Flexible monolithic ultra-portable ground penetrating radar using inkjet printing technology

Anya Nadira-Asanti Traille

THÈSE

En vue de l'obtention du

DOCTORAT DE L'UNIVERSITÉ DE TOULOUSE

Délivré par :

Institut National Polytechnique de Toulouse (INP Toulouse)

Discipline ou spécialité :

Micro-ondes, Électromagnétisme et Optoélectronique

Présentée et soutenue par :

Mme ANYA NADIRA-ASANTI TRAILLE

le mardi 25 novembre 2014

Titre :

FLEXIBLE MONOLITHIC ULTRA-PORTABLE GROUND PENETRATING RADAR USING INKJET PRINTING TECHNOLOGY

Ecole doctorale :

Génie Electrique, Electronique, Télécommunications (GEET)

Unité de recherche :

Laboratoire d'Analyse et d'Architecture des Systèmes (L.A.A.S.)

Directeur(s) de Thèse :

M. HERVE AUBERT

Rapporteurs :

M. ALAIN REINEIX, UNIVERSITE DE LIMOGES

M. DOMINIQUE BAILLARGEAT, UNIVERSITE DE LIMOGES

Membre(s) du jury :

M. GILLES DAMBRINE, UNIVERSITE LILLE 1, Président

M. COUSTOU ANTONY, LAAS TOULOUSE, Membre

M. HERVE AUBERT, INP TOULOUSE, Membre

M. MANOS TENTZERIS, GEORGIE TECH INSTITUTE OF TECHNOLOGY EU, Membre

Acknowledgements

I would like to acknowledge my thesis director Professor Hervé Aubert for coordinating this research, Sangkil Kim, Antony Coustou, Xavier Bouquet and Emilie Debourg for their contributions on characterization and assembly of the flexible circuits. I would also like to acknowledge IRD (Institut de recherche pour le déeveloppement)

Abstract

Flexible monolithic ultra-portable ground penetrating radar using inkjet printing technology A Ground Penetrating Radar (GPR) performs nondestructive detection of buried objects, or subsurface imaging by transmitting electromagnetic waves and detecting and analyzing the reflections. The main challenge of GPR is the reduction in detection range due to the severe signal attenuation that is caused by subsurface conductivity that becomes more severe at high frequencies. In order to increase the detection range, GPR uses lower frequencies than non-GPR radars and thus requires larger antennas that may limit system portability. Most GPR systems use impulse radars however the FMCW (frequency modulated continuous wave) radar can provide some advantages such as frequency versatility, reduced system maintenance and improved range resolution. Frequencies below 1 GHz were initially uncommon in short-range FMCW radars but are now finding their way back in systems such as ultra-wideband (UWB) ground penetrating radars for mine detection and as well as other applications. When measurements are performed on vehicles, large antenna fixtures are not a problem. Portability, however, can become an issue in geophysical studies or emergency work in which one may need to transport the system through rugged, unexplored and/or hazardous locations without vehicle access and perform measurements. Inaccessible environments may require climbing up and down, squeezing through, jumping over, crawling under, maneuvering through or swimming through obstacles (mountains, caves, lakes, rocky areas). In addition to transportation, rapid system setup is critical in difficult conditions such as freezing temperatures or extreme heat where exposure time is costly and limits measurement time. One solution to enhance the portability and deployability of a GPR system for wide area rugged measurements is to realize a complete system on a continuous substrate that is rollable around a reasonably small radius and storable in a scroll or poster-like fashion for easy backpack transportation. Electronics that can flex and bend have already used in military applications and for outdoor sporting gear. Currently, there are a few types of technology available to realize flexible electronics that have been a major topic of research, each

with different levels of integration. Inkjet printing technology offers a cost effective, versatile and efficient method for realizing flexible devices. In this work a classical FMCW radar system is designed and an effort is made, for the first time, to apply inkjet printing technology to a radar system. The system is referred to as a portable monolithic radar system in which all actives, passives and antenna are meant to share the same continuous rollable substrate. In doing this, a medium level of integration is used to investigate limits of system complexity, resolution and ultra miniaturization for tight rollability. Various design challenges of a large system are overcome that will hopefully give insight to new designs as the integration level using inkjet printing technology increases.

Contents

List of Figures

List of Tables

Chapter 1

Introduction

Liquid water is the most important and essential resources needed to host life. It is one of the most widely available ingredient of nature however due to man made activities, usable has become scarce in certain locations. The largest percentage of fresh water (70%) resides in ice caps, glaciers and snow and the second largest percentage (30%) is groundwater [98]. Ground penetrating radar, amongst other techniques can be used to locate groundwater sources.

1.1 Stepped frequency modulated continuous wave ground penetrating radar for groundwater detection

1.1.1 Concept of Operation

Ground Penetrating Radar (GPR) is a very popular microwave technique used to perform non destructive testing in a variety of applications ranging from civil engineering and forensics to environmental research, archeology and agriculture. A GPR system uses electromagnetic waves in the form of radar pulses to detect objects deep underground or within non-earth mediums such as within walls, bridges or other structure. GPR detection operates on the well known principle that an electromagnetic wave will undergo a reflection in the form of scattering when it encounters a sharp contrast in electrical properties. This same phenomena can be used to detect large bodies of groundwater. A GPR system can also synthesize a detailed image representative of the subsurface layers. When an electromagnetic wave is transmitted into an inho-

mogeneous ground, a portion of the wave is scattered back each time an electrical contrast is encountered. Each reflection reaches the receiver at a particular time instant and the receiver detects a series of distinct reflections versus time (Figure 1.1a) scattered from electric discontinuities that vary in space. The composite of the reflection amplitudes versus time is referred to as a reflection trace (Figure 1.1b). During a scan, measurement are taken and processed into reflection traces and collected across incremental spatial positions that is tangential to the measured surface (Figure 1.1c) known as survey lines. The traces can be combined to produce a wiggle diagram or 2D or 3D reflection profile. Producing such a profile require extensive amount of signal processing that includes filtering, background removal, deconvolution, velocity analysis, migration depth conversion as well as other steps.

Reflection surveys (Figure 1.9) employ various spatial configurations to measure signals traveling through the ground with each configuration providing different perspective for analyzing the signal path below the subsurface. There are five well known surveys, these include the common midpoint (FIgure 1.9c), common offset (Figure 1.9b), common source (Figure 1.9d), common receiver (Figure 1.9e) and trans-illumination (Figure 1.9a) survey. The common offset survey is the most commonly used and is performed by moving a single transmit and receive antenna along the ground surface with each antenna remaining at a fixed separation. The common midpoint reflection survey (WARR-Wide Angle Reflection Refraction) is performed by incrementing the transmit and receive antenna separation with respect to a fixed point and measuring the difference in two-way travel time for each spatial separation. Common source surveys involve transmitting to multiple receiver antennas and common receiver configurations involve receiving from multiple transmit antennas. In trans-illumination surveys, used in borehole GPR, a transmit antenna directly illuminates the receiver. A more thorough overview of methods GPR uses to collect data can be found in [79]. GPR can complement other nondestructive methods such as electromagnetic induction, seismic detection, infrared detection, resistivity and acoustic methods [74].

GPR Applications

GPR is a sucessful nondestrutive analysis technique used in various applications in the fields of archeology, geophysics, utility detection, civil engineering and snow research. The following applications have been listed in [Daniels] and numerous other references as having successfully utilized GPR:

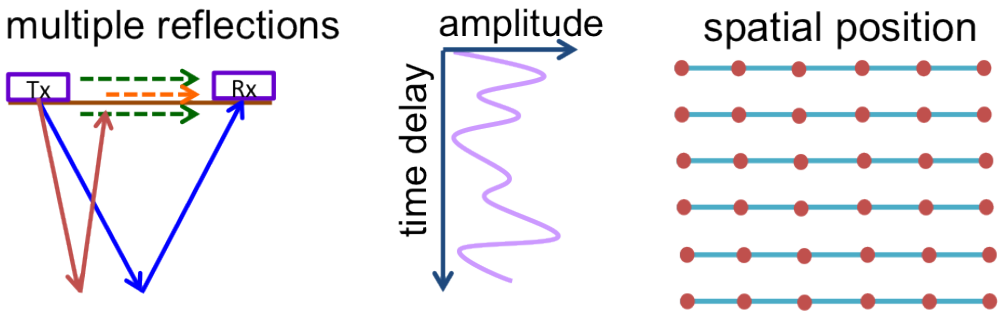

(a) GPR Reflections

(b) reflection(s) amplitude versus time

(c) wide area measurements across different spatial positions

Fig. 1.1 GPR concept of operation.

- Civil engineering: nondestructive testing and assessment of tunnel linings, wall condition, bridge decks, reinforced concrete, building condition, road condition and rail tracks
- Utilities: pipes and cable detection, mapping trench boundaries
- Geophysics: planetary exploration, snow/ice/glacier studies, measuring the depth to bedrock, depth to water table, mapping or detecting permafrost, imaging fractures and cavities, measuring glacier thickness, soil/rock characterization
- Environmental or geotechnical: investigation of land contaminants, mapping landfills, borehole inspection
- Snow research: to understand the properties of snow for environmental studies on energy balance (FMCW radar)
- Other Applications: archaeological investigations, timber condition, mine detection, forensic investigations, medical imaging, soil moisture content for agriculture and remote sensing

1.1.2 Exploration Depth

Groundwater can exist over a hundred meters deep. Ground Penetrating Radar is a useful technique because of the high resolution detection and imaging capabilities, however the exploration depth of GPR is limited. The achievable exploration depth of a GPR system depends on several factors: subsurface material properties, frequency, power, instrumentation and signal processing.

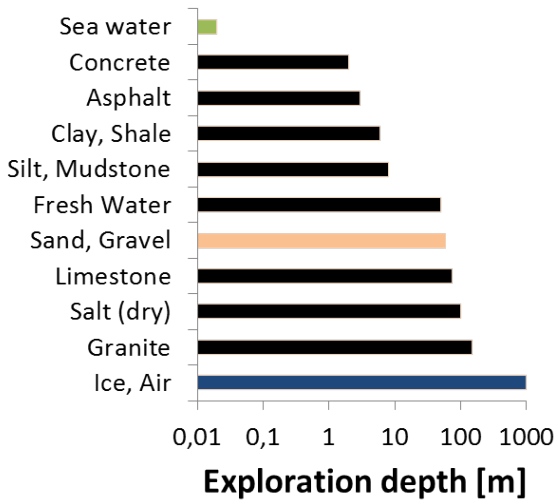

Fig. 1.2 Largest observed GPR exploration depths for different subsurface materials.

Subsurface materials

The primary uncontrollable factor that limits GPR exploration depth is the subsurface material properties. This is because the conductivity the material determines the skin depth or level of signal attenuation undergone. Figure 1.2 shows the best case possible exploration depths and it can be seen that materials such as ice are as transparent as air, and in materials such as dry sand and certain types of snow, a perfect GPR system can theoretically see 100 meters. For materials such as concrete or those containing clay, no more than 10 meters can be observed. Achieving such depths in Figure 1.2 is very difficult, even with commercial systems. The measured properties of common soil materials can be found in [29]. This data is used to determine more precisely the amount of attenuation loss for the GPR signal for specific soil conditions and at specific frequencies.

Frequency

The second factor dictating exploration depth is frequency. Low frequencies undergo less attenuation and therefore travel further however lowering the center frequency increases the pulse length and degrades the resolution, especially for impulse radar. The tradeoff between resolution and exploration depth (Figure 1.3) must be handled depending on the application. For instance FMCW radars used to characterize the properties of snow (properties which have a spatial distributions that vary on the order of a few centimeters) require architectures that utilize one or multiple frequencies

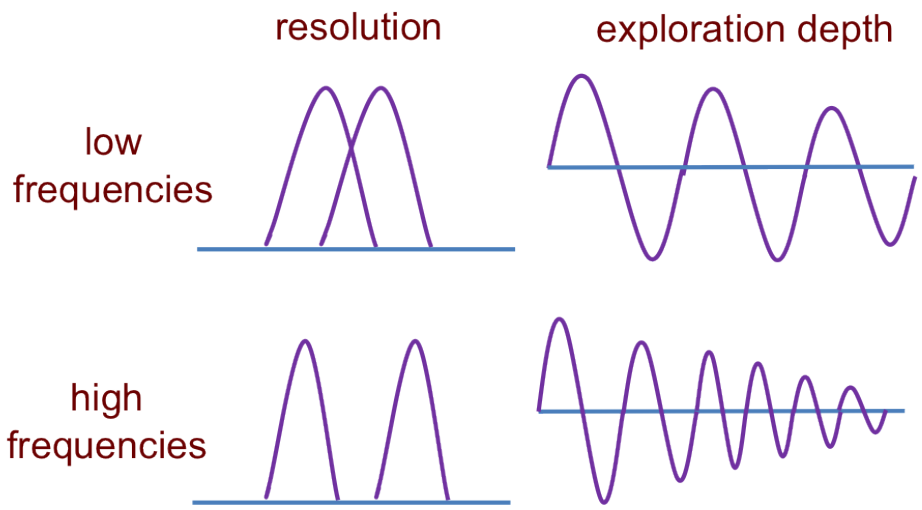

Fig. 1.3 Resolution versus exploration depth tradeoff.

between 4-40 GHz (C, K, Ka, Ku bands) in order to image different levels of snow. In utilities detection applications, when imaging larger structures such as pipes less than one meter deep, frequencies over 1 GHz are sufficient. For environmental applications, in order to reach large scale landforms that are deeply buried in soil that is potentially damp or wet, frequencies under 500 MHz are needed and some cases in literature even report frequencies as low as 25 MHz [Harry M. Jol].

Power

Another factor affecting exploration depth is power. Raising the transmitted power level increases the exploration depth however the exponentially increasing level of power needed to penetrate deeper into the ground makes this one of the less effective methods of increasing penetration. GPR systems are usually categorized as UWB devices, and therefore must conform to the rules for UWB power emissions limits as well. Table 1.2 shows the maximum allowed peak power spectral density and Table 1.1 the maximum allowed mean power spectral density for GPR devices for various frequency ranges according to the European rules [43]. In the Electromagnetic compatibility and Radio spectrum Matters (ERM); Code of Practice in respect of the control, use and application of Ground Probing Radar (GPR) and Wall Probing Radar (WPR) systems and equipment [34], concerning the use of Ground Penetrating Radar in Europe, several requirements are specified to minimize unnecessary radiation. These include: keeping the transmitter on only during measurements, having a deactivation mechanism, avoiding measurements near a radio site unless an agreement is made, and

whenever practical, *to ensure that the GPR/WPR operating face is in contact with a layer of absorptive earth or structural material of sufficient thickness and properties to absorb and dissipate the GPR/WPR low level radiation* [34]. More information can also be found in the CENELEC European Committee for Electrotechnical Standardizations: Electromagnetic Compatibility (EMC) [19], guide list [18], guide 24 [16] and guide 25 [17].

Max allowed measured radiated PSD	
Frequency Range [MHz]	**Maximum Peak PSD**
30 to 230 MHz	-44.5 dBm/120kHz
230 to 1000 MHz	-37.5 dBm/120kHz

Table 1.1 Maximum allowed measured radiated PSD for GPR/WPR imaging systems according to European rules taken directly from [43]

Max allowed measured radiated PSD	
Frequency Range [MHz]	**Maximum Peak PSD**
<230 MHz	-65 dBm/MHz
230 to 1000 MHz	-60 dBm/MHz

Table 1.2 Maximum allowed mean PSD for GPR/WPR imaging systems according to European rules taken directly from [43]

For the US, the FCC MPE (Maximum Permitted Exposure) limits for electric fields in the 30MHz-300MHz range according to US rules are shown in Table 1.3.

Maximum occupational (controlled exposure)	1mW/cm^{2}, 0dBm/cm^{2} (time averaged over 6 minutes)
Maximum general population (uncontrolled exposure)	0.2mW/cm^{2}, -7dBm/cm^{2} (at any given point in time)

Table 1.3 Maximum permitted exposure (MPE) according to FCC rules [94]

The same efforts to minimize radiation are made in the US as they are in Europe [34] in regards to the antenna design and positioning. The power radiated into the air is considered as backlobe radiation and should be varified for each system. For the case of stepped frequency GPR, as was done in [97], the power emissions lim-

its under NTIA rules may also apply. The NTIA (National Telecommunications and Information Administration) standards for non-licensed devices can be found in [78].

Other factors affecting exploration depth

In addition to all the factors mentioned above, signal processing and hardware also affect the exploration depth and can significantly improve detection range and measurement reliability. The selectivity and sensitivity of the receiver will of course have the biggest impact on the detection range. In the case of GPR, gating switches add further enhancements by allowing the system to transmit more power while still detecting weak GPR reflections.

1.1.3 Groundwater

Ground penetrating radar requires expertise in two main areas: electrical engineering and/or geophysics therefore in addition to system engineering work, a very thorough detail of study into the geophysical nature of groundwater was performed to determine the system requirements. Groundwater originates from rain, snow, lakes or rivers and is recharged from the surface into the ground. Underground water resides within soil pore spaces (Figure 1.4a), or within rock fractures and voids, in this case referred to as aquifers (FIgure 1.4b). Groundwater can come to the surface naturally or can be extracted from wells. The interest in observing groundwater is usually related to agriculture, contamination, resource management, or just understanding its effect on land formations.

The level at which water is found is called the water table. When using GPR to locate a groundwater table, a detection challenge is encountered due to the existence of a inhomogeneous zone that that reduces the contrast seen by electromagnetic waves, weakening the GPR reflections, particularly for high frequencies (Figure 1.5a). The inhomogeneous zone is formed by a capillary fringe [10] which is a tension saturated layer about half a meter thick where groundwater moves upwards through pores by means of capillary action and feeds what is called the transition zone. The capillary effect and transition zone thickness depend on the pore size, shape and number [8, 31]. In coarse textured soils the capillary fringe is thinner and creates a more sharp dielectric contrast to the transition zone whereas in fine textured soils the capillary fringe is thicker and creates a more gradual dielectric contrast to the transition zone [31]. The movement of water ($\epsilon_r = 81$) from the saturated region through pores

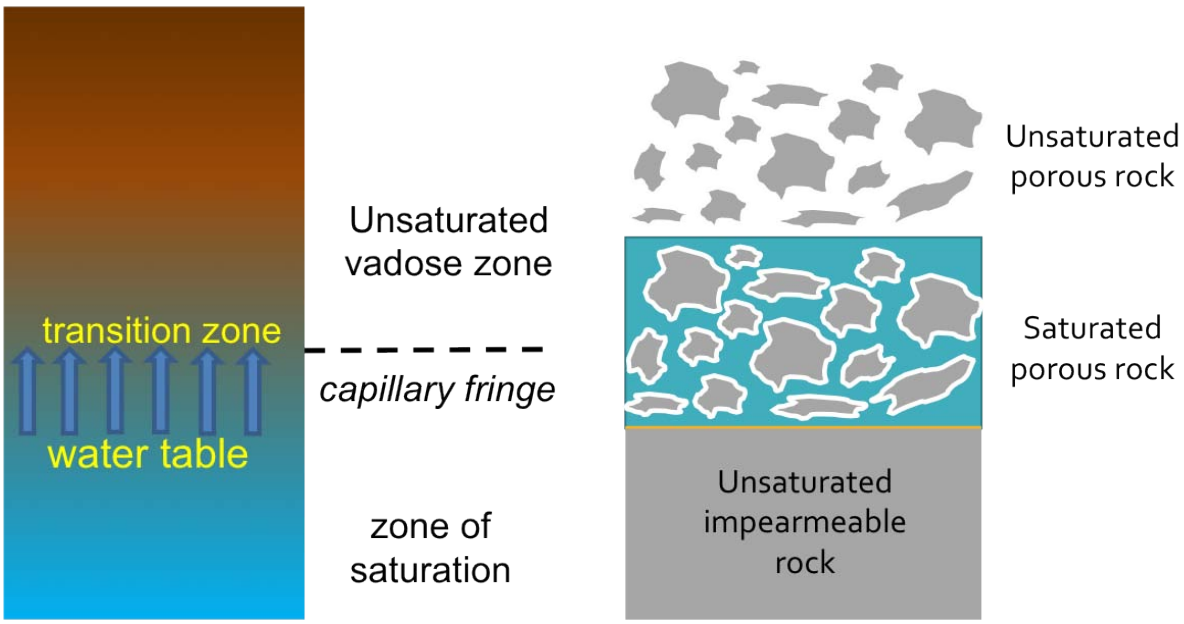

(a) soil pore spaces (b) fractures of rock formations

Fig. 1.4 Groundwater.

towards a low ϵ_r unsaturated region of soil (ϵ_r = 3-15) results in transition zone electrical properties that gradually progress. High frequency signals with wavelengths that are small compared to the transition zone thickness will fail to see the impedance contrast and therefore undergo significantly weaker reflections, often causing failure of the GPR system to detect the water table [47]. The thicker the transition zone, the lower the frequencies required for adequate detection [8] and often groundwater detection requires even lower frequencies than other buried targets such as those in other applications (Figure 1.5b).

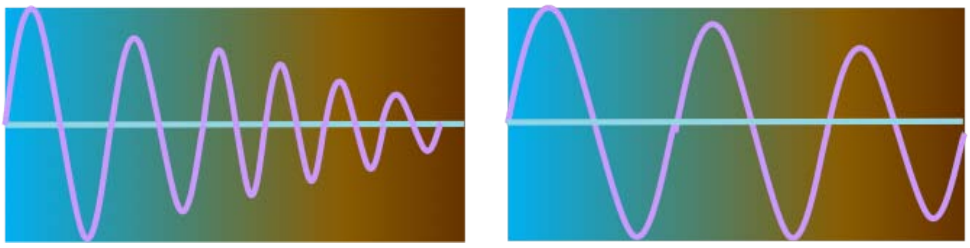

(a) High frequencies: wavelength too small to observe contrast (b) Low frequencies: wavelength large enough to see contrast

Fig. 1.5 Groundwater detection challenge.

According to [31], when estimating water table depths with impulse GPR, frequen-

cies of around 10-300 MHz are necessary and allow for a large exploration depth. The resulting degradation in resolution from the low center frequency can be compensated for through signal processing techniques to improve the target recognition or contrast between layers. In [47] it was found through measurement that the detection range of a 100MHz GPR antenna was limited to 35m while that of a 500MHz GPR antenna was limited to only 9m. In addition, using the 100MHz antenna resulted in more accurate groundwater detection than the 500MHz antenna as there was less masking due to the transition zone. In [92], a commercial GPR with 50MHz and 100 MHz antennas successfully detected a water table located 10 meters below the ground surface. In [20] it is indicated that GPR frequencies of less than 100 MHz undergo optimal conditions when it comes to subsurface attenuation.

1.1.4 FMCW/SFCW Architecture

For ground penetrating radar, it is ideal to keep a low center frequency for maximum exploration depth and a large absolute bandwidth for good resolution [85]. This is done by maximizing the bandwidth to center frequency ratio (B/fc $\approx$ 1). The SFCW (Stepped Frequency Continuous Wave) architecture, also known as SFMCW (Stepped Frequency Modulated Continuous Wave) is based on the FMCW (Frequency Modulated Continuous Wave) or chirp radar which operates like the impulse radar, except that it acquires the information in both the time and frequency domain (generally speaking). The FMCW radar transmits a frequency sweep or chirp and the reflected echo is delayed in time (Figure 1.6a, Figure 1.6b). The receiver correlates the transmitted and received signal (Figure 1.6c) and the converted signal is an IF beat frequency that is proportional to the target range (Figure 1.6d), and that can be sampled (Figure 1.6e) by a low speed analog to digital converter and then interpreted using the IFFT (Figure 1.6f).

Most GPR groundwater detection has been performed with impulse radars however the FMCW radar can provide some alternate advantages in ground exploration. The FMCW-based architecture is very practical for GPR, particularly because of the fine resolution capabilities. Sweeping the frequency decreases the pulse length at a rate that is inversely proportional to the absolute sweep bandwidth Δ R = v/(2B), therefore provides higher resolution detection and imaging. The FMCW chirp also transmits more energy with less average power: $E = P_{av}T_m$, increasing the signal to noise ratio ($SNR \propto T_m$) which is beneficial for GPR which suffers from a significant amount of background noise. The FMCW/SFCW transmitter architecture provides

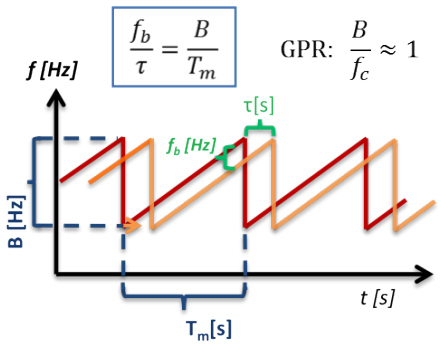

(a) Tx/Rx frequency versus time

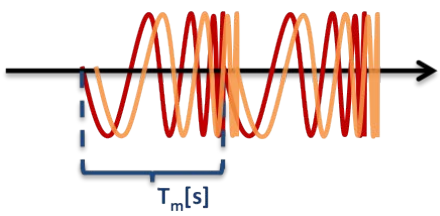

(b) Tx/Rx Chirp

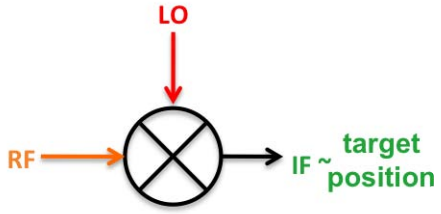

(c) Correlate Tx/Rx to produce f_b

$$f_b = \frac{B\tau}{T_m}$$

(d) beat frequency proportional to target distance $\tau = 2R/c$

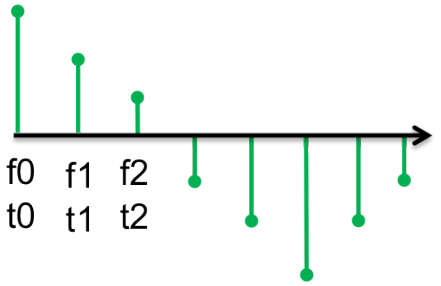

(e) sample with low speed ADC

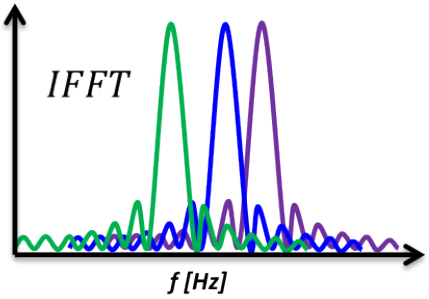

(f) IFFT

Fig. 1.6 FMCW concept of operation.

easy control over the frequency and radiated power, making the system extremely versatile for varying power emission limits or for different measurement conditions. The FMCW/SFCW receiver design demonstrates high efficiency and a low noise figure, both of which increase the dynamic range and increases exploration depth by allowing more power to be transmitted, weaker reflections to be detected despite strong surface reflections. The FMCW receiver also allows for easy control of the system gain and filtering which facilitates the analog to digital conversion of the beat frequency. The

simple low power hardware used (power amplifier, analog to digital converter) reduces the required system maintenance and finally these types of radars are also more difficult to intercept because the transmitted power spectrum is rectangular. One major disadvantage of FMCW/SFCW radar systems is that the continuous transmission introduces leakage into the receiver, usually 100dB higher, thus requiring at least 60dB of isolation. Range sidelobes can also make these types of radars vulnerable to nearby reflections and clutter.

For the SFCW architecture in particular, transmitting in the form of discrete frequency steps rather than a continuous sweep allows for I/Q processing. With a slight modification in architecture, the signal can be mixed with the two orthogonal basis functions having correlation of zero (cosine and sine). The real and imaginary parts allow for computation of amplitude and phase of the frequency spectrum. This is beneficial as phase conveys more information than magnitude. In the case of detecting a target, the magnitude energy peaks and decays independently of the phase whereas the phase energy is more equally distributed across all frequencies. The phase properties are more easily detected in situations where the SNR is lower, making it better than amplitude detection.

A frequency domain radar system can be designed to be switchable between SFCW and FMCW modes and is often done in certain applications to exploit the complementary advantages of both. Swept FMCW demonstrates high processing speed, moving platform tolerance, high unambiguous range, better spectral purity and facilitation of gating. With swept FMCW though, data acquisition can be complicated, I/Q processing is not performed and achieving high linearity over a wide bandwidth is very challenging (posing the issue of range sidelobes). SFCW can achieve very linear sweep over a wide bandwidth, implement I/Q processing for more accurate detection/imaging and zooming capabilities and the data acquisition is simpler since it is performed at discrete steps. SFCW however suffers from digitally induced spurious emissions that can cause false detections and as well as doppler smearing (leakage between range bins) due to the slower processing.

The first patent for FMCW radar was filed by J.O. Bentley for the *airplane altitude indicating system* [60]. FMCW radar is still used today in the radio altimeter (RADALT), meteorological and atmospheric observations, through wall detection, tank liquid level measurements, vehicle collision warning, small motion measurements and other short range applications, typically using frequencies above 1 GHz.

1.1.5 State of the art Systems

Table 1.7 displays three examples of state of the art radar systems using different architectures: SFCW, SFCW/FMCW and FMCW. The first system, WISDOM (Figure 1.7a) [21] down-converts DDS output with a reference oscillator to obtain a highly linear frequency sweep, stepping over a wide bandwidth. It also employs an automatic gain control circuit containing a variable gain amplifier in order to transmit the same power level across all frequencies. The gating switches increase the dynamic range by allowing the system to transmit more power while still detecting weak GPR reflections. Gating is quite complicated, as it requires switches on the order of nanoseconds in order to gate out surface reflections. The second system, PANDORA (Figure 1.7b) uses DDS output that is split across 8 channels, amplified, recombined in a Wilkinson combiner and transmitted. The received signal is sent to the LNA, then split into several channels using band pass filters before detection. Isolation between the channels is achieved by performing measurements in two phases in which only half the channel frequencies are used at a given point in time, essentially creating a gap between channels. It was emphasized that realizing this radar system consisted or integrating off the shelf components [109]. The third system (Figure 1.7c) is designed for a larger exploration depth and reduced range resolution, justifying the need for VHF frequencies. It actually features two different modes of operation UHV and VHF for different exploration depths. The frequency sweep was obtained by downcoverting a digital chirp synthesizer with a YIG oscillator, then using automatic gain control to maintain uniform power at all frequencies. The architecture shown also illustrates the use of attenuators for matching. Two sets of bowtie antennas are used having lengths of 80cm and 20cm for the VHF and UHF operation modes [51].

VHF frequencies are commonly used for impulse radars but frequencies below 1GHz are not so common for most short-range FMCW radars used in tracking, navigation, meteorological studies, sensing and other applications. The VHF microwave band (A-band up to 250MHz and B-band 250-500MHz), was commonly used for two- way radio communication and today used in television broadcasting, land mobile radio systems, air traffic control and other applications. It is obvious that the large physical antenna size degrades angular resolution, but despite this disadvantage, the ability of these frequencies to travel further at less power makes it essential for some applications. These frequencies are becoming practical for use in UHF microwave band radars C-band (300MHz-1GHz) and A-C band Ultra-wideband (UWB) Radars. Such radars are used in ground exploration for archaeological explorations, soil mapping and mining

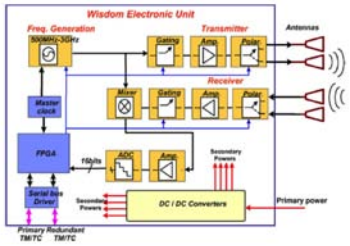

(a) WISDOM radar

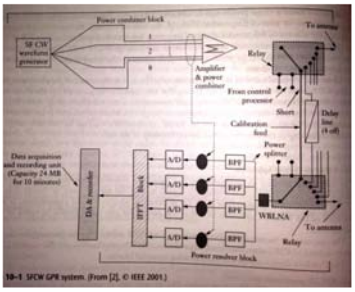

(b) Pandora radar

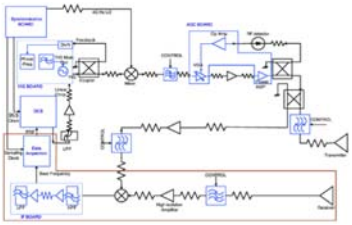

(c) UWB radar

Name	WISDOM (Water Ice Subsurface Deposits Observation on Mars)	PANDORA (Parallel Array for Numerous Different Operational Research Activities)	Ultrawideband penetrating radar
Application	high resolution imaging of sedimentary layers of well preserved organic molecules (ESA 2018 ExoMars Rover mission)	Landmine detection and other applications	Measuring the thickness of sea ice above water
System	Gated SFCW GPR	FMCW/SFCW GPR multichannel	FMCW GPR 2 modes
Frequency	500MHz - 3GHz N = 501 $\Delta f = 5MHz$	400MHz - 4.845GHz across 8 channels	VHF: 50-200MHz T_m = 2ms, f_s = 500kHz R_{un} = 3-30m UHF: 300-1300MHz T_m = 10ms, f_s = 500 MHz R_{un} = 0.5-5m
Exploration depth	2-3 meters	1-4.5 meters	0.3-10 meters
Resolution	A few centimeters	<5 centimeters	VHF: 75cm UHF: 15cm
Transmit Power	10-20 dBm	Average power = 5W 37 dBm per channel	20 dBm

Fig. 1.7 State of the art radars employing SFCW dual SFCW/FMCW or FMCW architecture.

applications.

1.1.6 Research Focus

This work is dedicqted to the design of a SFCW/SFMCW GPR (stepped frequency modulated continuous wave ground penetrating radar) system designed specifically and exclusively for groundwater detection at very large depths. This requires a system designed for a long detection range and with a sufficient resolution to detect or image a large groundwater source, therefore frequencies of no more than 400 MHz will be used. The system developed in this work utilizes as unique combination of technologies (Figure 1.8) that cannot be found commercially or in literature. Nearly all GPR systems for geophysical/environmental applications, more specifically for groundwater detection use impulse radar. Impulse ground penetrating radar systems are prevalent in academic research and exist on the market but a recent interest other types of radars, such as FMCW, for ground penetration has arisen due to some advantages it gives in performance and system architecture. FMCW radars are not commercially available and existing FMCW GPR architectures for research have been designed for applications such as snow research, shallow soil mapping or landmine detection. These radars use frequencies over 1GHz and are designed to penetrate no more than 5 meters deep. Ultra-wideband FMCW/SFCW ground penetrating radars for very high resolution imaging applications have been realized by focusing primarily on a general system architecture and using commercial state of the components. High performance, portable systems have also been realized by developing new hardware over a long period of time. There do exist some FMCW GPR systems designed for long range detection using VHF frequencies for measuring sea-ice thickness. Currently there exists almost no FMCW/SFCW radar system that is specifically designed detect groundwater at depths of tens of meters while also addressing the low frequency restriction in the case that a transition zone exists [7]. The first focus of this research will therefore be to design an FMCW/SFCW Ground Penetrating Radar to accurately detect the presence of water in realistic conditions. Frequencies under 1 GHz will be used to achieve ranges over tens of maters, and restricted to below 500 MHz to ensure good detection despite the possible presence of a transition zone. Improvements in SNR, dynamic range, penetration depth and probability of detection can be made, particularly for groundwater research applications. This system will provide a theoretical and experimental foundation to address the portability issues in ground penetrating radar applications through the development of a flexible monolithic ultra-portable ground penetrating radar using advanced fabrication technology.

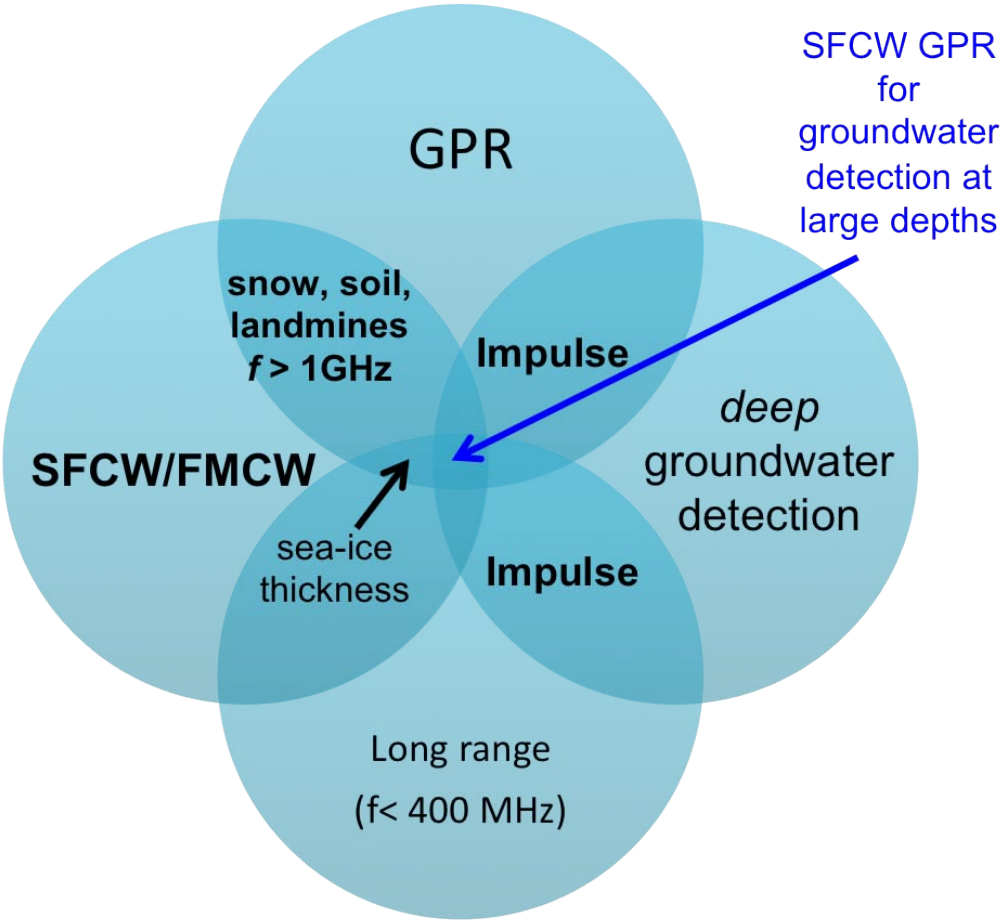

Fig. 1.8 Development of a new radar system using a unique combination of technologies (type of radar, chosen architecture, frequencies, application.

1.2 Ultra-portable ground penetrating radar using inkjet printing technology

1.2.1 Portable monolithic radar

GPR reflection surveys can be complex, tedious, dangerous, time consuming and expensive (Figure 1.10). The complexity arises from the fact that certain measurement require the system to be moved across wide areas (Figure 1.9) and/or for the system antennas to be oriented in different spatial configurations (Figure 1.10a). Many commercial vendors include practical portability enhancements such as equipping GPR systems with wheels.

In addition, GPR systems designed for large exploration depths use low frequen-

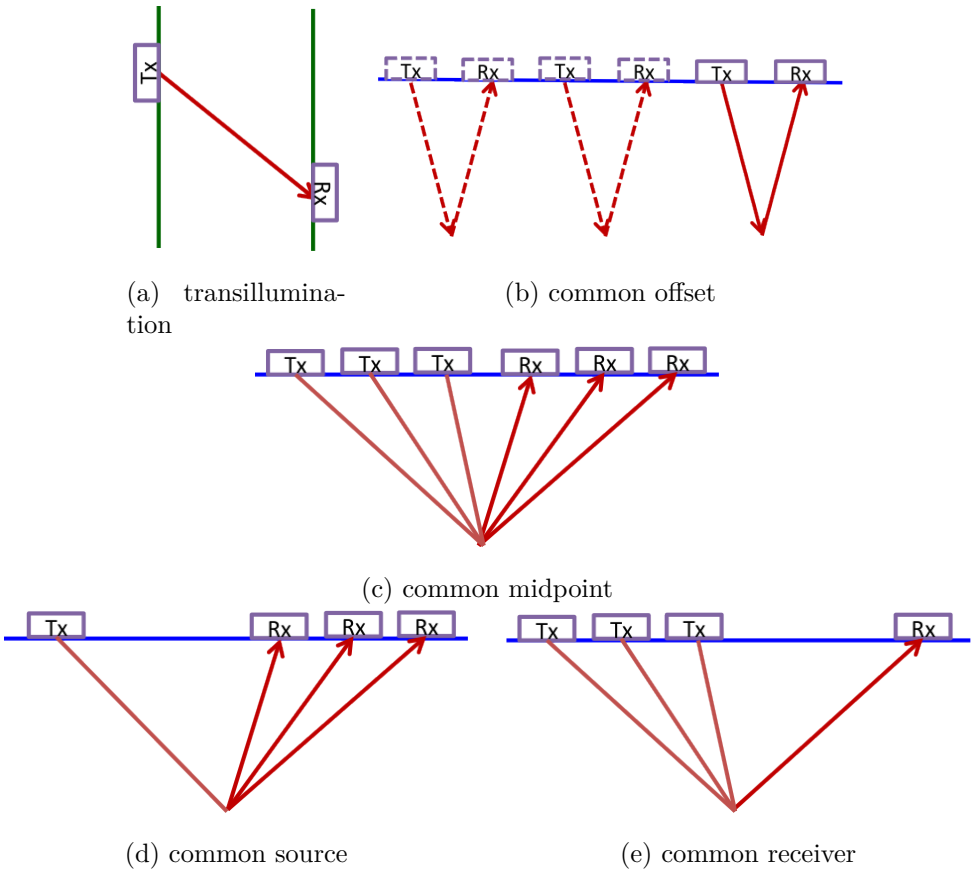

(a) transillumination (b) common offset

(c) common midpoint

(d) common source (e) common receiver

Fig. 1.9 Reflection Surveys.

cies and therefore require physically large antennas. This is why many systems, in addition to wheels, also come with detachable antennas. Extremely large antenna fixtures are manageable when wide-area measurements are performed using vehicles or sleds however in many geophysics studies or emergency work, one often needs to transport the the system through difficult to reach areas with limited vehicle access (FIgure 1.10b) and hazardous conditions such as extreme heat, arctic cold or volcanic environments (FIgure 1.10c). Many of these locations are unexplored and unmarked, therefore require climbing or maneuvering through small spaces (mountains, caves, rocky terrains) by foot. In such environments, the safe and easy portability of the system becomes extremely critical, just as it is when hiking. In addition to portability, when measurements must be performed in unfavorable conditions such as extreme heat, damp, or freezing temperatures, the rapid deployment and repacking of the entire system is critical, as it will save exposure time and cost by decreasing setup time and maximizing measurement time. A more portable system will also require less staff

to support while transporting and setting up the system which significantly saves cost.

(a) GPR sytem in verticql configuration (http://www.malags.com/solutions).

(b) GPR used in location without vehicle access (http://www.malags.com/solutions).

(c) GPR used in hazardous environments (http://www.malags.com/solutions).

Fig. 1.10 GPR applications involving measurements in rugged outdoor environments.

An ideal solution for an ultra portable radar would be to realize a complete system on a continuous rollable substrate. The system would be ultra thin, therefore rollable and able to fit into a compact container for storage. It would be lightweight, therefore back attachable and simple to transport because it folds up as tightly as a tent. And finally the deployment would simply involve unrolling the system to setup for measurements and rolling the system when measurements are complete (Figure 1.11). Such a system would require for at least all actives, passives and antenna to share the same common substrate. To accomplish this, we look to electronics that can flex,

bend and roll. Such electronics are already used in military and outdoor sporting gear (ex. solar backpacks). Currently, there are several type of technology for realizing flexible electronics, each differing in the level of integration and performance. Some are commercially available while others are still under research.

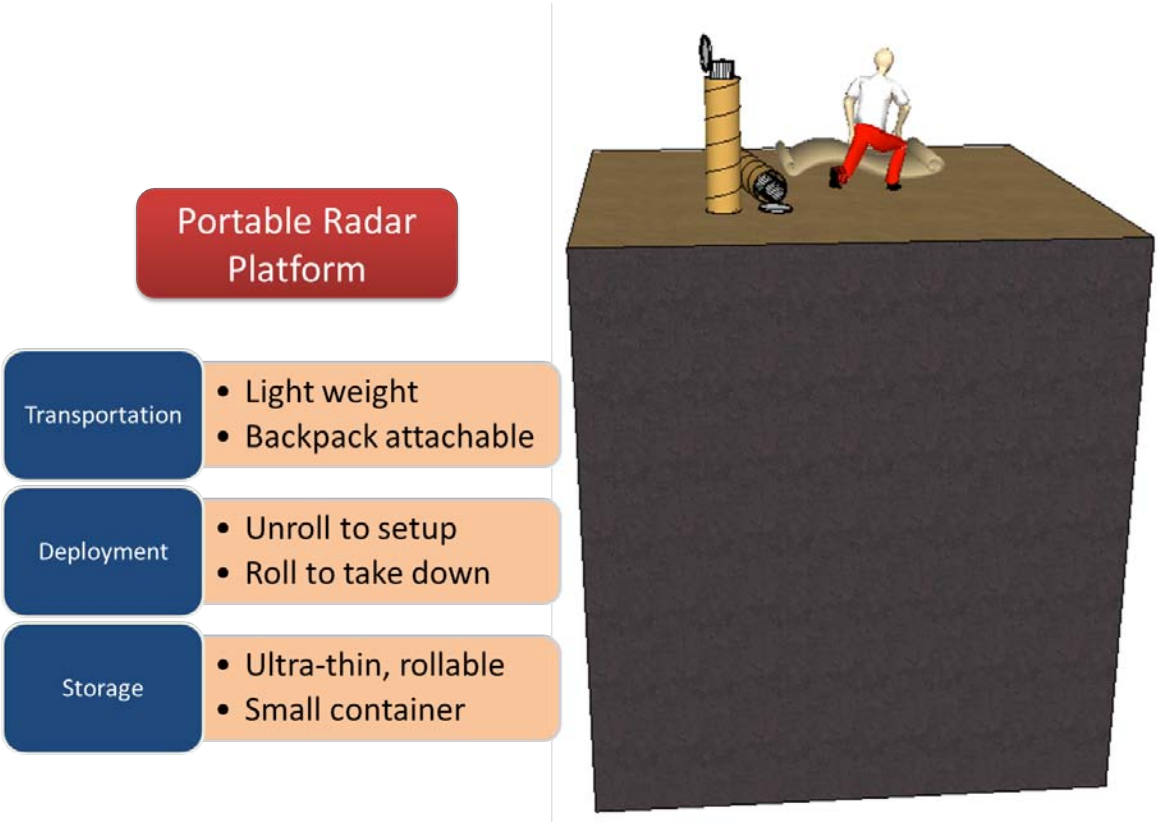

Fig. 1.11 Concept of ultra portable ground penetrating radar system.

1.2.2 State of the art devices

In order to realize a rollable radar system it is necessary to look into flexible electronics. One of the primary objectives in electronics packaging was miniaturization and integration, as it still is today. Technologies then emerged that could benefit from the ability of electronics to merge physically with non-rigid real world objects. As the number of devices per person increases, efforts are being made to make technology less imposing to the individuals personal space and time. Flexible electronics is now one of several types of disruptive technology (Figure 1.12) because it allows devices to be more easily integrated into everyday life by making them smaller, portable, wearable,

bio-compatible and even environmentally friendly (Figure 1.13) while also enhancing the functionality and performance, particularly for sensors.

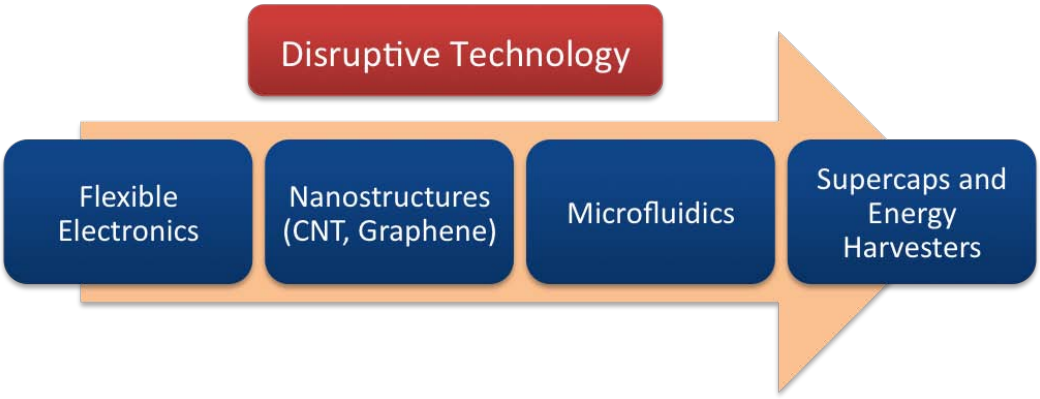

Fig. 1.12 Flexible electronics is one of several types of disruptive technology.

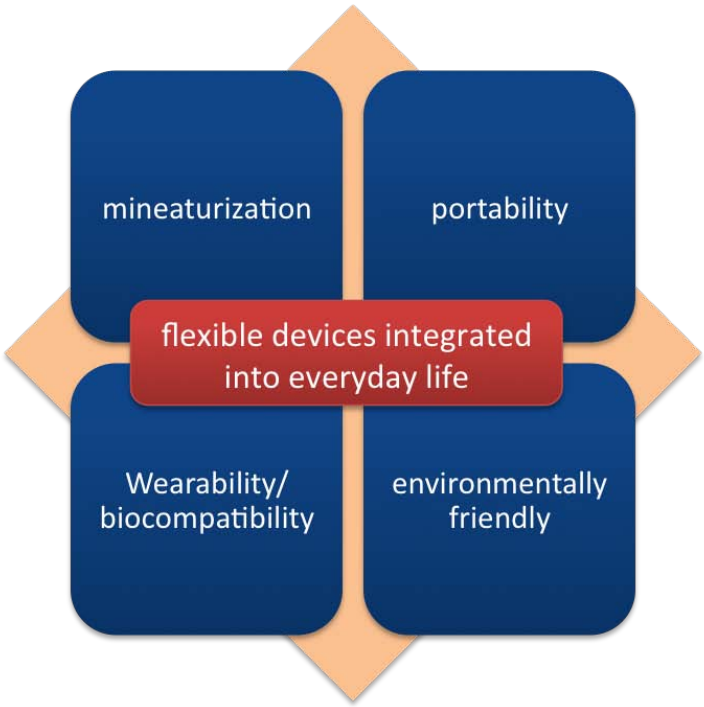

Fig. 1.13 Flexible electronics benefit to everyday life.

Stretchable electronics

Stretchable electronics (or elastic electronics, elastronics) are electronics that can be pulled and elongated, increasing their area by several percent while still operating nor-

mally. In most cases the electronics are completely encapsulated in a stretchable material. Stretchable electronics are ideal for sensor applications (stress/strain/pressure) and applications where electronics are tightly wrapped around objects that expand and contract such as smart skins, band-aids and structural monitoring devices. Additional applications of stretchable electronics include batteries, capacitors solar cells and clothes. Substrates used in stretchable electronics are usually polymers such as polyurethane, polymide, silicone and other flexible materials. Realizing interconnects with elastic properties has been a major research topic and various types of technology have been used ranging from patterning conductive materials (such as gold) onto elastic membranes to using SWCNT based stretchable conductors [14]. Rigid but miniaturized commercial off the shelf components are still used in stretchable electronics and one of the key challenges is managing the mechanical strain induced on the interconnects when stretching, a challenge that will continue to be a topic of research. For many of these devices, bonding is typically performed with low temperature solder alloy that is compatible with the stretchable materials.

Flexible electronics

Flexible electronics are electronics that can bend and flex. The typical structure consists of a flexible circuit mounted onto one or both sides of a flexible substrate. Applications for flexible electronics include those used for stretchable electronics as well as other devices such as keyboards, instrument panels, printers, cameras, calculators and solar cells. The typical technology used in flexible electronics is either etching or inkjet printing. Substrates usually include materials such as polymide, PEEK, polyester, PET and paper.

Rollable electronics

Rollable electronics, in addition to flexing, can roll about a reasonably small radius like a scroll or a poster. In many cases this includes stretchable electronics. Rollability is ideal for applications requiring mineaturization or convertibility within other devices or simply for rollable storage and easy transportation. *The electronics world has been dreaming for half a century of the day you can roll a TV up in a tube* [68]. Other uses of rollable electronics are for dynamic performance; devices designed to operate while in the rolled state. In addition to rollability, the mechanical properties of rollable electronics also make them thinner, lighter more robust (cleanable and less susceptible

to breakage when dropped). Rollable electronics are useful for the applications already mentioned in stretchable and flexible electronics. Biocompatability is another useful feature of rollable electronics for wearable/implantable medical devices.

In this work, rollability is of interest for ultra miniaturization of the GPR system. A new type of packaging is needed to realize a radar with this level of mechanical versatility, which is why we look at flexible electronics. The specific mechanical requirements for rollable electronics present key challenges that can only be met with new materials and new fabrication technology. As flexible, stetchable and rollable electronics, device such as antennas, batteries, sensors and flexible displays have already been demonstrates as seen in Figure 1.14. Examples include bendable antennas on liquid crystal polymer (Figure 1.14a from [81]), foldable antennas printed on paper (Figure 1.14b from [65]), flexible/stretchable batteries (Figure 1.14c from [112]), flexible sensors for medical applications (Figure 1.14d from [99]), wearable/biocompatible devices such as contact lenses (Figure 1.14b from [87]) and interactive displays (Figure 1.14d from [110]). There are different ways of realizing flexible electronics, with each differing in the type of materials used, the technology process, and the level of integration.

1.2.3 Technology Processes

For most flexible electronics, conventional technology processes cannot be used. It is necessary to use a technology process that is both compatible with the low cost flexible materials used (Figure 1.15) by not causing thermal damage to them but at the same time reliable enough for the system to remain assembled and resist failure when mechanically stressed.

FlexCircuits

There are a few types of technology available to realize flexible electonics. FlexCircuits for example are available commercially (allflexinc, flexiblecircuit). They are made from polymide film laminated onto copper sheets and chemical etching is used for the circuit. A coverlay made out of polymide is often used as a protective top layer. The single sided flexcircuits have one conductor layer so components and interconnections are located on one side and accessed only from that one side. Minor crossovers can be formed on top of the coverlay. The advantage of the single layer design is that it has the advantages of being very thin (less than .10mm-.20mm) which is useful for certain

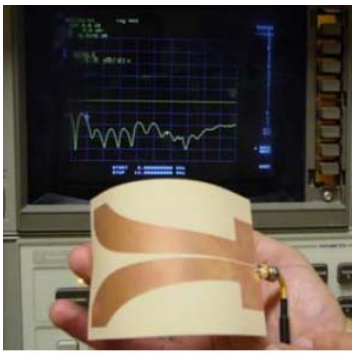

(a) Flexible DTSEA on LCP [81].

(b) Foldable magic cube antenna on paper [65].

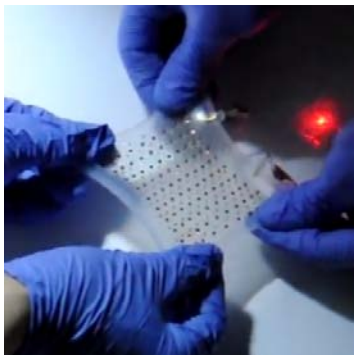

(c) Stretchable battery [112].

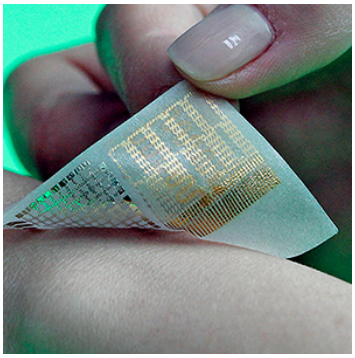

(d) Flexible/stretchable medical patch [99].

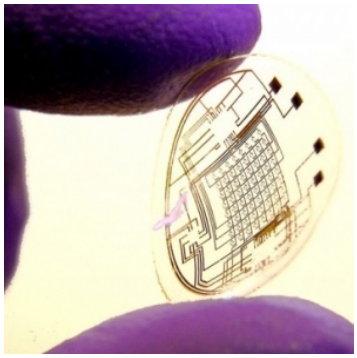

(e) Bionic contact lens [87].

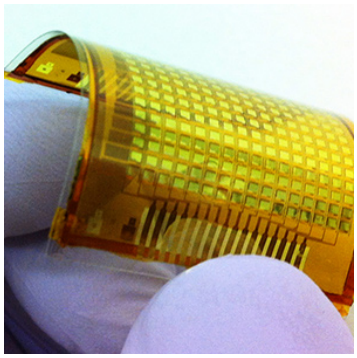

(f) Interactive display [110].

Fig. 1.14 State of the art flexible devices.

applications prioritizing ultra thinness over high density. Single layer Flexcircuits with access on both top *and* bottom sides can be realized but require special processing and lasers to create such an access. Another commercial configuration reported is the sculptured flex circuit that uses multi-step etching to vary the conductor thickness at different sections to optimize either mechanical flexibility, electrical properties or assembly (making built-in termination points for connectors). Double sided flexcircuits can be used for more dense layouts that require GND or power planes, shielding, or layouts that just do not allow one layer. Double sided flexcircuits have two conductor layers and the components and interconnections are placed on both sides and access across layers is achieved with plated thu-holes. Multilayer flex circuits are available for even denser applications and provide impedance control, crosstalk elimination and shielding for applications and frequencies requiring it. They contain 3 or more conductors layers, each accessible with plated through holes or by other means. Flexibility can be maintained by not using continuous lamination and leaving air gaps. Finally

more low cost flexcircuit is also commercially available where referred to as polymer thick film flex circuits made by screen printing conductor onto polymer film, and in the case of multilayer designs, printing insulating layers in between. It is reported that the low conductivity makes these more ideal for low-power but higher voltage applications.

Printing methods

Printing electronics offers a cost effective and efficient approach to realizing miniaturized, complex, stretchable/flexible/rollable devices. Various printing methods can be selected depending on the desired substrate, printed material, precision, printing area, layer quality, adhesion properties, time and cost desired for the job. For a large radar system at low frequencies, with a large antenna, the high volume/low precision roll-to-roll production could be more ideal than the sheet-based production.

Several printing methods already used in the printing industry are now used in electronics. Impact methods such as gravure, originally developed for printing newspapers gives the highest resolution and speed, and high volumes, which is why it is still used today for magazines and in graphic arts. The main disadvantage of this method is that the setup is timely and costly; rolls are expensive to pattern and the patterning process is slow. This can be major setback for realizing designs that differ from one another. In the area of electronics gravure can be used for printing organic semiconductors, organic and inorganic conductors and dielectrics. Lithography is the most widely used type of printing, still used for newspapers today however in the case of electronics, cross-contamination when two different solutions may pose an issue. Flexography (evolved from letterpress) can also be used for high volume printing for conductors and dielectrics. Screen printing is very commonly used though has a long setup time. Screen printing is a low cost method that is used for printing electronics. It involves silk screen printing of silver conductive paste into polyester. It can be used to print both single layer and multi layer designs on a variety of substrates and is a very efficient method however is restricted to printing only a single material. One of its biggest competitors is inkjet printing which will be explained in the following section.

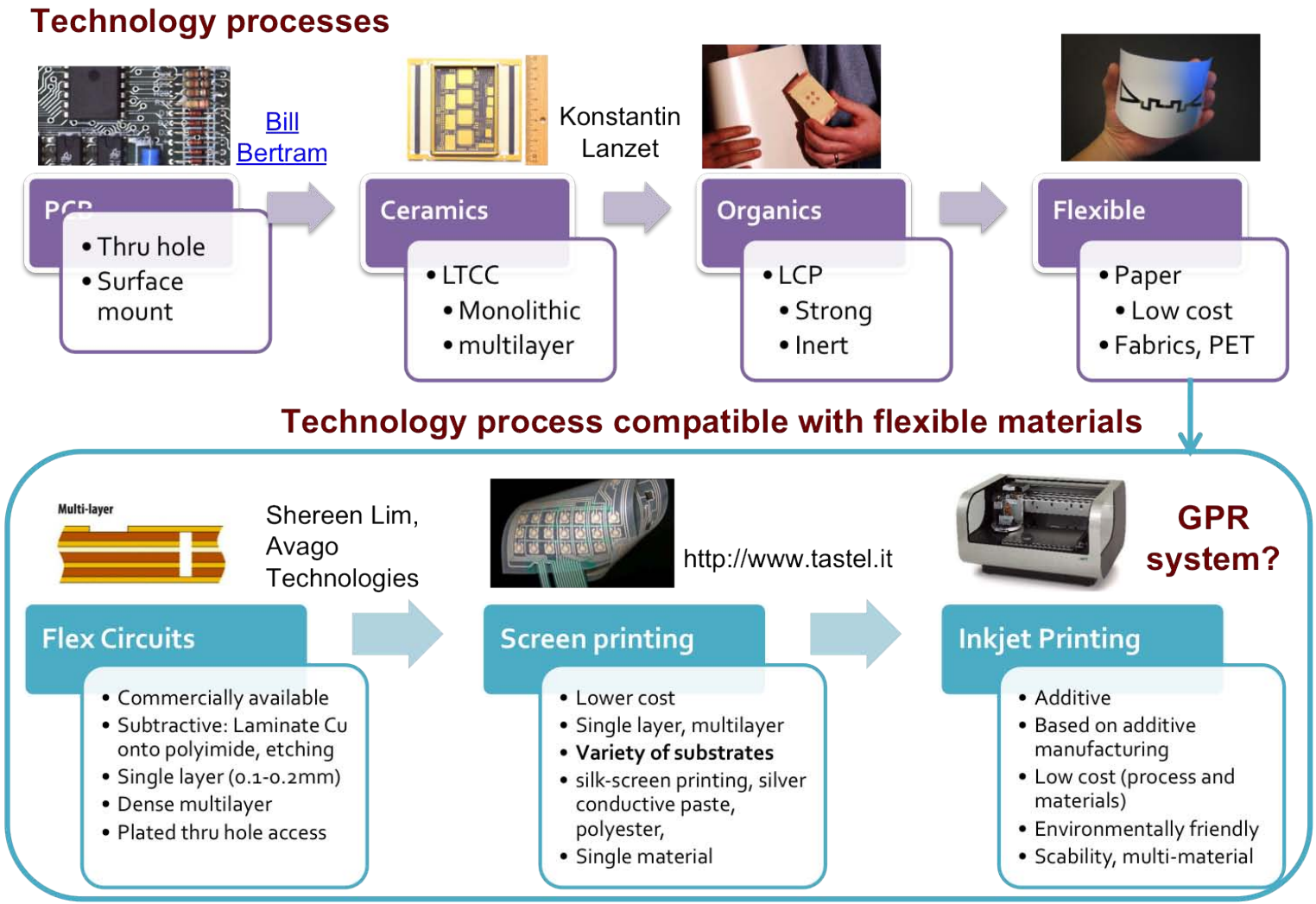

Fig. 1.15 Technology processes for rigid and flexible electronics.

1.2.4 Inkjet Printing

Inkjet printing is one of several nonimpact printing methods already used for flexible electronics and is based on additive manufacturing. Additive manufacturing and 3D printing in general is listed among top 10 breakthrough technologies of 2013 according to technologyreview. It has not only helped fabrication, allowing researches to realize more creative ideas in academia. It has also made a turnaround in industry: in design, manufacturing and performance. Additive manufacturing saves production cost and one way is by using less material. More complex shapes can be manufactured and finished parts can be lighter. Inkjet printing is a flexible and versatile method that is very commonly used, and though a complicated process in itself, is the easiest to setup compared to other methods in the printing industry. Inkjet Printing is at the moment used for low volume production as the speed and resolution is slower than the previous methods mentioned, however one of the most extraordinary features of inkjet printing is the multi-material capabilities. Materials that can be printed include organic and inorganic semiconductors, metallic conductors, nanoparticles and nanotubes. The multi-material capability is allowing inkjet printing to achieve a very high level of integration when it comes to realising devies ranging from antennas, to sensors and microfluidics devices (Figure 1.16). But how does one realize a complete radar system using inkjet printing?

Fig. 1.16 Integration levels of inkjet printing technology.

1.2.5 Research Focus: Hybrid Technology

In order to achieve the difficult task of realizing a large system using inkjet printing technology, this research uses the hybrid technology approach The hybrid approach is combining inkjet printing with off the shelf components (Figure 1.17). Why is this approach taken? For comparison, with inkjet printing technology one can realize transmission lines, antennas, passives (inductors and capacitors with Q factors of 20 up to several gigahertz) and 2D/3D interconnects. Printed transistors, using pentacene for instance are challenged by long channel length low electron mobility (5-10 cm^2Vs)

compared to silicon electronics (10,000 cm^2Vs), carbon nanotubes (100,000 cm^2Vs) and graphene (200,000 cm^2Vs). To realize a large high performance system using only inkjet printing technology is not yet possible. Using the hybrid approach, one can take advantage of the maturity of conventional CMOS ICs and quickly advance to a full high performance system while still taking advantage of the mechanical capabilities of flexible electronics. The hybrid approach simply works by printing the circuit footprint, assembling the components and applying a protective layer. The hybrid process however is anything but trivial. It requires having flexible/stable interconnects with good adhesion and resistance to cracking. Both the printed film and the components themselves should demonstrate strong adhesion to the substrate, without delamination, especially when flexing or rolling the devices. The hybrid approach also requires a low temperature assembly process that is compatible with both the flexible materials used as well as the off the shelf components. The process must be repeatable and reliable, and the structure itself must be robust, without and electrical or mechanical failure. In addition, component miniaturization is required in order to minimize the bending radius and handling small pin sizes with a nonstandard technology process is very challenging.

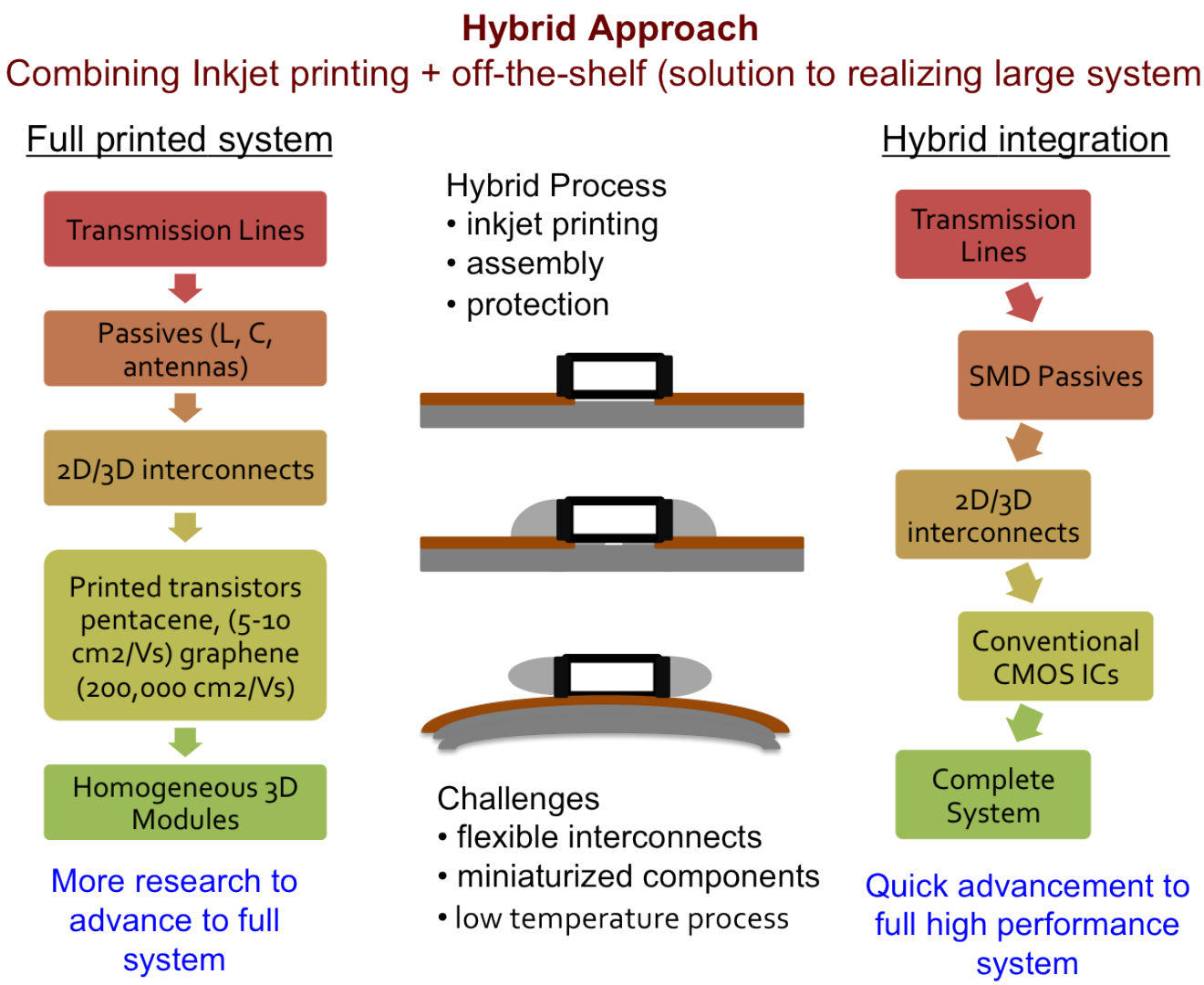

Fig. 1.17 Concept of hyrbrid approach.

To achieve ultra-portability for a GPR system, a new system packaging approach is taken to make the system rollable. For the first time, inkjet printing technology will be applied to the radar system. In doing this, the focus will be shifted to the system level design and performance of systems using current inkjet printing technology.

Chapter 2

System Design

2.1 System Overview

The system specifications for a SFCW/SFMCW GPR (stepped frequency modulated continuous wave ground penetrating radar) system designed specifically and exclusively for groundwater detection at large depths are established. These specifications provide a theoretical foundation to which the flexible monolithic ultra-portable ground penetrating radar using inkjet printing technology are be built upon.

The specifications are divided into six categories illustrated by color in Figure 2.1 which include: transmit waveform, power, signal propagation/loss/reflection, receiver design, digitization, signal processing; detection and finally the performance criteria. The establishment of the system specifications and selection or construction of hardware (Figure 2.1) were performed in parallel through multiple iterations in order to ensure that the requirements for the particular system could be meet with the available hardware components. The transmit waveform is controlled and limited by the DDS (Direct Digital Synthesizer) fed by a VCO reference clock. The DDS contains two outputs, the amplifier input and the the local oscillator which includes the in-phase channel (and optionally the quadrature channel when connecting the phase shifting circuit). The power stages include the power amplification stages that drive the transmit antenna, and the signal intercepted by the receive antenna. The signal propagation/loss/reflection stages are related to the soil environment and the reflection characteristics of the target, in this case groundwater. This stage is quantified by using a detailed ground model estimate, and experimentally validated using an indoor delay cable that simulates a particular target depth. The receiver is designed

to have the sensitivity, selectivity, gain and filtering for the adequate digitization and signal processing (ex. IFFT) necessary to interpret reflections. The system specifications are interrelated within one another, and the relationship between parameters established for this particular design is illustrated in Figure 2.2. The detection range is controlled by the soil environment and target reflection properties, the maximum sweep frequency, the transmitted power, the receiver design and the signal processing. The maximum unambiguous range is controlled by the modulation waveform and, in the case of SFCW, the frequency stepsize. The range resolution is determined by the sweep bandwidth, and sweep rate with the sweep rate also dictating the receiver bandwidth. An excel spreadsheet was used in order to calculate the specifications to establish operating points.

2.2 Waveform Specifications

The type of frequency modulation (Figure 2.3) will affect the unambiguous range, resolution and doppler tolerance. Sawtooth linear modulation is the most common type of modulation used and demonstrates the largest range however doppler components cannot be isolated from the beat frequency component and may lead to range ambiguities that vary in severity depending on doppler frequency and sampling. With triangular modulation, the doppler can be averaged out of the distance measurement (as long as the doppler frequency is smaller than the beat frequency) and both target range and velocity can be measured accurately. In this design, stepped triangular modulation was chosen as it demonstrated experimentally the most narrow spectrum in the chosen hardware configuration, in addition to the advantages mentioned above. A Direct Digital Synthesizer (AD9910) provides fine frequency resolution down to < 0.5 MHz and covers a frequency range of up to 400 MHz with reasonable spurious performance however a high level of spurious emissions were observed The AD9915 is suggested as an alternative as it provides improved spurious performance, and allows for frequency output of up to 1 GHz. Benchmarking spurious performance is very complicated and additional work has been done in [Kroupa 2000], [Kroupa 1993] and [Nicholas 1987]. A significant level of amplitude modulation was observed at the DDS output. This was due to a current controlled source at the output, and a capacitive termination that caused the output impedance to vary with frequency. The components for a buffer circuit were obtained in order to solve this issue. The maximum frequency was chosen in order to minimize subsurface attenuation, and maximize the reflection coefficient

System Specifications	
Transmit Waveform	
Modulation type	Stepped
Minimum frequency	f_{min}
Maximum frequency	f_{max}
Sweep bandwidth	B
Number of frequency points	N
Dwell time (at each freq)	t_d
Modulation period	T_m
Modulation frequency	f_m
Sweep period to TWT	T_m/τ
Power	
Transmit power	P_t
Antenna gain	G_{Tx}, G_{Rx}
Signal Propagation/Path Loss	
Attenuation/Skin depth	α, δ_s
Target RCS	σ
Target reflection	Γ
Receiver Design	
Receiver noise figure	NF
Conversion gain	G
Thermal noise	kTB_{IF}
Receiver sensitivity	S_{min}
Receiver bandwidth	B_{IF}
Maximum beat frequency	$f_{b,max}$
Beat frequency period	$1/f_b$
Sampling, Signal Processing	
ADC sampling frequency	f_s
FFT length	N/f_s
FFT gain, 10log(...)	N/2
FFT resolution	f_s/N
Performance	
Unambiguous range	R_{un}
Detection range	R_{max}
Range resolution	ΔR
Signal to Noise Ratio	SNR_{min}

Table 2.1 System specification list.

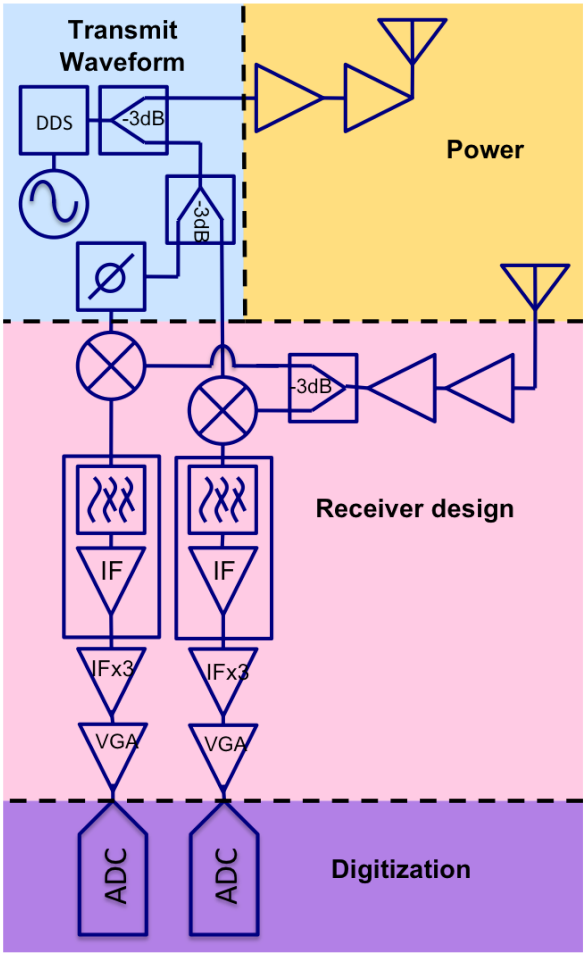

Fig. 2.1 General system architecture.

at the transition zone interface [Wolf 1937], [8]. The minimum frequency was then selected based on the chosen bandwidth to obtain the desired resolution and hardware capabilities. Finally, to avoid overlap of the RF or LO into the IF, it is confirmed that the minimum frequency will never cross into the IF bandwidth, which exists below 20 MHz in this system. The remaining waveform specifications were obtained using the

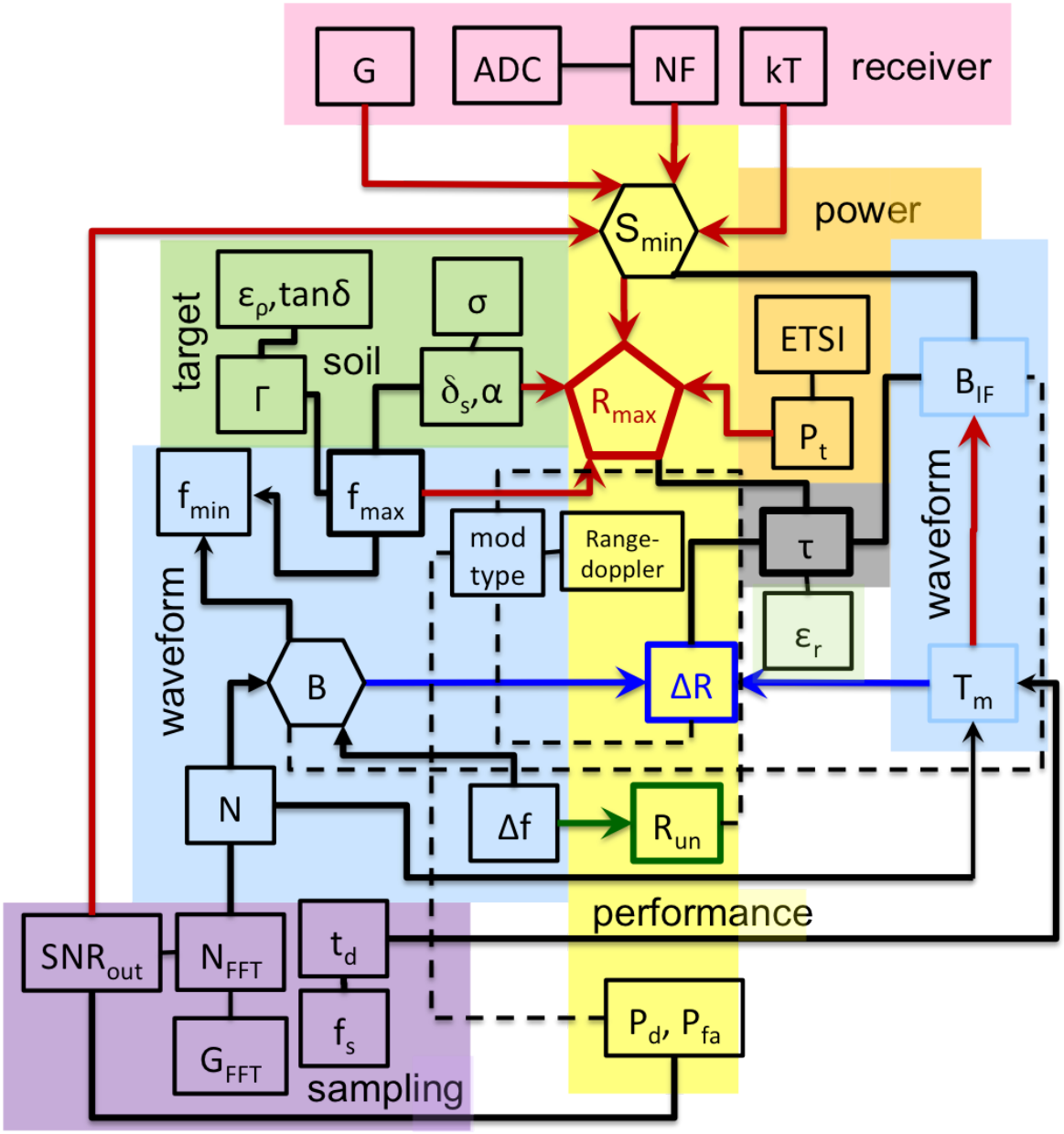

Fig. 2.2 Relationship between system specifications established for the specific SFCW GPR system under design.

classical FMCW equation which relates the sweep bandwidth B ($f_{max} - f_{min}$) and the modulation period T_m to the difference frequency fb and two-way travel time τ for a target at range R as seen in (2.2.1) and Figure 2.3a and Figure 2.3c

$$FMCW: \quad \frac{f_b}{\tau} = \frac{B}{T_m}, \; where \; \tau = \frac{2R}{v} \tag{2.2.1}$$

which is modified for the SFCW case by indicating Δf and t_d where $B = N\Delta f$ and $T_m = Nt_d$ as seen in (2.2.2) and Figure 2.3b and Figure 2.3c

$$SFCW: \quad \frac{f_b}{\tau} = \frac{\Delta f}{t_d}, \; where \; \tau = \frac{2R}{v} \tag{2.2.2}$$

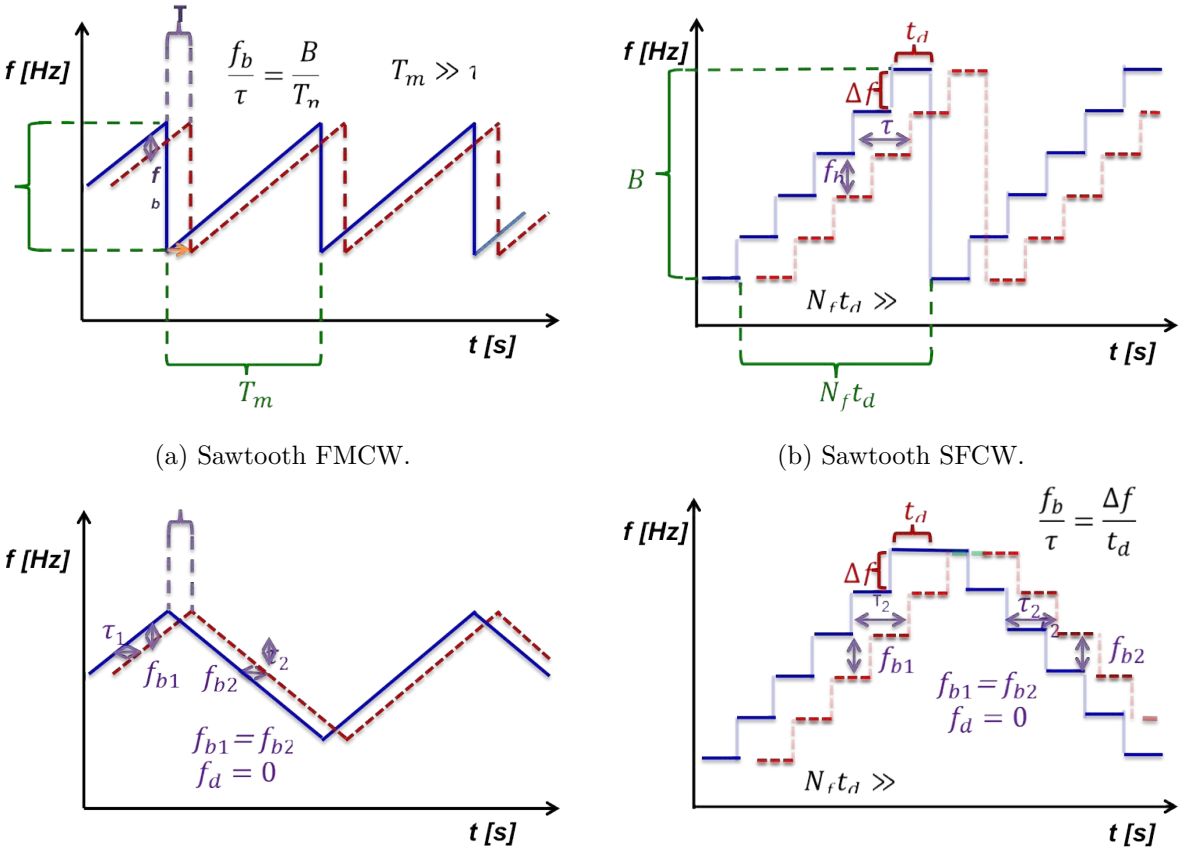

(a) Sawtooth FMCW.

(b) Sawtooth SFCW.

(c) Triangular FMCW.

(d) Triangular SFCW.

Fig. 2.3 Waveform.

The maximum beat frequency measured corresponds to the maxim range measured in (2.2.3)

$$R_{max} = \frac{vt_d}{2\Delta f} f_{b_{max}} \tag{2.2.3}$$

The SFCW frequency steps are synchronized with the ADC (one sample per step) in (2.2.4)

$$f_s = \frac{1}{t_d} \tag{2.2.4}$$

In order to avoid distortion in the IF beat frequency signal it is necessary to ensure that the number of frequency steps used, N, within a given sweep bandwidth $B = N\Delta f$ is large enough so that the dwell time t_d is less than the beat frequency period by satisfying (2.2.5)

$$t_d < \frac{1}{f_b} \tag{2.2.5}$$

Or more specifically, taking the ADC Nyquist criteria in (2.2.6)

$$\frac{f_s}{2} \geq f_{b_{max}} \tag{2.2.6}$$

and imposing it on the SFCW frequency stepping t_d by combining (2.2.4) and (2.2.6) to get (2.2.7)

$$5mm\frac{1}{2t_d} = f_{b_{max}} \tag{2.2.7}$$

By putting (2.2.7) into (2.2.6) gives the expression for the unambiguous range

$$R_{max} = \frac{vt_d}{2\Delta f}\left(\frac{1}{2t_d}\right) \tag{2.2.8}$$

$$R_{max} = \frac{v}{4\Delta f} \tag{2.2.9}$$

Since the phase shift is proportional to the target range $\Delta\phi = 2\pi\Delta f\tau$ where $\tau = \frac{2R}{v}$, $v = \frac{c}{\sqrt{\epsilon_r}}$ the frequency stepsize is chosen so that the $\Delta\phi < 2\pi$ over the desired unambiguous range. This is satisfied when $\frac{1}{\Delta f} > \tau$. The frequency stepsize should be small enough so that R_{un} exceeds the detection range. This particular system is designed to have a very long detection range therefore Table 2.2.

Δf_{max}		
R_{un} **[m]**	$\epsilon_r = 3$	$\epsilon_r = 15$
20	2.17	9.7
40	1.08	4.8
60	0.72	0.32
80	0.54	0.24
100	0.43	0.19

Table 2.2 Maximum unambiguous range versus frequency stepsize.

A frequency stepsize of no more than 1MHz is specified for the system. This was

experimentally validated (Figure 2.4) using a delay cable measurement (see Chapter 4), using a 47 m +/- 15cm cable ($\epsilon r \approx 2$) to simulate reflection from a subsurface target. Uniform frequency stepsizes of 1, 2, 3, 4 and 5MHz were used for three frequency sweeps of: 50-250 MHz, 50-300MHz and 50-400MHz corresponding to sweep bandwidths 200MHz (N = 200, 100, 67, 50, 40), 250MHz (N = 350, 175, 116, 88, 70) and 350 MHz (N =350, 175, 116, 88, 70) making a total of 15 measurements. Figure 2.4a shows the signal level versus frequency stepsize, Figure 2.4b shows the signal to noise ratio versus frequency stepsize and Figure 2.4c the range estimation error versus frequency stepsize. Figure 2.4d-Figure 2.4h show the beat frequency spectrums for each frequency stepsize for the sweep bandwidth of 350 MHz. As the frequency stepsize increases from 1MHz to 5MHz the signal level remains between -7 and -3dBFS however the SNR decreases from 10 dBFS to 6dBFS and the range estimatation error increases dramatically from 0m up to 200m. At Δf = 1MHz the cable length is estimated to 49 meters whereas for Δf = 5MHz estimated as 254 meters.

Number of frequency points and bandwidth

Using a frequency stepsize of 1MHz (corresponding to the number of frequency points, and assigned as a power of two), the range resolution versus bandwidth is shown in Table 2.3

range resolution ΔR[m] for $\Delta f_{DDS} = 1$ MHz B[MHz]= N_f			
B[MHz]= N_f	ΔR[m] ($\epsilon_r = 2$)	ΔR[m] ($\epsilon_r = 3$)	ΔR[m] ($\epsilon_r = 15$)
128	0.83	0.68	0.44
256	0.41	0.34	0.22
512	0.21	0.17	0.11

Table 2.3 Range resolution versus bandwidth for different material properties.

Dwell time

Sweeping too fast reduces the effective bandwidth (Figure 2.5a), so the required sweep rate needed to meaintain resolution is verified. The T_m/τ ratio required depends on the application, in particular to the target range. According to theory, a T_m/τ ratio of at least 30 is required (Figure 2.5b).

Figure 2.5 was also experimentally validated using using a 47 +/- 15cm cable ($\epsilon r \approx 2$) over the full extent of the DDS sweeping capabilities (Figure 2.6). The same

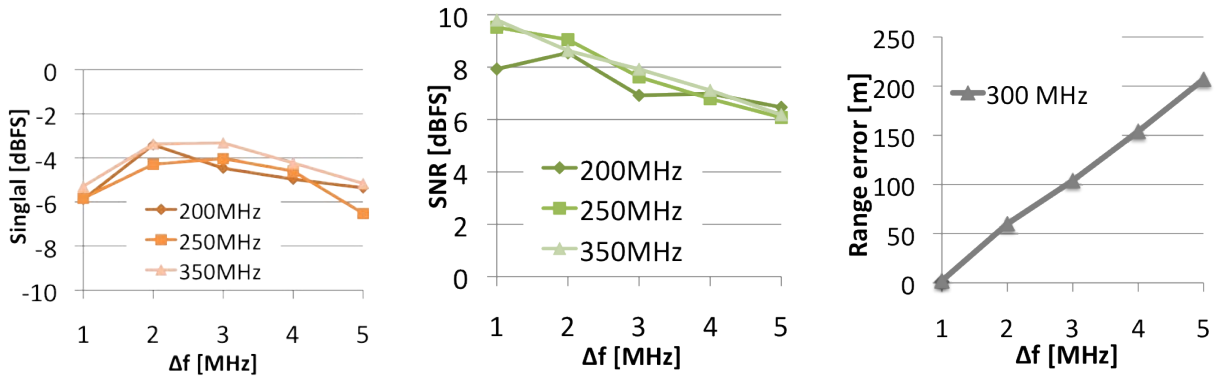

(a) signal vs Δf. (b) SNR vs Δf. (c) Range error vs Δf.

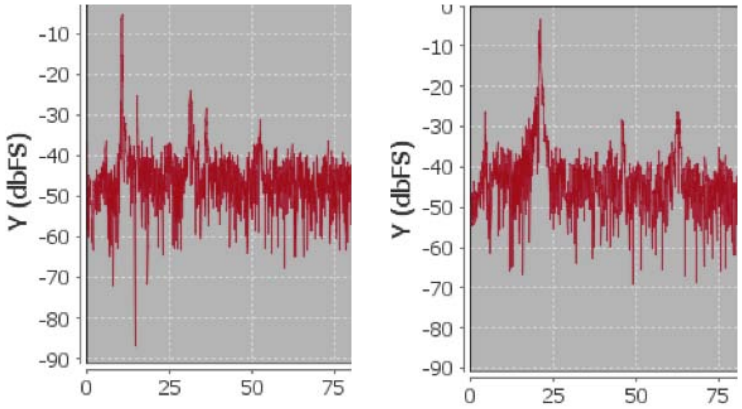

(d) $\Delta f = 1$ MHz, $f_b = 10$ MHz $L_{meas} = 49$ m (e) $\Delta f = 2$ MHz, $f_b = 21.7$ MHz $L_{meas} = 107$ m

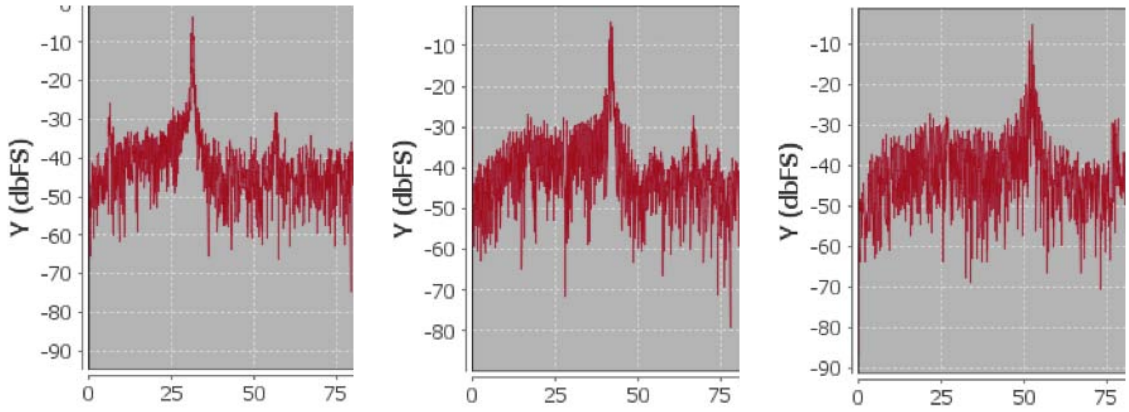

(f) $\Delta f = 3$ MHz, $f_b = 30.8$ MHz $L_{meas} = 151$ m (g) $\Delta f = 4$ MHz, $f_b = 41$ MHz $L_{meas} = 201$ m (h) $\Delta f = 5$ MHz, $f_b = 51.6$ MHz $L_{meas} = 254$ m

Fig. 2.4 Experimental validation of frequency stepsize Δf on range ambiguities.

frequency sweeps were used: 50-250MHz, 50-300MHz and 50-400MHz corresponding to bandwidths of 200MHz, 250MHz and 350 MHz. Figure 2.6a shows the signal level

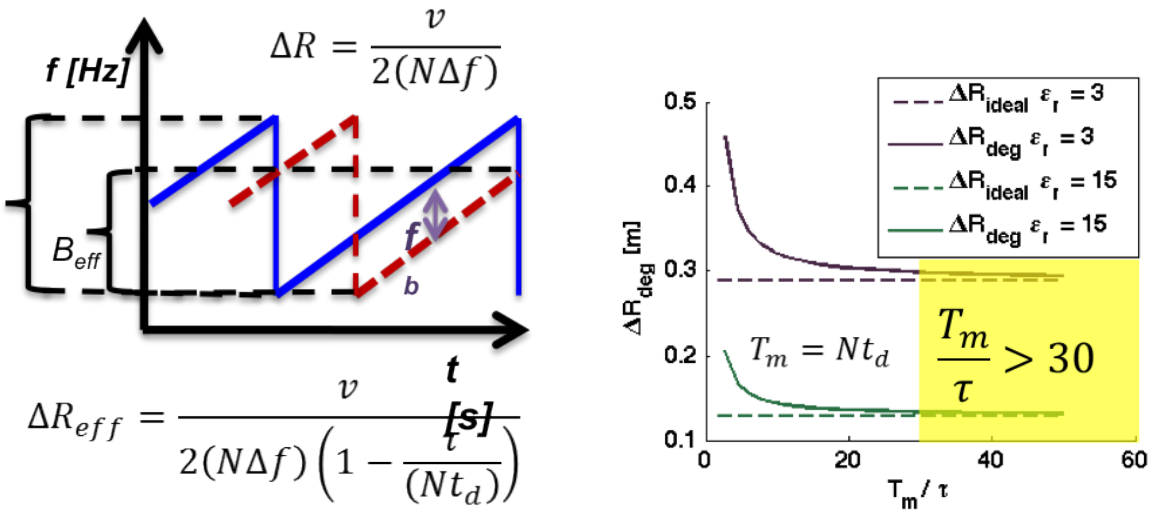

(a) effect of sweep rate on bandwidth and resolution

(b) calculated required T_m/τ ratio

Fig. 2.5 T_m/τ according to theory.

versus dwell time (ranging betweem -5 and -3 dBFS), Figure 2.6b shows the SNR versus dwell time. It can be seen that as the sweep rate decreases, the SNR increases from 6 dBFS and maximizes at 10dBFS in the Tm/tau < 30 region then levels off, confirming the theoretical estimation. Figure 2.6c-Figure 2.6g show the beat frequency spectrum for the 350MHz bandwidth measurement.

The expected beat frequencies for different target ranges and DDS sweep rate settings are shown in Table 2.4 and Table 2.5 for three different materials. This information is used to verify the low pass filters, of which the LT6600 Fully Differential 4th Order Lowpass Filter was used, each model permitting cutoff frequencies that include: 2.5 MHz, 5MHz, 10MHz, 15MHz and 20 MHz. A tunable filter may add versatility of the system.

It is noted that the required waveform specifications to maximize detection (or imaging) may vary greatly depending on soil conditions. Various operating modes may be needed if one wants to extract a very detailed image of the properties. Figure 2.6-FIgure 2.9 show operating modes for different groundwater scenarios, each list of specifications shows an illustration of the reflection coefficient as a function of frequency. Stepping through each different frequency slowly will result in a different amount of power reflected back, thus allowing the system to access more information about the groundwater source, however that can only be done operating within the cutoff frequency. In case 1 (Figure 2.6) where the transition zone height is small and

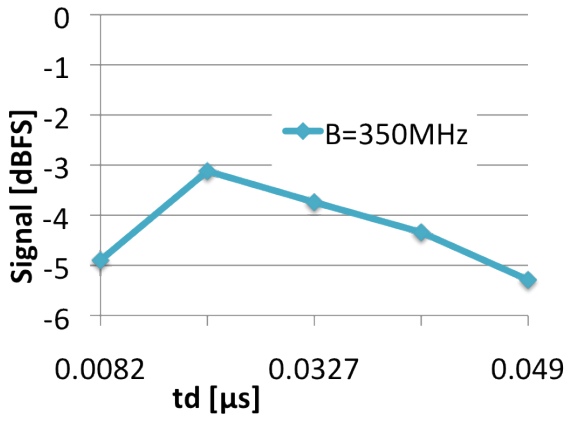

(a) signal vs t_d.

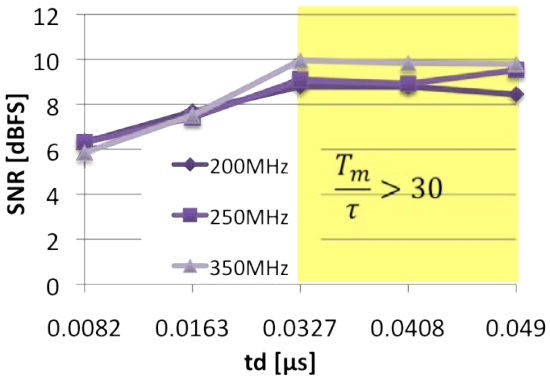

(b) SNR vs t_d.

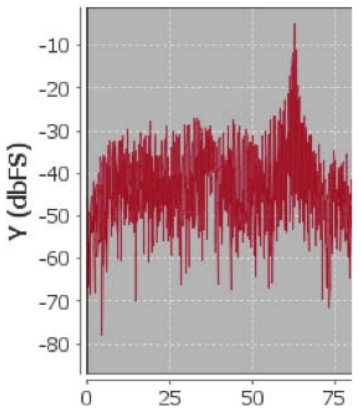

(c) L_{meas} = 51.0m

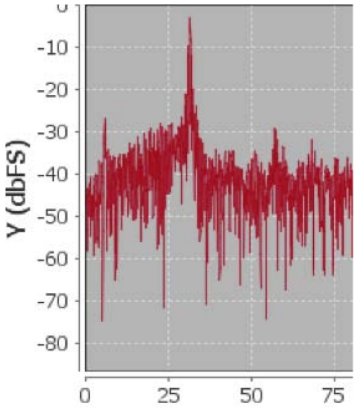

(d) L_{meas} = 50.2m

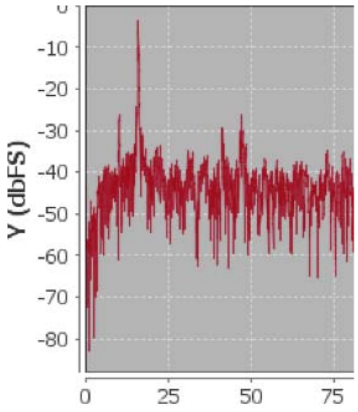

(e) L_{meas} = 49.5m

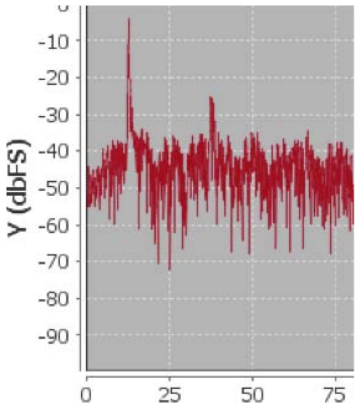

(f) L_{meas} = 47.1m

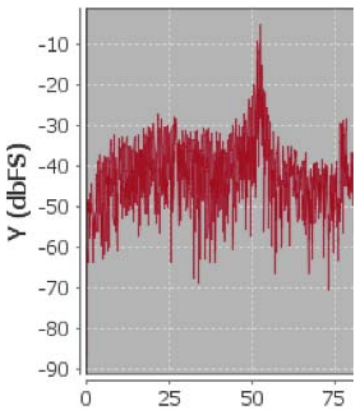

(g) L_{meas} = 54.1m

Fig. 2.6 Experimental validation of sweep period (or dwell time) on signal.

the soil dry (h = 0.1m, ϵr = 3), the transition zone cutoff frequency is 424 MHz and with the waveform specifications adjusted to operate within the 50-500MHz range as indicated in Figure 16a, the maximum unambiguous range is 43.3 meters, effective

Beat frequencies for B = 200 MHz, ϵ_r = **3)**					
Modulation, Target	R=10m τ=115ns	R=20m τ=231ns	R=30m τ=346ns	R=40m τ=462ns	R=50m τ=577ns
$t_d = 0.004\ \mu s$, $f_s = 250$MHz $T_m = 0.804\ \mu s$,$f_m = 1240$ kHz	28.72	57.45	86.17	114.90	143.62
$t_d = 0.008\ \mu s$, $f_s = 125$MHz $T_m = 1.61\ \mu s$,$f_m = 622$ kHz	14.36	28.72	43.09	57.45	71.81
$t_d = 0.016\ \mu s$, $f_s = 62.5$MHz $T_m = 3.22\ \mu s$,$f_m = 311$ kHz	7.18	14.36	21.54	28.72	35.90
$t_d = 0.032\ \mu s$, $f_s = 31.3$MHz $T_m = 6.43\ \mu s$,$f_m = 155$ kHz	3.59	7.18	10.77	14.36	17.95
$t_d = 0.064\ \mu s$, $f_s = 15.6$MHz $T_m = 12.9\ \mu s$,$f_m = 77.7$ kHz	1.80	3.59	5.39	7.18	8.98
$t_d = 0.128\ \mu s$, $f_s = 7.81$MHz $T_m = 25.7\ \mu s$,$f_m = 38.9$ kHz	0.90	1.80	2.69	3.59	4.49
$t_d = 0.256\ \mu s$, $f_s = 3.91$MHz $T_m = 51.5\ \mu s$,$f_m = 19.4$ kHz	0.45	0.90	1.35	1.80	2.24

Table 2.4 Beat frequencies f_b versus range R, (for ϵ_s = **3**)

Beat frequencies for B = 200 MHz, ϵ_r = **15)**					
Modulation, Target	R=10m τ=258ns	R=20m τ=516ns	R=30m τ=775ns	R=40m τ=1030ns	R=50m τ=1290ns
$t_d = 0.004\ \mu s$, $f_s = 250$MHz $T_m = 0.804\ \mu s$,$f_m = 1240$ kHz	64.23	128.46	192.69	256.91	321.14
$t_d = 0.008\ \mu s$, $f_s = 125$MHz $T_m = 1.61\ \mu s$,$f_m = 622$ kHz	32.11	64.23	96.34	128.46	160.57
$t_d = 0.016\ \mu s$, $f_s = 62.5$MHz $T_m = 3.22\ \mu s$,$f_m = 311$ kHz	16.06	32.11	48.17	64.23	80.29
$t_d = 0.032\ \mu s$, $f_s = 31.3$MHz $T_m = 6.43\ \mu s$,$f_m = 155$ kHz	8.03	16.06	24.09	32.11	40.14
$t_d = 0.064\ \mu s$, $f_s = 15.6$MHz $T_m = 12.9\ \mu s$,$f_m = 77.7$ kHz	4.01	8.03	12.04	16.06	20.07
$t_d = 0.128\ \mu s$, $f_s = 7.81$MHz $T_m = 25.7\ \mu s$,$f_m = 38.9$ kHz	2.01	4.01	6.02	8.03	10.04
$t_d = 0.256\ \mu s$, $f_s = 3.91$MHz $T_m = 51.5\ \mu s$,$f_m = 19.4$ kHz	1.00	2.01	3.01	4.01	5.02

Table 2.5 Beat frequencies f_b versus range R, (for ϵ_s = **15**)

range resolution is 0.256 maters, and beat frequency around 11.67 MHz. In case 2 with the same transition zone height but a damp soil environment (h = 0.3m, $\epsilon r = 15$. This decreases the velocity of propagation so the two-wave-travel time τ is increased from 404 ns to 904 ns. Maintaining the same T_m/τ ratio reduces the dwell time at

each frequency t_d, so the beat frequency will remain the same. The pulse length also becomes smaller due to decreasing velocity so the range resolution becomes finer (ΔR = 0.11m) which is an advantage. The decrease in wavelength however increased the phase shift between frequency steps and therefore reduced the unambiguous range Run from 63.34m to 19.3m which is no longer exceeds the target range of 35 meters. Also, increasing the dielectric constant of the subsurface decreases the transition zone cutoff. This means that the maximum sweep frequency needs to be reduced to be below the cutoff frequency. Changing the max sweep frequency f_{max} from 400 MHz to 200 MHz will increase the resolution from 0.11m to 0.26m. This is reasonable as it recuperates the original resolution of Case 1. The maximum unambiguous range is increased by keeping the same number of frequency points despite decreasing the bandwidth (the smaller frequency step-size reduces the phase shift between frequency steps bringing the maximum unambiguous range back up to 66.1m) Finally, the maximum beat frequency has reduced to 5 MHz and the configuration can be seen in Figure 2.7. Backing up to the subsurface conditions of case 1, in case 3 the height of the transition zone is increased (from 0.1m to 0.3m), reducing the transition zone cutoff frequency very significantly from 424 MHz down to 141 MHz, requiring a reduction in the maximum sweep frequency to around 130 MHz. Reducing f_{max} will decrease the bandwidth and pushes the already satisfactory resolution from 0.2559m to 1.1m. This resolution loss is more severe than in case 2 since the selected specifications did not have a superior resolution to start off with. The only way to improve the resolution again is to increase the bandwidth but this time by reducing the minimum sweep frequency f_{min}. Setting f_{min} = 30MHz the resolution returns only to 0.90m. Finally since Run has reached 221 meters, N can be reduced to 512 points, or even down to 128 points which will still satisfy the requirements in 2.2.14 to prevent distortion in the converted beat frequency signal. The final configuration is shown in Figure 2.8. Case 4 is demonstrates a damp subsurface and thick transition zone height (ϵr = 15, h = 0.3 meters). This case demonstrates a degradation in the ability to achieve high resolution (as in case 3) but maybe not quite as catastrophic. The transition zone thickening reduces the cutoff frequency from 424 MHz down to 87 MHz and the increase in ϵr improves the resolution from 0.25m to 0.11m. If the maximum sweep frequency from 400 MHz to 80 MHz the resolution is reduced from 0.11m to 1.3m. The minimum sweep frequency can be reduced from 50 MHz to say 25 MHz to gain back some resolution back to ΔR = 0.7824m. Unfortunately bandwidth is something there is little control over as seen in Case 3. Finally since Run has reached 221m, N can be reduced to 128 points since

such a large unambiguous range is unnecessary. The final configuration can be seen in Figure 2.9. The case 1 scenario was of an ideal, low ϵr material with minimum transition zone thickness. This allowed very relaxed restrictions on maximum frequency and the ability to achieve a very satisfactory range resolution with little effort. Case 2 stressed how reduced dielectric contrast between materials overall brings the need for lower frequencies (not just in the case of a transition zone). Case 3 and case 4 showed how the presence of, and thickening of a transition zone makes this low frequency requirement even stricter, therefore dominating the limit of the maximum frequency step, even when the neighboring subsurface above has a low ϵr. Regardless of ideal subsurface conditions, if a transition zone is present, the frequency will need to be reduced significantly but the resolution will be poor and difficult to recover simply by reducing fmin for a larger bandwidth, since bandwidth is something there is little freedom over. The system specifications have been chosen based on known prior knowledge of the subsurface and target properties, however these modes could be used in order to access or determine the properties as well.

Figure 2.7a shows a close view of the transmit frequency versus time for the chosen system configuration. Figure 2.7 displays matlab plots, calculated show the waveform properties on a realistic time and frequency scale for Case 1, using expressions from [60]. Figure 2.7b is of the transmitted waveform, Figure 2.7c the received waveform, Figure 2.7d the converted signal and Figure 2.7e the spectrum.

2.3 Radar Range Equation

The classical radar range expression (2.3.1) is used in the system analysis

$$S_{min} = \frac{P_t^{avg} G^2 e^{-4\alpha R} \lambda \sigma}{(4\pi)^3 R_{max}^4} \tag{2.3.1}$$

This expression has been modified (as is done in all applications) for the specific case of groundwater detection to (2.3.2) and (2.3.3). It takes into account the transmission loss from the air to the ground, the average power for the case of the SFCW radar (shown in Équation 13), the RCS for a planar interface (porportional to R^2 rather than R^4), the dependence of the reflection coefficient on frequency, transition zone height and material properties including water with frequency and temperature

dependent properties.

$$\left(kTB_{IF}F_N SNR_{min}^{out}\right) = \left[\frac{4Z_g Z_a}{|Z_g + Z_a|^2}\right]^4 = \frac{\left(P_{peak} \cdot \frac{Nt_d}{T_m}\right) G^2 e^{-(4\pi R)} \lambda}{(4\pi)^3 R_{max}^4} \sigma\left(R^2, R, \lambda\right) |\Gamma\left(\omega, h, \epsilon_s, \epsilon_w\left(\omega, T\right)\right)|^2 \tag{2.3.2}$$

Rearranging to separate system parameters from the material parameters.

$$\frac{\left(P_{peak} \cdot \frac{Nt_d}{T_m}\right) G^2}{\left(kTB_{IF}F_N SNR_{min}^{out}\right)} = \frac{(4\pi)^3 R_{max}^4}{\left[\frac{4Z_g Z_a}{|Z_g + Z_a|^2}\right]^4 e^{-(4\pi R)} \lambda \sigma\left(R^2, R, \lambda\right) |\Gamma\left(\omega, h, \epsilon_s, \epsilon_w\left(\omega, T\right)\right)|^2} \tag{2.3.3}$$

2.4 Transmitted Power

According to **??**, for a frequency range of 30-230MHz, the maximum allowed peak power = $PSD_{peak} \cdot B$ = -12dBm and the max allowed mean power = $PSD_{peak} \cdot B$ = -42 dBm. This system, however, is designed to be operated in a remote environment, therefore these limits may not apply. The system will be designed to transmit 20dBm of power, P1 = 20dBm. **The designers are however aware of these limits.** The average transmitted power for the SFCW case is clarified in Table 2.10. For the range expression, (2.4.1) is used as the average powr

General relationship		
average power transmitted over time $P_{avg} = \frac{E}{\tau i} = \frac{P_{peak} \cdot \text{pulse length}}{\tau_i}$ τ_i = coherent integration time		
	Impulse	**SFCW**
peak power	P_{peak}	P_{peak}
pulses per second	PRF	$1/t_d$
time between pulses	PRI	t_d
coherent integration time	PRI	T_m
pulse length	τ_p	$N \cdot t_d$
energy	$P_{peak} \cdot \tau_p$	$P_{peak} \cdot Nt_d$
average power	$P_{peak} \cdot \frac{\tau_p}{PRI}$	$P_{peak} \cdot \frac{Nt_d}{T_m} \approx P_{peak}$

Table 2.10 Average power.

$$P_t^{avg} = \frac{E}{\tau_i} = \frac{P_{peak} \cdot \text{pulse length}}{\tau_i} = P_{peak} \cdot \frac{Nt_d}{T_m} \tag{2.4.1}$$

2.5 Soil Environment and Target Reflection

2.5.1 Soil and Water Properties

The soil material properties were taken from measured data in [L'Assembleedesradiocommunicationsd 2000]. The properties for dry soil ($\epsilon r \approx 3$) and damp soil ($\epsilon r \approx 15$) are indicated in 2.11. The electrical properties of dry soil remain constant over frequency but in wet soil the addition of mosture causes the conductivity to increase with frequency. The frequency and temperature dependence of the complex permittivity of water (Figure 2.8) was calculated using the well known debye expression [13] and is shown in Figure 2.8a and Figure 2.8b. For GPR frequencies commonly used (Figure 2.8c and Figure 2.8d), the dielectric constant remains constant versus frequency but changes over temperature and the conductivity and dielectric tangent increase with frequency (and also display temperature dependence). The complex permittivity of water falls around 80 – j0.22 with a variation with temperature (the real part decreases with temperature and the imaginary part also decreases with temperature), the numerical values are shown in 2.13

2.5.2 Ground Model

A groundwater model (Figure 2.9b) was formed in order to bechmark the radar environment (the soil) and target properties (the groundwater) to compute the path loss (Figure 2.9a). Ground models vary depending on the application (geophysics, radar, etc. . .) where each application focuses on a particular physical quantity that distinguishes each region of the subsurface (for example temperature, electrical, moisture, porosity). In this work, an electrical groundwater model was formed by dividing the subsurface into four different layers, each layer having different electrical properties. Above the surface is 1) air, with the impedance of freespace. The vadose zone consists of the 2) a homogeneous upper layer of dry sand having residual saturation. This layer has low to moderate loss depending on not the sand is dry ($\epsilon_r \approx 3$) or contains some moisture, in this case, damp or wet soil ($\epsilon_r \approx 15$) and 2) an inhomogeneous transition zone about 30 to 40cm thick [10] where the water content (and ϵ_r) increase with depth. Depending on the application, the capillary fringe is included in either the va-

Soil Material Properties			
constants $\epsilon_0 = 8.854x10^{-12}$, $\mu_0 = 4\pi x10^{-7}$, $Z_0 = 377\Omega$, $c = 3x10^8$			
Test frequency	**50 MHz**	**250 MHz**	**400 MHz**
Dielectric constant (measured data from [29])			
Dry soil	3		
Damp soil	15		
Propagation velocity [m/s]			
Dry soil	1.73		
Damp soil	7.75		
Wavelength [m]			
Dry soil	3.46	0.69	0.43
Damp soil	1.55	0.31	0.19
Soil conductivity [S/m] (measured data from [29])			
Dry soil	0.001		
Damp soil	0.013	0.05	0.09
Soil skin depth [m] (measured data from [29])			
Dry soil	90		
Damp soil	9	3	2
Loss tangent: $tan\delta = \frac{\sigma}{\omega\epsilon_0\epsilon_r}$			
Dry soil	0.120	0.024	0.015
Dry soil	0.312	0.240	0.270
Impedance: $Z = \sqrt{2}\frac{\mu_0\mu_r}{\epsilon_0\epsilon_r}\sqrt{2}\frac{1}{1-jtan\delta}$			
Dry soil	216.4 + j12.9	217.5 + j2.6	217.5 + j1.6
Damp soil	94 + j14.3	95.2 + j11.3	94.8 + j12.6

Table 2.11 Soil Properties.

dose zone or saturation zone, or just treated as a boundary condition. The rest of the saturation zone consists of 4) the water table and water source which is fully saturated and lossy ($\epsilon_r \approx 81$). The electrical properties vary as a function of frequency, salinity and temperature [13] as mentioned in the previous section. Using this ground model, the path loss was estimated in order to determine the receiver sensitivity required.

It is assumed that the antenna will be placed directly onto the ground, in order to minimize ground reflections and ensure that the maximum amount of radiation is absorbed into the subsurface (Figure 20a). The power in the direction of the target is defined by the antenna gain and the power transmitted into the ground is defined by the impedance of freespace and the soil environment subsurface (Figure 20b). The amount of power lost from air to dry soi is 0.65 dB and from air to damp soil is 3.8dB for most GPR frequencies.

Power Transmitted into the Ground

It is assumed that the antenna will be placed directly onto the ground, in order to minimize ground reflections and ensure that the maximum amount of radiation is absorbed into the subsurface (Figure 2.10a). The power in the direction of the target is defined by the antenna gain and the power transmitted into the ground is a result in the impedance difference between the air and soil (Figure 2.10b). The amount of power lost from air to dry soi is 0.65 dB and from air to damp soil is 3.8dB for most GPR frequencies.

Path Loss through spreading and attenuation

The path loss through the soil environment is due to spreading and attenuation. Figure 2.11 displays the two-way attenuation and spreading loss as a function of exploration range for different frequencies. It can be seen that for dry soil, at all frequencies, the loss remains less than 100dBm. If the soil contains moisture, however, the rate of loss rapidly increases, and frequencies below 50 MHz are needed to significantly penetrate the soil.

Target Reflection

The water properties are used in the computation of the reflection coefficient [Wolf 1937], [Officer 1958], and [8] at the groundwater source. In the case of a simplified ground model that consists of a sharp interface between soil and water, the reflection coefficient was determined based on the properties of the soil and water alone. The complex impedance of water falls around 41.5 + j0.06 with a slight variation with temperature and frequency (the real part increases with temperature, and imaginary part decreases with temperature). The complex reflection coefficient between dry sand and water falls around -0.68 – j0.02 with a slight variation with temperature (the real part decreases with temperature and the imaginary increases with temperature). The power reflection coefficient between dry soil and water ranges from 0.47 to 0.44, decreasing with temperature (Table 2.14). The impedance of damp sand falls around 93.510795 + 15.194344i at 400 MHz. The reflection coefficient between damp sand and water is around -0.4-j0.06 with a slight variation with temperature (the real part increasing with temperature and imaginary part decreasing with temperature). The power reflection coefficient for damp soil to water ranges fom 0.16 to 0.14, decreasing with temperature (Table 2.14). In the case that a transition zone exists, the reflec-

tio coefficient will have a very strong frequency dependence and is illustrated more clearly in Figure 22a-d illustrates more clearly the reflection coeffient versus frequency calculated from [Wolf 1937], [Officer 1958], and [8]. The expression calculates a velocity gradient using a spatial average. The reflection coefficient demonstrates low pass behavior with a first cutoff frequency defined where the reflection coefficient goes to zero (Figure 2.12). It can be seen that when observing Figure 2.12a-Figure 2.12c and Figure 2.12b-Figure 2.12d which compares dry soil to damp soil, the cutoff frequency is reduced. When observing Figure 2.12a-Figure 2.12b to Figure 2.12c-Figure 2.12d, which compares a thin transition zone height to a thick transition zone height, a more significant reduction in the cutoff frequency is observed.

sharp interface

$$\Gamma = \frac{Z_{water} - Z_{soil}}{Z_{water} + Z_{soil}}$$

transition zone

$$\Gamma(\omega) = \frac{1}{2\frac{j\omega}{a} + \frac{m(v_w^m + v_s^m)}{(v_w^m - v_s^m)}},\ \textit{where}\ m = 2\sqrt{\frac{1}{4} - \frac{\omega^2}{a^2}},\ \textit{and}\ a = \frac{v_w - v_s}{h}$$

Power reflection coefficient $\lvert\Gamma\rvert^2$ from {dry} soil to water									
	h = 0 m			**h = 0.1 m**			**h = 0.3 m**		
$\circ C$	**50 MHz**	**250 MHz**	**400 MHz**	**50 MHz**	**250 MHz**	**400 MHz**	**50 MHz**	**250 MHz**	**400 MHz**
1	0.4721	0.4728	0.4730	0.4615	0.1977	0.0054	0.3702	0.0093	0.0015
6	0.4686	0.4693	0.4694	0.4581	0.1974	0.0058	0.3676	0.0097	0.0017
11	0.4644	0.4651	0.4652	0.4540	0.1968	0.0063	0.3645	0.0102	0.0020
16	0.4607	0.4614	0.4614	0.4504	0.1962	0.0067	0.3618	0.0107	0.0022
21	0.4564	0.4570	0.4571	0.4462	0.1955	0.0072	0.3586	0.0112	0.0025
26	0.4518	0.4524	0.4524	0.4417	0.1946	0.0077	0.3552	0.0117	0.0028
31	0.4472	0.4478	0.4478	0.4372	0.1937	0.0083	0.3518	0.0121	0.0032
36	0.4436	0.4442	0.4442	0.4337	0.1929	0.0087	0.3491	0.0125	0.0034
Reflection coefficient $\lvert\Gamma\rvert^2$ from {wet} soil to water									
1	0.1691	0.1691	0.1678	0.1548	0.0003	0.0073	0.0555	0.0002	0.0005
6	0.1659	0.1660	0.1649	0.1519	0.0004	0.0074	0.0549	0.0002	0.0006
11	0.1621	0.1623	0.1612	0.1484	0.0004	0.0074	0.0542	0.0003	0.0006
16	0.1588	0.1590	0.1580	0.1454	0.0005	0.0074	0.0535	0.0003	0.0007
21	0.1549	0.1552	0.1543	0.1419	0.0006	0.0073	0.0527	0.0004	0.0007
26	0.1508	0.1511	0.1503	0.1382	0.0007	0.0072	0.0519	0.0005	0.0007
31	0.1468	0.1471	0.1464	0.1346	0.0008	0.0071	0.0510	0.0005	0.0007
36	0.1437	0.1440	0.1433	0.1318	0.0009	0.0070	0.0503	0.0006	0.0007

Table 2.14 Reflection coefficient from soil to water.

Backscatter Cross Section

Electromagnetic waves that encounter a large body of groundwater will see a lossy planar interface rather than a single point target. Therefore the power reflected from a rough planar surface will decrease by R^2, from a smooth planar surface by R^3 and from a point source R^4. The backscatter cross section will vary depending on the frequency, target distance and surface roughness and material properties (Table 2.15). This is why prior information about the groundwater source is accessed when using GPR systems. The calculated reflection coefficient values (see section Target Reflection) can be inserted into these expressions. The backscatter cross section (not including the reflection coefficient) for different subsurface targets and operating frequencies is shown in Table 2.15.

Backscatter cross section $10log\left(\sigma\|\Gamma\|^2\right)$ = backscatter cross section [dBm^2] σ = scattering cross section $[m^2]$ $\|\Gamma\|^2$ = backscatter gain			
Smooth planar reflector	$\sigma\|\Gamma\|^2 = \pi R^2\|\Gamma\|^2$		
Rough planar reflector	$\sigma\|\Gamma\|^2 = \pi\left(\left(\frac{\lambda}{4}\right)^2 + \frac{\lambda R}{2}\right)\|\Gamma\|^2$ $\sigma\|\Gamma\|^2 = \frac{\pi\lambda R}{2}\|\Gamma\|^2$		
Spherical (point)	$\sigma\|\Gamma\|^2 = \pi a^2\|\Gamma\|^2$		
Scattering cross section σ $[m^2]$			
R = 30m	50 MHz	250 MHz	400 MHz
Smooth planar target	2827	2827	2827
Rough planar target (dry soil)	166	33	20
Rough planar target (wet soil)	74	15	9

Table 2.15 Scattering cross section calculated from [42, 83, 93]

2.5.3 Power at Each Stage

The power at each stage is shown in Tables 2.16 and Tables 2.17 for a smooth planar, rough planar or point target located 30 meters deep below the subsurface for different transition zone heights (though do not apply for a point target but are still included for comparison), and for three different operating frequencies. As expected, the reflection from a planar surface is obviously larger than that of a point surface, and even larger for a rough planar surface. The amount of power lost due to transmission from the air-to-ground or vice versa is the least compared to other stages. The majority of

the loss is due to the signal attenuation, as can be seen when comparing the path loss undergone in dry soil versus wet soil, particularly for higher frequencies. The next largest amount of path loss occurs due to the existence of a transition zone, rapidly increasing as the height of the transition zone increases. The power received versus target depth can be seen in Figure 2.13 for dry soil (Figure 2.13a) and wet soil (Figure 2.13b). Various targets and soil conditions in Figure 2.14 and Figure 2.15.

Power at each stage (dry soil)									
	h = 0m			**h = 0.1m**			**h = 0.3m**		
Frequency	**50 MHz**	**250 MHz**	**400 MHz**	**50 MHz**	**250 MHz**	**400 MHz**	**50 MHz**	**250 MHz**	**400 MHz**
Smooth planar reflector									
Transmitted	20	20	20	20	20	20	20	20	20
In target direction	26	26	26	26	26	26	26	26	26
Into ground	25.4	25.4	25.4	25.4	25.4	25.4	25.4	25.4	25.4
Incident on target	-18.1	-18.1	-18.1	-18.1	-18.1	-18.1	-18.1	-18.1	-18.1
Reflected by target	-21.5	-21.5	-21.5	-21.6	-25.2	-39.5	-22.5	-37.6	-44.1
Reflected by target towards receiver	13.0	13.0	13.0	12.9	9.35	-5	12	-3.1	-9.5
Power to surface	-30.4	-30.4	-30.4	-30.5	-34.1	-48.4	-31.5	-46.5	-53
Power to air	-31.0	-31.0	-31.0	-31.2	-34.7	-49.1	-32.1	-47.2	-53.6
Power to receiver	-29.4	-30.7	-30.8	-29.5	-34.4	-48.9	-30.5	-46.8	-53.4
Rough planar reflector									
Transmitted	20	20	20	20	20	20	20	20	20
In target direction	26	26	26	26	26	26	26	26	26
Into ground	25.4	25.4	25.4	25.4	25.4	25.4	25.4	25.4	25.4
Incident on target	-18.1	-18.1	-18.1	-18.1	-18.1	-18.1	-18.1	-18.1	-18.1
Reflected by target	-21.5	-21.5	-21.5	-21.6	-25.2	-39.5	-22.5	-37.6	-44.1
Reflected by target towards receiver	0.69	-6.33	-8.37	0.61	-10.0	-26.4	-0.34	-22.5	-30.9
Power to surface	-42.7	-49.8	-51.8	-42.8	-53.5	-69.8	-43.8	-65.9	-74.4
Power to air	-43.4	-50.4	-52.5	-43.5	-54.1	-70.5	-44.4	-66.5	-75.0
Power to receiver	-41.7	-50.1	-52.3	-41.8	-53.8	-70.3	-42.8	-66.2	-74.8
Point target									
Transmitted	20	20	20	20	20	20	20	20	20
In target direction	26	26	26	26	26	26	26	26	26
Into ground	25.4	25.4	25.4	25.4	25.4	25.4	25.4	25.4	25.4
Incident on target	-18.1	-18.1	-18.1	-18.1	-18.1	-18.1	-18.1	-18.1	-18.1
Reflected by target	-21.5	-21.5	-21.5	-21.6	-25.2	-39.5	-22.5	-37.6	-44.1
Power to surface	-64.9	-64.9	-64.9	-65.0	-68.6	-82.9	-66	-81.0	-87.5
Power to air	-65.6	-65.6	-65.6	-65.7	-69.3	-83.6	-66.6	-81.7	-88.1
Power to receiver	-63.9	-65.2	-65.4	-64.0	-68.9	-83.4	-65	-81.4	-87.9

Table 2.16 Power at each stage (dry soil).

Power at each stage (wet soil)									
	h = 0m			**h = 0.1m**			**h = 0.3m**		
Frequency	**50 MHz**	**250 MHz**	**400 MHz**	**50 MHz**	**250 MHz**	**400 MHz**	**50 MHz**	**250 MHz**	**400 MHz**
Smooth planar reflector									
Transmitted	20	20	20	20	20	20	20	20	20
In direction of target	26	26	26	26	26	26	26	26	26
Into ground	22.2	22.3	22.2	22.2	22.2	22.2	22.2	22.2	22.2
Incident on target	-47.3	-105	-149	-47.3	-105	-149	-47.3	-105	-149
Reflected by target	-55.7	-113	-157	-55.8	-137	-170	-60.1	-139	-180
Reflected by target towards receiver	-21.1	-78.9	-122	-21.3	-103	-136	-25.6	-105	-146
Power to surface	-90.6	-206	-293	-90.7	-230	-306	-95.0	-232	-316
Power to air	-94.4	-210	-297	-94.5	-234	-310	-98.8	-236	-320
Power to receiver	-93.7	-210	-297	-93.8	-234	-310	-98.1	-236	-320
Rough planar reflector									
Transmitted	20	20	20	20	20	20	20	20	20
In direction of target	26	26	26	26	26	26	26	26	26
Into ground	22.2	22.2	22.2	22.2	22.2	22.2	22.2	22.2	22.2
Incident on target	-47.3	-105	-149	-47.3	-105	-149	-47.3	-105	-147
Reflected by target	-55.6	-113	-157	-55.8	-137	-170	-60.1	-139	-180
Reflected by target towards receiver	-37	-102	-147	-37.1	-126	-161	-41.4	-127	-171
Power to surface	-107	-229	-318	-107	-253	-331	-111	-255	-341
Power to air	-110	-233	-322	-110	-257	-335	-115	-259	-345
Power to receiver	-110	-232	-322	-110	-257	-335	-114	-259	-345
Point target									
Transmitted	20	20	20	20	20	20	20	20	20
In direction of target	26	26	26	26	26	26	26	26	26
Into ground	22.2	22.2	22.2	22.2	22.2	22.2	22.2	22.2	22.2
Incident on target	-47.3	-105	-149	-47.3	-105	-149	-47.3	-105	-149
Reflected by target	-55.7	-114	-157	-55.8	-137	-170	-60.1	-139	-180
Power to surface	-125	-241	-328	-125	-265	-341	-130	-267	-351
Power to air	-129	-245	-332	-129	-269	-345	-133	-270	-355
Power to receiver	-129	-244	-331	-128	-268	-345	-133	-270	-355

Table 2.17 Power at each stage (wet soil).

Dry soil, thin transition	
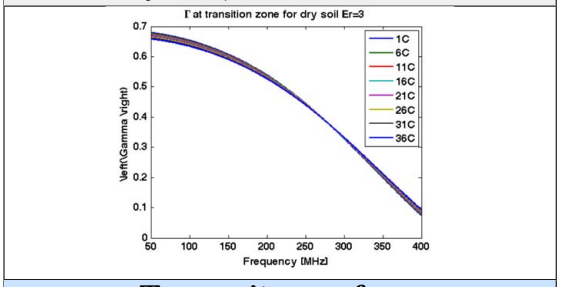	
Transmit waveform	
Minimum frequency	50 MHz
Maximum frequency	400 MHz
Bandwidth	350 MHz
Number of frequency points	512 points
Dwell time (at each freq)	0.0237 μs
Modulation period	12.12 μs
Modulation frequency	>82 kHz
Digitization	
ADC sampling frequency	42 MHz
Measurements	
Unambiguous range	63 m
Detection range	>50 m
Range resolution	>25 cm
Signal to Noise Ratio	-24 dB

Table 2.6 System specifications (case 1).

Wet soil, thin transition	
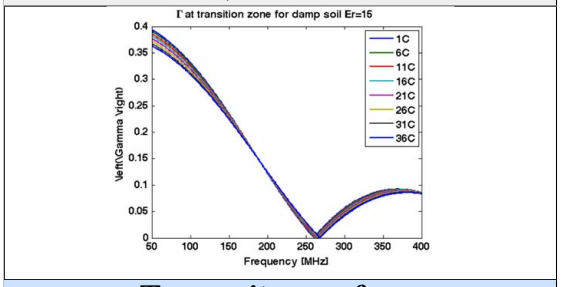	
Transmit waveform	
Minimum frequency	50 MHz
Maximum frequency	200 MHz
Bandwidth	150 MHz
Number of frequency points	512 points
Dwell time (at each freq)	0.0530 μs
Modulation period	27.11 μs
Modulation frequency	» 37 kHz
Digitization	
ADC sampling frequency	20 MHz
Measurements	
Unambiguous range	66 m
Detection range	>30 m
Range resolution	>25 cm
Signal to Noise Ratio	-24 dB

Table 2.7 System specifications (case 2).

Dry soil, thick transition	
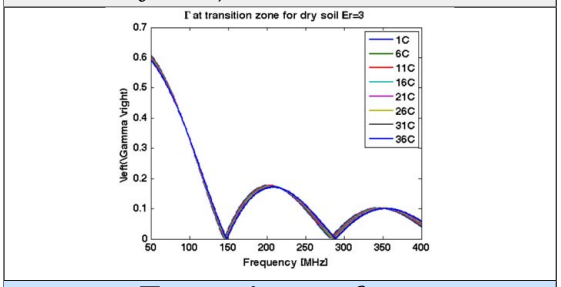	
Transmit waveform	
Minimum frequency	30 MHz
Maximum frequency	130 MHz
Bandwidth	100 MHz
Number of frequency points	128 points
Dwell time (at each freq)	0.0947 μs
Modulation period	12.12 μs
Modulation frequency	>82 kHz
Digitization	
ADC sampling frequency	10 MHz
Measurements	
Unambiguous range	55 m
Detection range	>50 m
Range resolution	>90 cm
Signal to Noise Ratio	-18 dB

Table 2.8 System specifications (case 3).

Wet soil, thick transition	
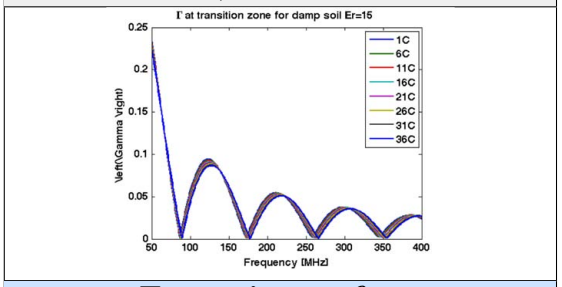	
Transmit waveform	
Minimum frequency	25 MHz
Maximum frequency	80 MHz
Bandwidth	55 MHz
Number of frequency points	128 points
Dwell time (at each freq)	0.2118 μs
Modulation period	27.11 μs
Modulation frequency	>37 kHz
Digitization	
ADC sampling frequency	5 MHz
Measurements	
Unambiguous range	63 m
Detection range	>45 m
Range resolution	>30 cm
Signal to Noise Ratio	-18 dB

Table 2.9 System specifications (case 4).

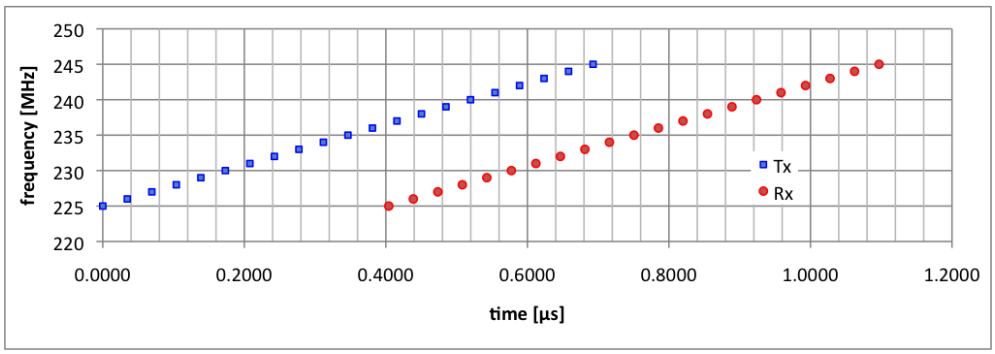

(a) Tx/Rx frequency versus time (to scale).

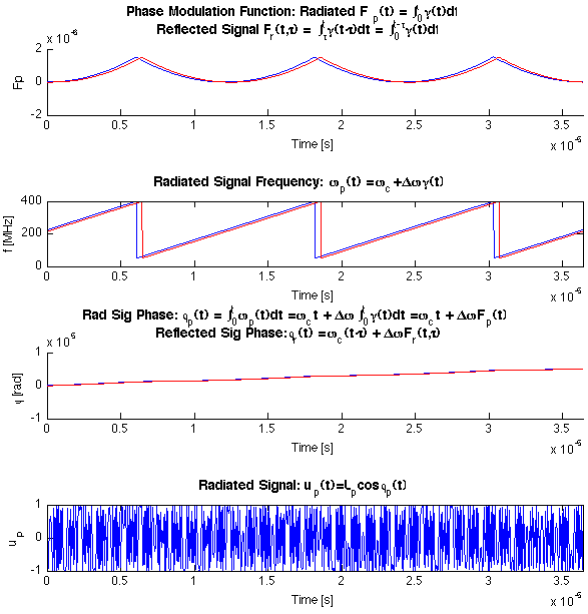

(b) transmit

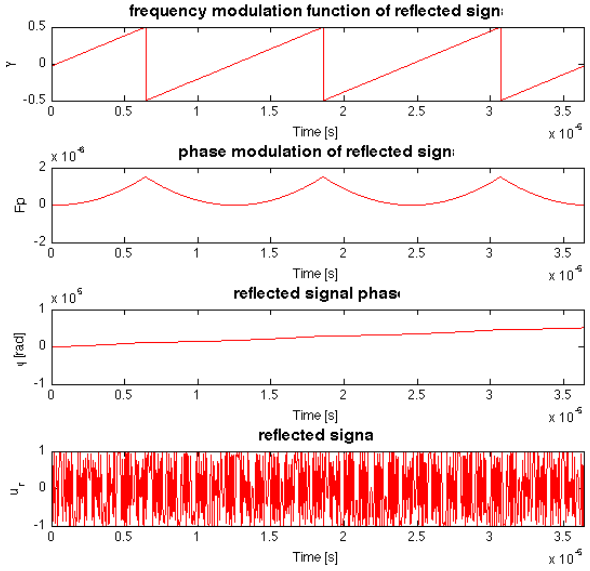

(c) receive

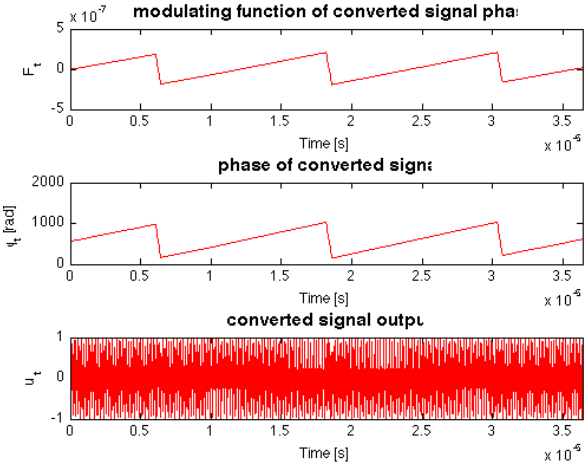

(d) converted

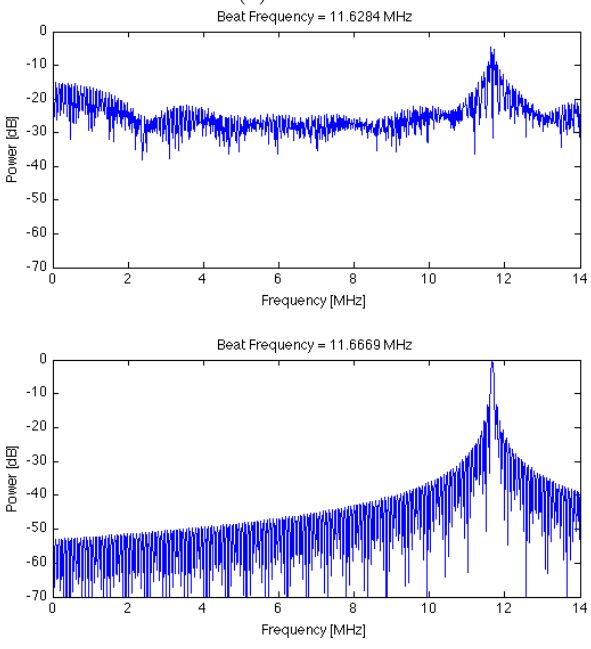

(e) spectrum

Fig. 2.7 Waveform properties to scale calculated using [60].

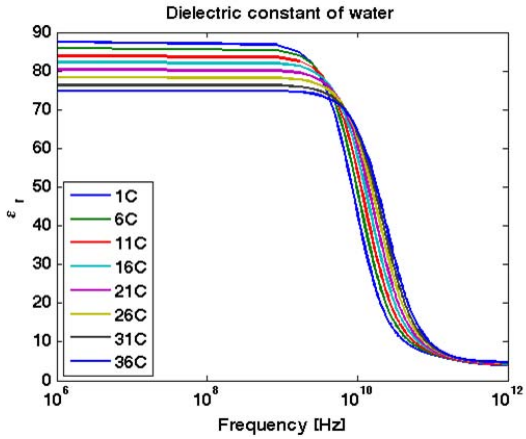

(a) dielectric constant versus frequency

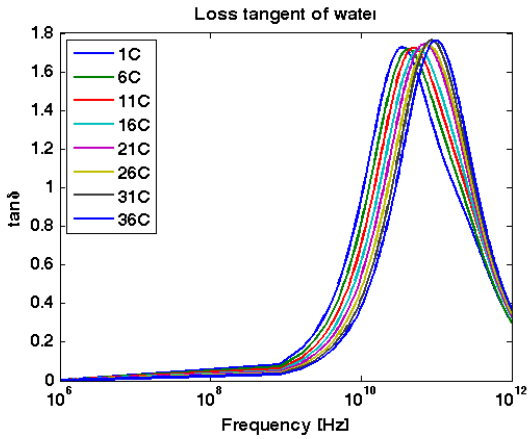

(b) loss tangent versus frequency

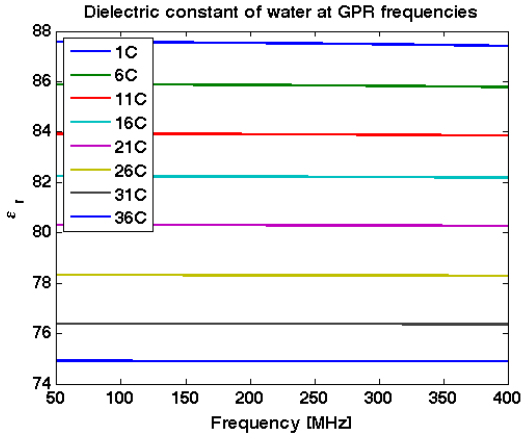

(c) dielectric constant at GPR frequencies

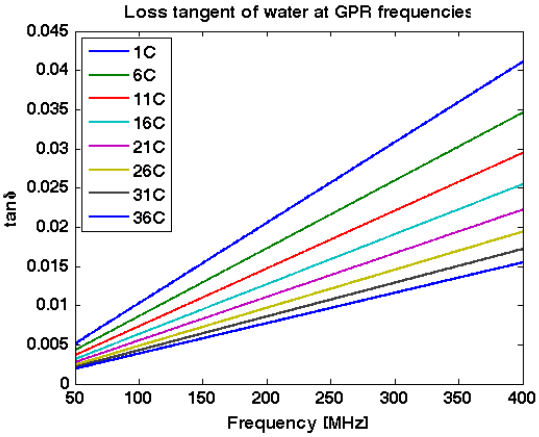

(d) loss tangent at GPR frequencies

Fig. 2.8 Water properties.

$$\epsilon(\omega) = \frac{\epsilon_s - \epsilon_2}{1 + j\omega\tau_1} + \frac{\epsilon_2 - \epsilon_\infty}{1 + j\omega\tau_2} + \epsilon_\infty$$

Dielectric relaxation parameters of water

T (K)	ε	τ_1 (ps)	ε_2	τ_2 (ps)	ε_∞	χ^2
273.35	87.57	17.67	6.69	0.9	3.92	0.131
278.15	85.89	14.92	6.76	1.0	4.10	0.094
283.15	83.93	12.70	6.57	0.9	4.08	0.118
288.15	82.24	11.00	6.64	1.0	4.34	0.071
293.15	80.31	9.60	6.53	1.2	4.42	0.067
298.15	78.32	8.38	6.32	1.1	4.57	0.106
303.15	76.39	7.39	(5.75)	0.9	4.60	0.090
308.15	74.91	6.69	6.22	1.5	4.74	0.060

Table 2.12 Water properties from [13]

Water			
$\circ C$	**50 MHz**	**250 MHz**	**400 MHz**
Complex permittivity			
1	87.6 - j0.45	87.6 - j2.25	87.4 - j3.59
6	85.9 - j0.37	85.8 - j1.86	85.8 - j2.97
11	83.9 - j0.31	83.9 - j1.55	83.9 - j2.47
16	82.2 - j0.26	82.2 - j1.31	82.2 - j2.09
21	80.3 - j0.22	80.3 - j1.11	80.3 - j1.79
26	78.3 - j0.19	78.3 - j0.95	78.3 - j1.52
31	76.4 - j0.16	76.4 - j0.82	76.4 - j1.31
36	74.9 - j0.15	74.9 - j0.73	74.9 - j1.16
Loss tangent			
1	0.0051	0.0257	0.0411
6	0.0043	0.0216	0.0346
11	0.0037	0.0184	0.0295
16	0.0032	0.0159	0.0255
21	0.0028	0.0139	0.0222
26	0.0024	0.0121	0.0194
31	0.0022	0.0108	0.0172
36	0.0019	0.0097	0.0155
Impedance			
1	40.3 + j0.21	40.2 + j1.03	40.2 + j1.65
6	40.7 + j0.18	40.6 + j0.88	40.6 + j1.41
11	41.1 + j0.15	41.1 + j0.76	41.1 + j1.21
16	41.5 + l0.13	41.5 + j0.67	41.5 + j1.06
21	42.0 + j0.12	42.0 + j0.58	42.0 + j0.93
26	42.6 + j0.10	42.6 + j0.52	42.6 + j0.83
31	43.1 + j0.09	43.1 + j0.46	43.1 + j0.74
36	43.5 + j0.08	43.5 + j0.42	43.5 + j0.67

Table 2.13 values

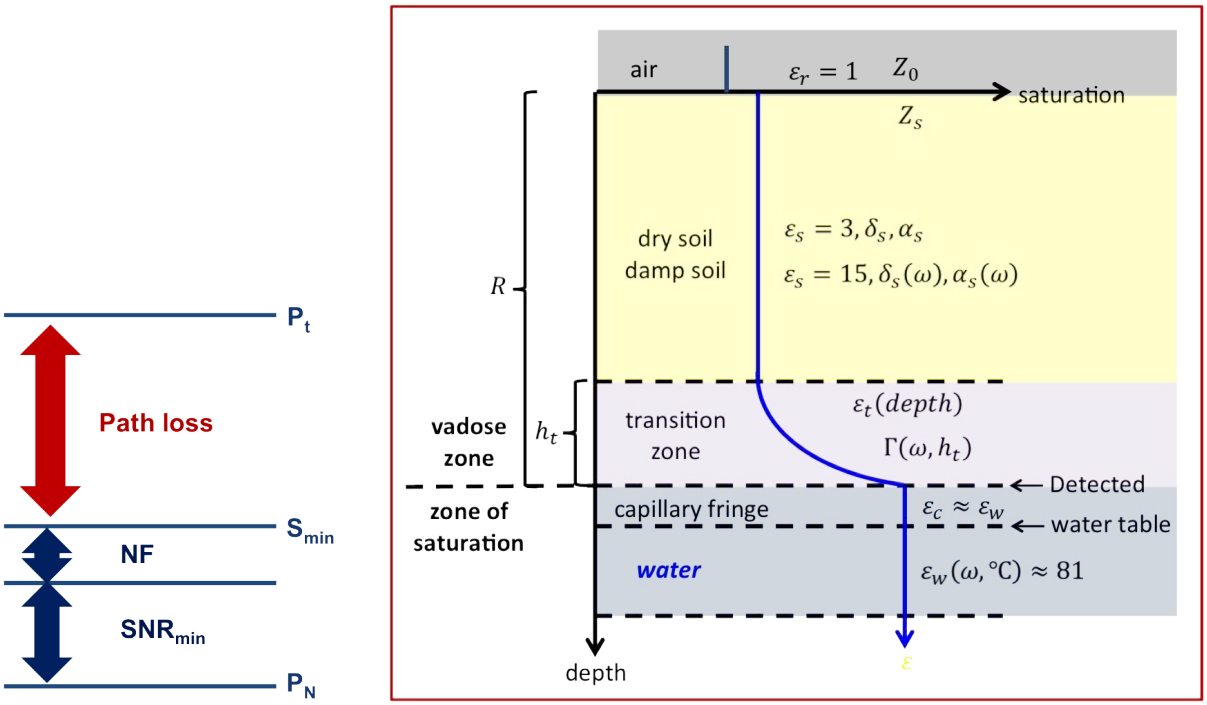

(a) path loss (b) ground model

Fig. 2.9 Power budget.

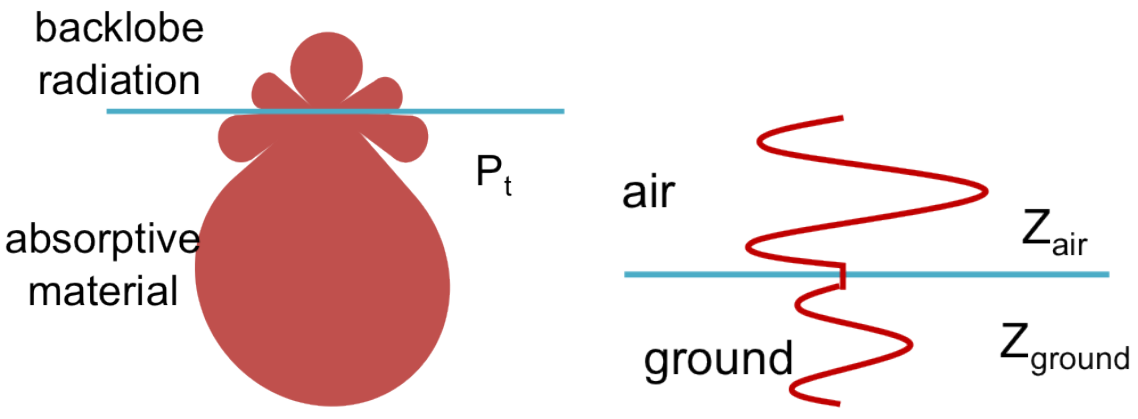

(a) absorption into material. (b) transmission loss.

Fig. 2.10 Power transmitted into the ground.

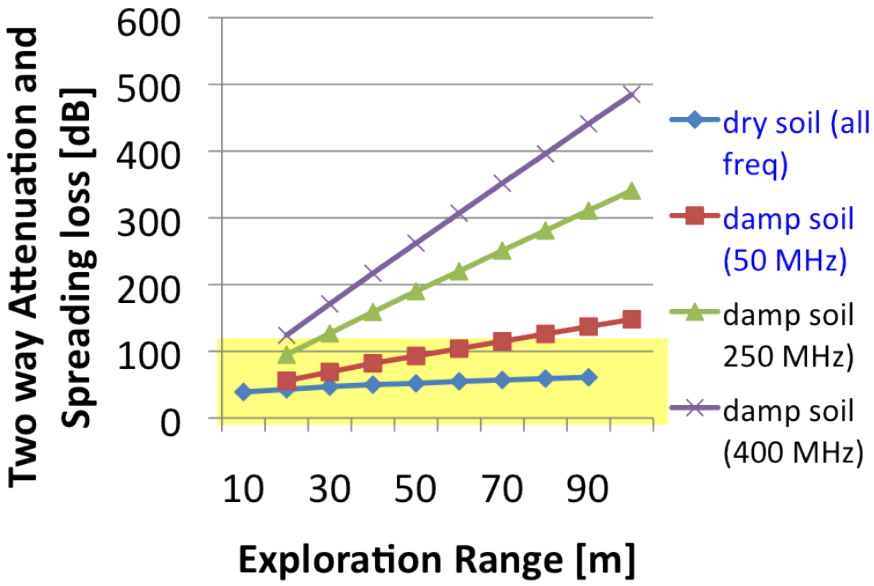

Fig. 2.11 Two way attenuation and spreading loss versus range.

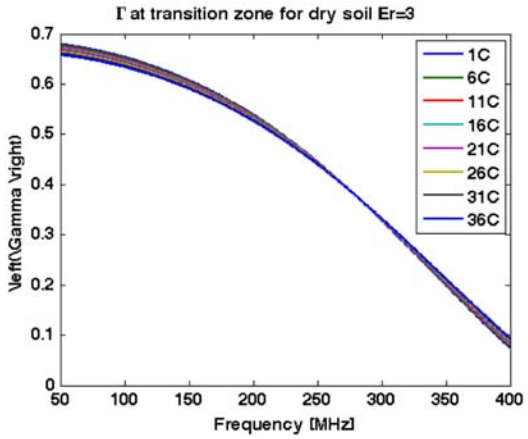

(a) dry soil ($\epsilon_r = 3$), thin transition (h = 0.1m)

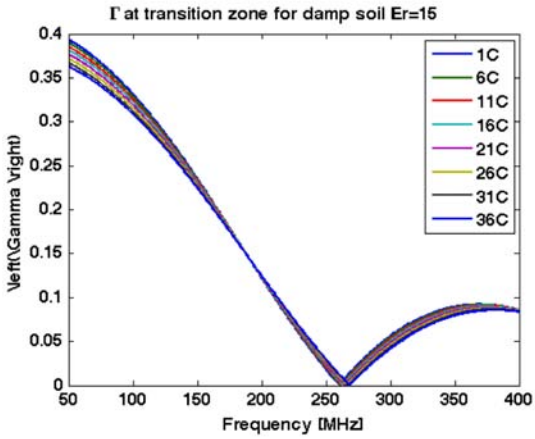

(b) wet soil ($\epsilon_r = 15$), thin transition (h = 0.1m)

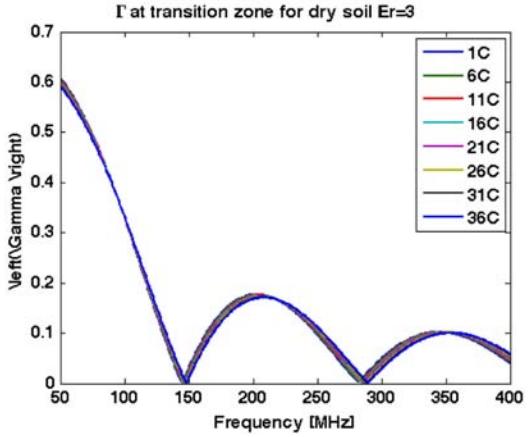

(c) dry soil ($\epsilon_r = 3$), thick transition (h = 0.3m)

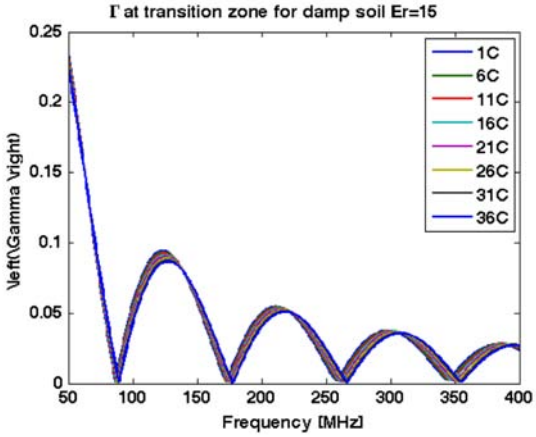

(d) wet soil ($\epsilon_r = 15$), thick transition (h = 0.3m)

Fig. 2.12 Water properties.

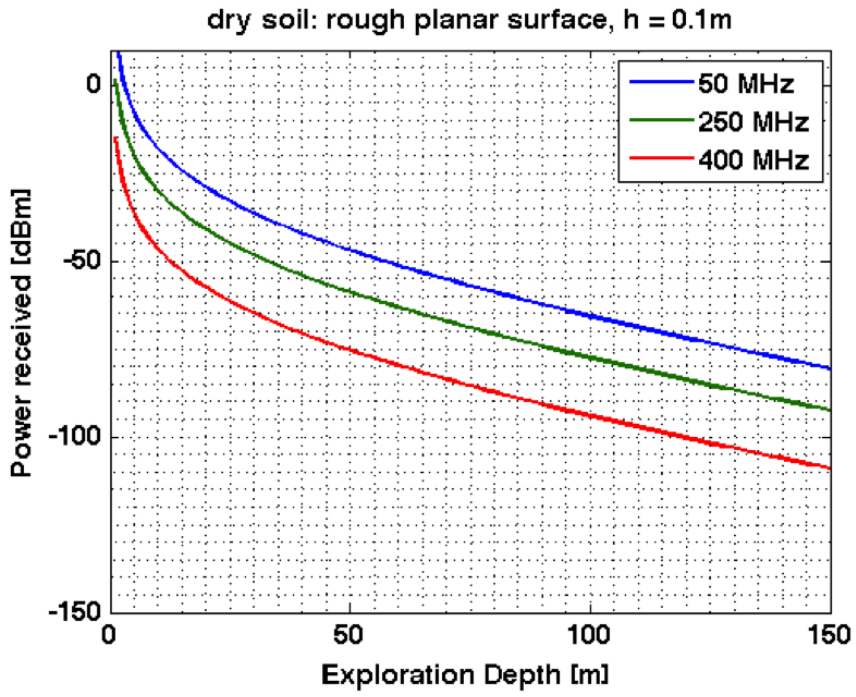

(a) Power received versus target range, dry soil, h = 0.1

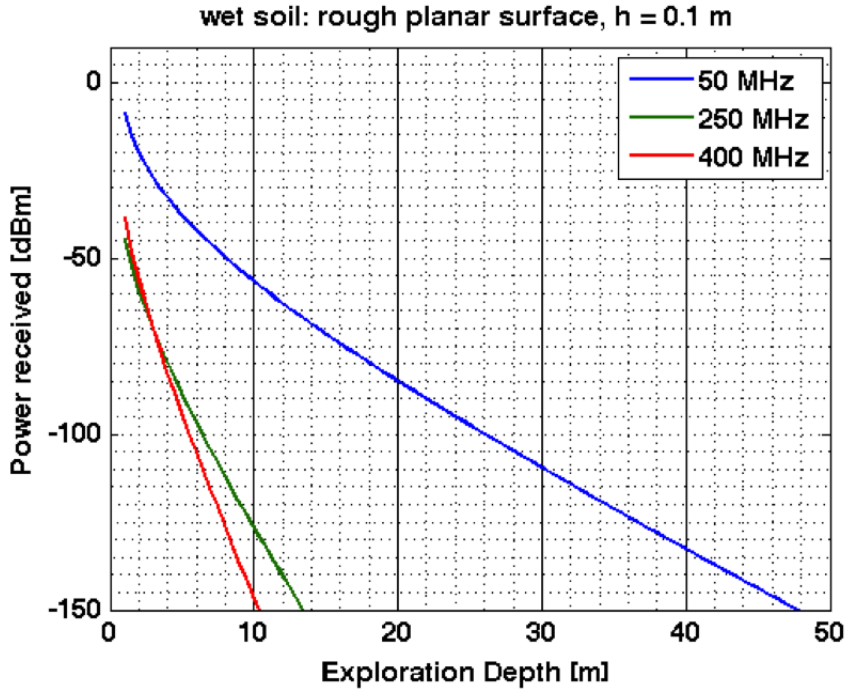

(b) Power received versus target range, wet soil, h = 0.1

Fig. 2.13 Power received versus range.

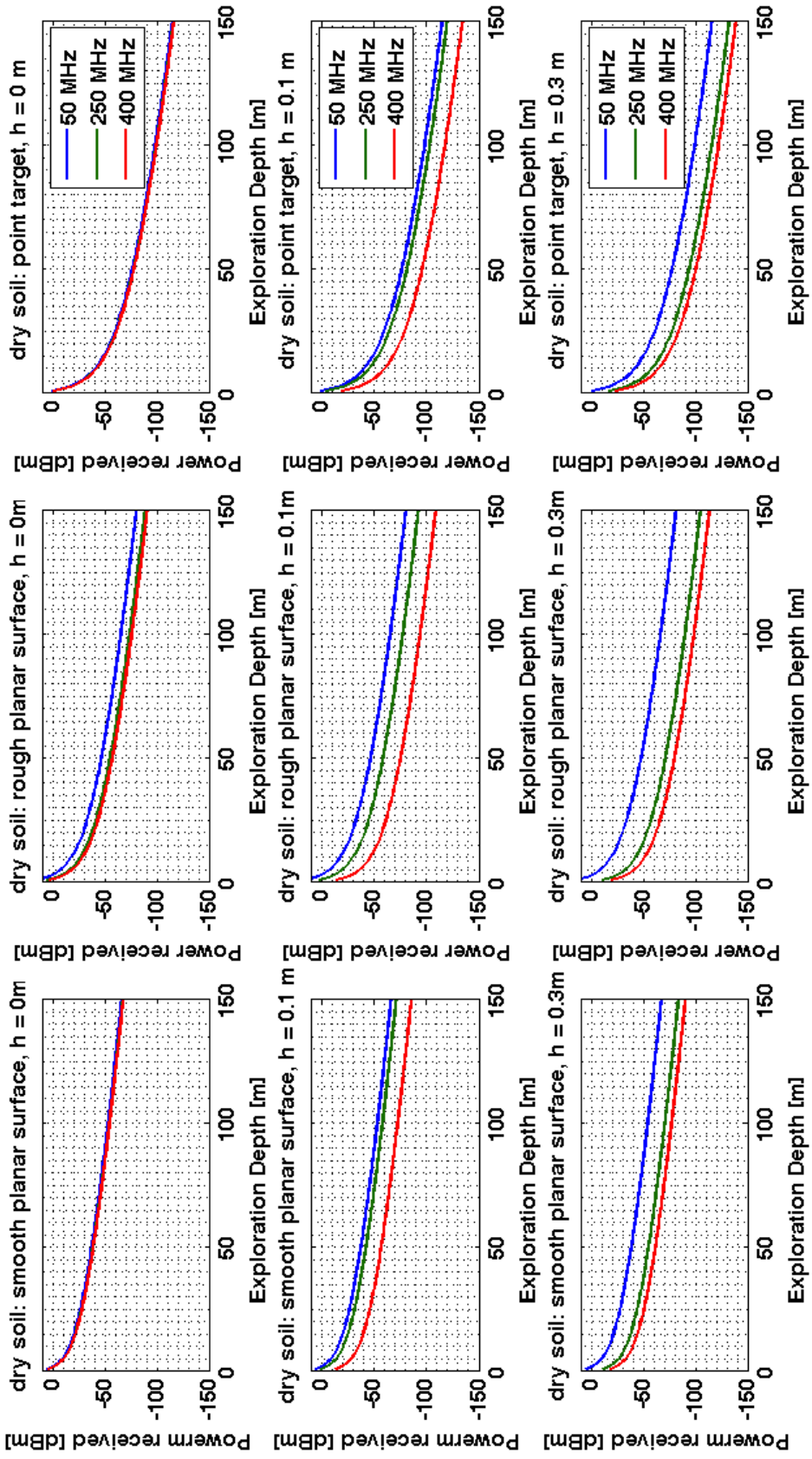

Fig. 2.14 Power received versus range for various frequencies and target conditions (dry soil).

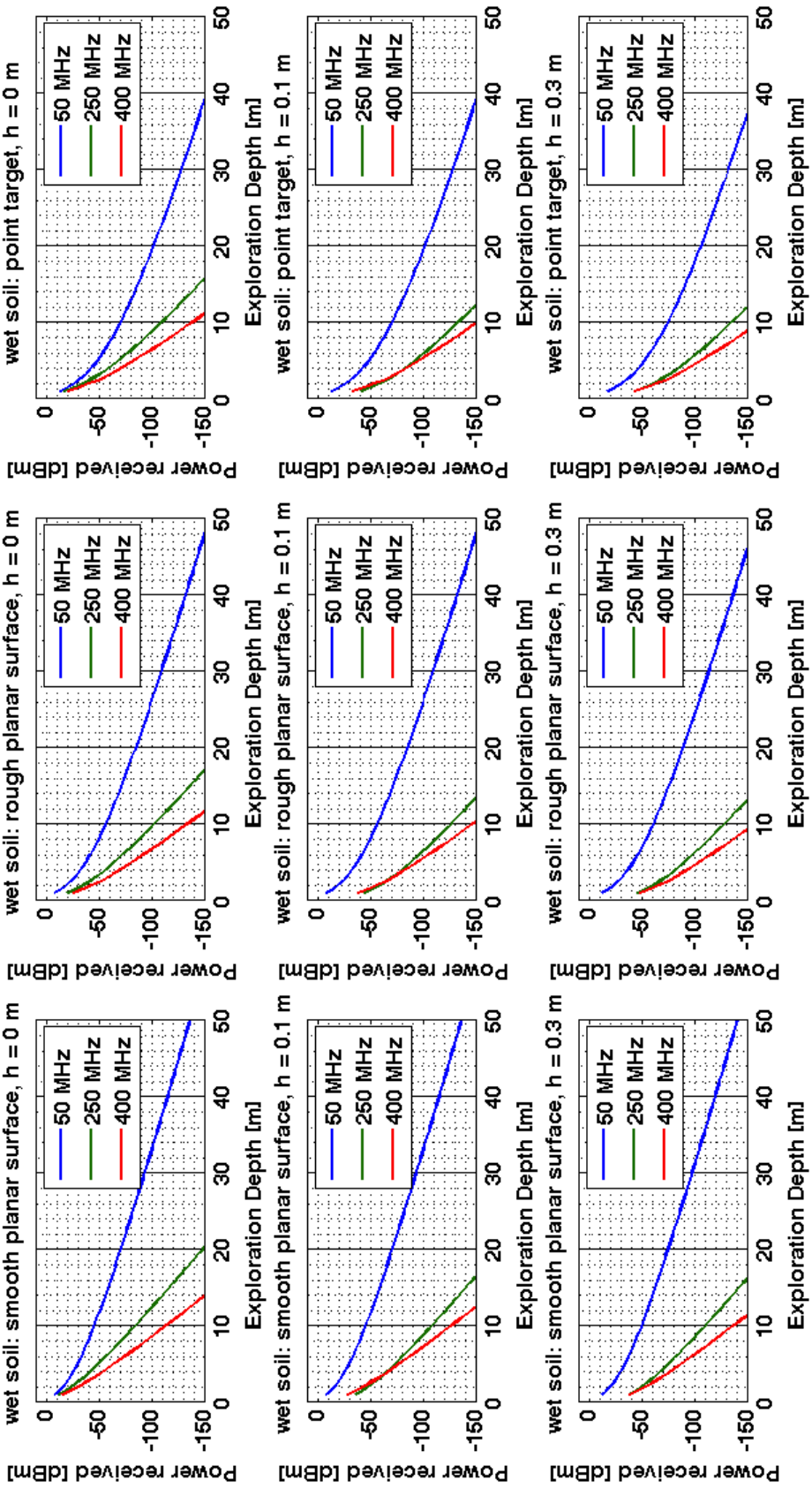

Fig. 2.15 Power received versus range for various frequencies and target conditions (wet soil).

2.6 Receiver Design

The receiver (Figure 2.16) was designed to have a sensitivity P_{min} = -123 dBm as seen in (2.6.1). This is based on a noise power P_N = -101 dBm, defined by the receiver bandwidth B_{IF} = 20 MHz for the highest expected beat frequency, the receiver noise factor NF ≈ 2 dB (taking into account the noise factor of the Analog to Digital Converter due to thermal or quantization noise) and finally the minimum required signal-to-noise ratio at the receiver output (based on the size of the FFT matrix, corresponding to the number of SFCW frequency steps used) SNR_{min} = -24dB.

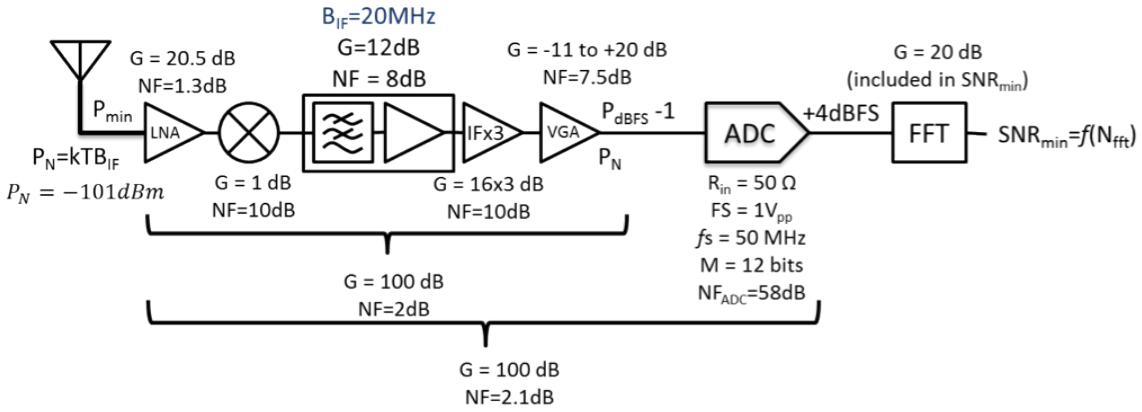

Fig. 2.16 Receiver design.

$$P_{min} = P_N + NF + SNR_{min} = -101dBm + -24dB = -123dBm \tag{2.6.1}$$

Addiing additional amplification stages for the outdoor setup will allow an overall gain of 100dB, providing $P_{out} - 101dBm + 100dB = -1dBm$ of power to the ADC output, a level that is suitable considering a full scale level of +4dBFS.

2.7 Analog to Digital Conversion

The ADC Noise Figure is estimated using [105] and [58] which specifies the effective ADC Noise Figure as a function of quantization noise and thermal noise. The expression takes in the Full Scale Power level in dBFS. For the HMC9000 Analog Digital Converter which features a FullScale input level = $1V_{pp}$, input terminating resistance

= 50 Ω, 12 bit resolution, SNR = 40dB and sampling frequency set to 50 MHz and full scale level of $P = \frac{V_{RMS}^2}{R_{in}} = \frac{\left(\frac{Vpp/2}{\sqrt{2}}\right)^2}{R_{in}} = 4dBFS$. When used in

$$NF_{ADC} = \underbrace{(P_{dBFS} - 1) - SNR_{ADC}}_{\text{Integrated Nyquist band noise power}} - \underbrace{10log_{10}(f_s/2)}_{\text{(normalization)}} - \underbrace{10log_{10}(kTB)}_{\text{thermal noise}} \tag{2.7.1}$$

Which gives $NF_{ADC} = 4dBFS - 1dBFS - 45dB - 74dBHz + 173dBm/Hz = 50dB$

2.8 Signal Processing

The minimum required SNR at the receiver output is chosen based on the number of FFT points (the number of SCFW frequency steps) as seen in Figure 2.17. The signal processing is performed using the EasySuite software to computer the IFFT and interpret the frequency spectrum. It also allows for the selection of the ADC output bandwidth or number of samples per second.

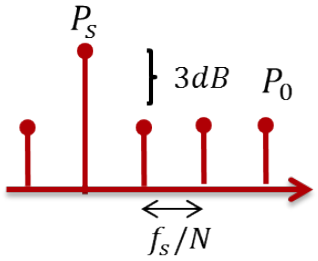

Fig. 2.17 Signal to noise ratio.

2.9 Detection

The minimum required SNR depends on the desired probability of detection and false alarm. The probability of false alarm varies from application to application. Detection can done using hypothesis testing, which involves deciding which hypothesis is true. Some examples of well known detection criteria are Bayes or Neyman-Pearson detection criteria. The process is explained below however many details are omitted. For the hypothesis test

$$H_0 : \theta = \theta_0, \text{ noise (null hypothesis)}$$
$$H_1 : \theta = \theta_1, \text{ target + noise}$$

Detection is done by forming a decision rule $\phi(x)$

$$\phi(x) = \begin{cases} 1 & \text{decide } H_1 \\ 0 & \text{decide } H_2 \end{cases}$$

We then define the parametric measurement model $p(x|\theta)$. The detection process will have probability of false alarm P_{fa} and probability of detection P_d

$$P_{FA} = \int_{\phi(x) \text{ decides } H_1} p(x|0)\, \mathrm{d}x$$
$$P_D = \int_{\phi(x) \text{ decides } H_0} p(x|0)\, \mathrm{d}x$$

The decision between H_1 and H_2 can be made using the likelihood ratio test. The likelihood ratio Λ is defined as

$$\Lambda(x) = \frac{p(x|\theta_1)}{p(x|\theta_0)}$$

where $p(x|\theta_0) =$ probability that H_0 is true and $p(x|\theta_1) =$ probability that H_1 is true. The detection/decision process can then consist of the following: if $\Lambda \geq \tau$ then a detection is made.

$$P_{FA} = P[\Lambda(x) \geq \tau | H_0]$$
$$P_D = P[\Lambda(x) \geq \tau | H_1]$$

The detection threshold η needs to be defined for a specified P_{fa} which varies for different applications. A classical way to determine the optimal threshold for a specified P_{fa} is to find η that satisfies

$$\int_{x:\Lambda(x)>\eta} p\left(x;\theta_0\right) \mathrm{d}x = P_{fa}$$

The search for groundwater should be performed using a series of detections (Figure 2.18). The first detection can consist of a search across a wide area, measuring the spectrum and power level to determine weather or not subsurface anomalies exist. If no detection is made (Figure 2.18a) the search continues. If a detection is made (Figure 2.18b) the the radar operation mode can be switched to be able to discriminate weather or not the subsurface anomaly found is of any significance (Figure 2.18c) and resembles a quantity of groundwater (Figure 2.18d). The SFCW radar steps through each frequency slowly, therefore each frequency will have different penetrationa and reflection properties that can be analyzed in order to obtain more information about the subsurface object. A detailed image of the subsurface can be extracted using the appropriate software.

2.10 System specifications

The transmit waveform used will dépend on the operating mode. For the configuration shown in Table 2.18 and Figure 2.19, the system steps through 512 frequencies ranging from 50MHz to 400 MHz over a bandwidth of 350 MHz. The duration of the chirp is 12ns, spending 0.0237μs at each frequency. A T_m/τ ratio of 30 is used to maintained adequate resolution. A 20dBm transmit power will be used which exceeds the power emissions limits which do not apply when performing controlled measurement in remote environments. The receiver has a sensitivity of -123 dBm, a bandwidth of 20MHz, noise figure 2dB and overall gain of 100dB. The analog to digital converter sampling frequency will be set to 50 MHz, This will give a maximum unambiguous range of over 60 meters and resolution of less than 25 centimeters. The IF bandwidth of 20 MHz was required in order for the software to recognize the spectrum. The noise however is still low enough to have an adequate detection range and it is ensured that $f_{min} \geq f_{b_{max}}$.

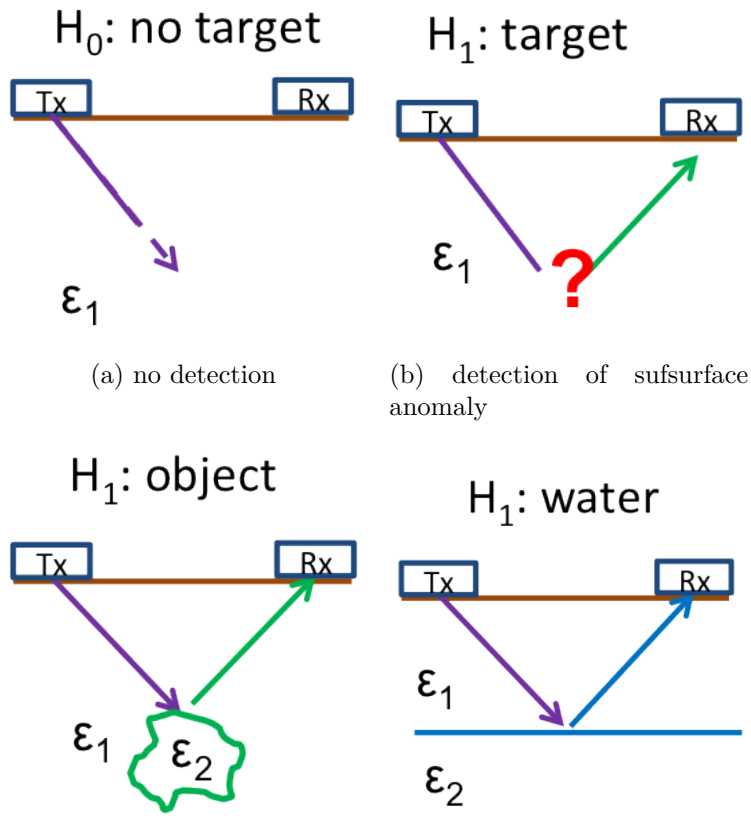

(a) no detection

(b) detection of sufsurface anomaly

(c) detection of nonwater object

(d) detection of groundwater

Fig. 2.18 Detection.

2.11 Conclusion

The system specifications for a SFCW/SFMCW GPR (stepped frequency modulated continuous wave ground penetrating radar) system designed specifically and exclusively for groundwater detection at large depths have been established. These specifications provided a theoretical foundation to which the flexible monolithic ultra-portable ground penetrating radar using inkjet printing technology (Figure 2.20) can be built upon. Based on these system specifications and hardware availability, the flexible system will be designed transmit a frequency sweep from 200-400 MHz and the receiver will be designed to have a 20MHz bandwidth.

System Specifications	
Transmit Waveform	
Modulation type	Step,Δ
Minimum frequency	50 MHz
Maximum frequency	400 MHz
Sweep bandwidth	350 MHz
Number of frequency points	512
Dwell time (at each freq)	0.0237μs
Modulation period	12.12μs
Modulation frequency	80 kHz
Sweep period to TWT	30
Power	
Transmit power	20dBm
Antenna gain	6dB
Signal Propagation/Path Loss	
Attenuation/Skin depth	α, δ_s
Target RCS	σ
Target reflection	Γ
Receiver Design	
Receiver noise figure	2 dB
Conversion gain	100 dB
Thermal noise	-101 dBm
Receiver sensitivity	-123 dBm
Receiver bandwidth	20 MHz
Maximum beat frequency	15 MHz
Beat frequency period	0.0857μs
Sampling, Signal Processing	
ADC sampling frequency	40 MHz
FFT length	12.12 ns
FFT gain, 10log(...)	24 dB
FFT resolution	80 kHz
Performance	
Unambiguous range	63 m
Detection range	$>$ 30 m
Range resolution	$<$ 25 cm
Signal to Noise Ratio	-24 dB

Table 2.18 System specifications.

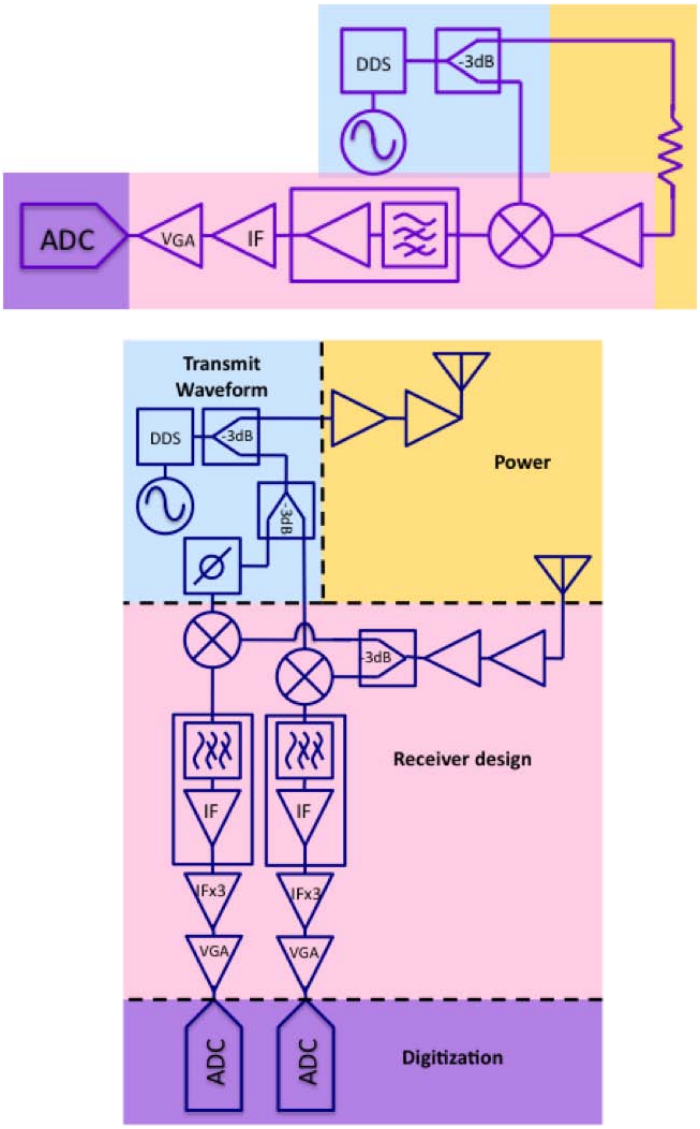

Fig. 2.19 Schematic (indoor, outdoor setup)

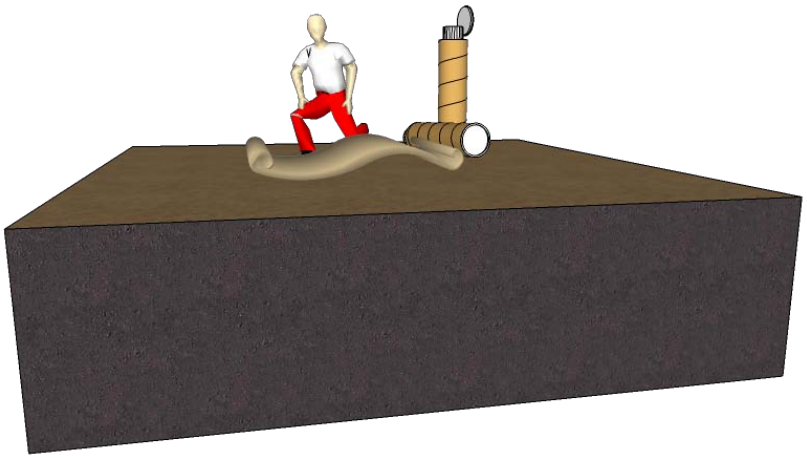

Fig. 2.20 Portable radar.

Chapter 3

Design and Fabrication of Monolithic GPR

3.1 Introduction

Ground penetrating radar systems used in outdoor environmental research, as opposed to wall probing radars, often require frequencies in the VHF range or lower in order to reduce the attenuation undergone in conductive soil ($\epsilon_r \approx 3-15, \sigma \approx 0.001-0.01 S/m$) and maximize exploration depth to reach large scale deeply buried land formations. The antennas associated with environmental GPR systems are large which is why many systems are equipped with wheels and detachable antennas to enhance transportation and storage. Ground Penetrating Radar systems that synthesize a 2D or 3D image of the subsurface require measurement surveys that involve positioning these antennas in various spatial orientations with respect to one another and/or moving the antennas along incremental spatial positions of the ground surface. Transporting the system to, and performing measurements in certain environments is challenging when there is limited vehicle access. Limited portability can complicate geophysical studies when it is necessary to transport the entire system by foot to perform measurements. Inaccessible locations may require climbing up and down steep landforms, maneuvering and squeezing through awkward spaces, scrambling over rocky obstacles and in some cases swimming. In addition to portability, speed can become an issue in emergency work in which one may need to rapidly transport the system through unmarked outdoor places. Rapid system deployment is also critical even in geophysical studies performed in extreme outdoor conditions where exposure time is costly when enduring freezing temperatures or extreme heat. Performing GPR surveys in

conditions with extreme temperatures, limited facilities and limited vehicle access may require additional staff for the transportation, setup and measurements. The extreme conditions also limit the time available for system setup and measurements and can reduce the quality and scientific gain of the GPR study.

One way to enhance the portability of a GPR system would be to change the packaging of the entire system to one that provides further consolidation, mechanical versatility, and miniaturization. In this work, the concept of an ultra portable GPR system is proposed with the goal of realizing an entire GPR system and antenna on a common rollable substrate that can easily be stored and attacked for backpack transportation and quickly unpacked and setup while maintaining good performance lifetime. The system would be referred to as monolithic, as the actives, passives and antenna would share a common substrate that is rollable around a radius small enough for efficient storage and transportation. The concept of a portable monolithic ground penetrating radar is illustrated in Figure 3.1. The portable monolithic radar would be extremely rollable for storage in a light form cylindrical-like container that can be attached to the body or a backpack, and carried while walking. It could be stored anywhere indoor our outdoors, as easily as if it were just an umbrella. The user could repeatedly pack and unpack the system and even take it along with them during food, drink and toilet breaks, as it appears less imposing in a poster container.

3.1.1 Background: Materials

The materials used in electronics have changed significantly from what they were nearly a century ago, and very drastically over the recent decades. The PCB, fabricated using various types of multi-step additive and subtractive processes became the foundation of all electronic components. The introduction of ceramics such as LTCC for multilayer passive elements, monolithic ICs and hybrid ICs reduced cost of and increased miniaturization of modules. Organic materials such as LCP demonstrated robust properties including high mechanical strength, chemical inertness, and abundant availability as well good electrical properties (high ϵ_r, low $\tan\delta$). LCP was widely available, as it is used in many everyday materials, and the properties made it popular for MEMS and also flexible/fold-able antennas as seen in Figure 1.14 (p 22) of Chapter 1.

Finally substrates such as paper, PET and other fabrics were introduced as low cost, flexible materials that could be patterned by using inkjet printing; a low cost, environmentally friendly additive method to realize interconnects, and eventually multi-

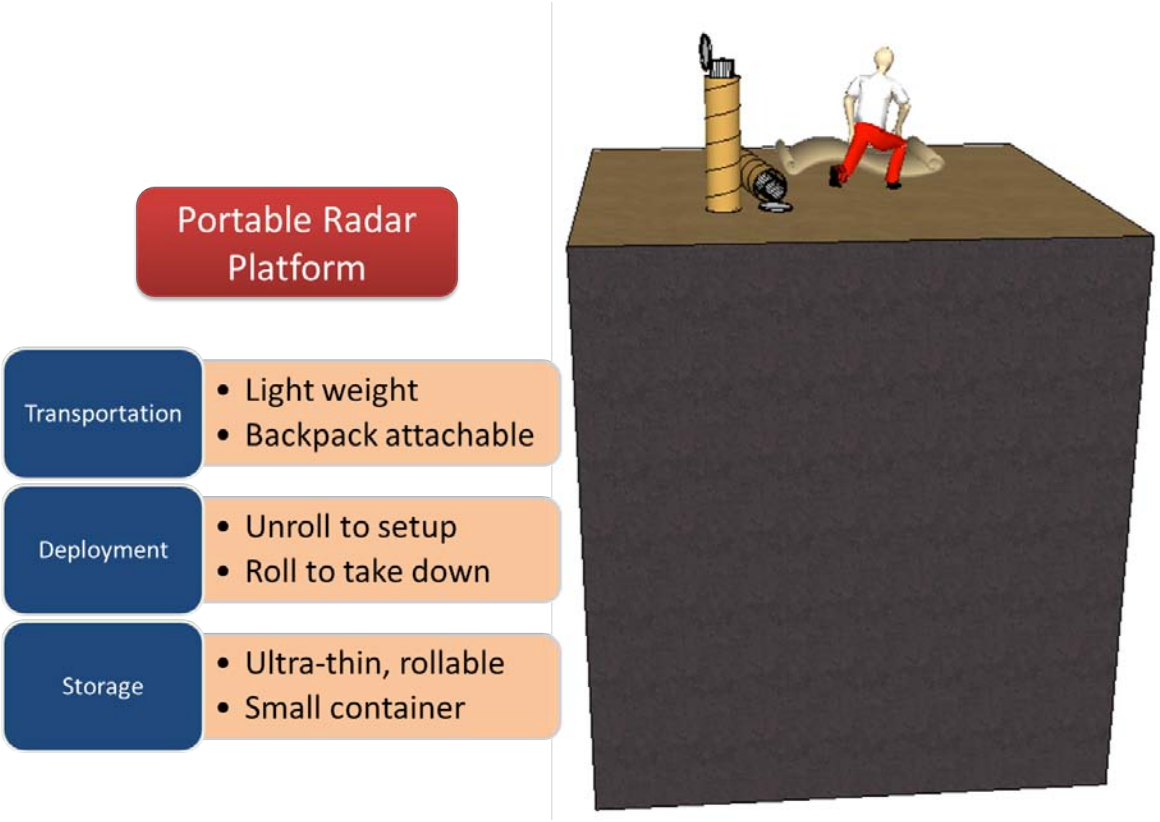

Fig. 3.1 concept of portable Radar.

material, multi-layer modules in the near future.

3.1.2 Integration Level of Flexible Electronics

The integration level of flexible electronics has taken a similar route to that of conventional electronics. The first flexible electronic consisted only of transmission lines. It was through these simple structures that electrical properties of flexible substrates and print solutions were accessed, and the complex process of configuring and optimizing the printing method became a topic of research. Transmission lines were printed on flexible substrates to benchmark the control of impedance in inkjet printed microstrip and CPW lines. Printing resolution limits became a primary focus in order to improve the quality of narrow line widths and gaps. This involved extensive characterization optimal printer settings, sintering, curing and proper handling of substrates and printing solutions. Materials printers are equipped with user friendly software which allows the importing of more complex geometries such as *small antennas*. In addition, *passive elements (R,L,C)* can be mounted onto the inkjet printed intercon-

nects using low temperature solder paste. This has lead to the development of the first complete modules on paper. As inkjet printing technology is rapidly advancing at this very moment, the ability to print *2D/3D interconnects* will allow the realization of multilayer inkjet printed modules. The 2D/3D interconnect printing capabilities will help further expand the integration of flexible electronics to *homogeneous 3D modules*. As materials expertise increases, *multi-material multilayer modules* such as printed capacitors, graphene transistors will allow for the realization of a complete flexible, rollable system.

3.1.3 Technology and Applications

The motivation for optimizing inkjet printing technology is driven not only for the purpose of enhancing current consumer products but also to support various disruptive technologies that have become major topics of research. Low-cost fabrication of multi-material structures can facilitate the realization of various multi-discliplinary concepts that are difficult to fabricate, and thus speed their advancement. In addition to flexible interconnects, inkjet printing technology has given researchers the ability to explore and exploit nanostructures (CNT, graphene) inexpensively. This is leading the development new devices that benefit from the electrical, chemical and mechanical properties of nanostructures. Microfluidics technology, previously facing many technology and cost challenges, has also advanced significantly due to inkjet printing technology and can be more easily exploited for passive sensors or smart skin applications.

Wireless sensor networks have rapidly become an integral part of everyday life. Applications (Figure 3.2 p 71) such as monitoring suspension structures for structural integrity as they undergo immense mechanical force from natural disasters. Other applications include gas detection, such as detecting noxious gases in underground mines or ensuring that the food sold off the supermarket shelf remains fresh and is continuously kept at the correct temperature and humidity level. Sensor networks are facilitating the ability to compile massive amounts of data which can greatly improve the knowledge of the surrounding environment. To enable scalable pervasive sensor networks which collect this data, the sensing platform should be reliable, energy efficient, and extremely low cost to become a viable long-term solution. Inkjet printing as an electronics fabrication technology has attracted significant attention over the last decade as a method to fabricate passive and active components. Printing of electronics allows for rapid prototyping, low material waste, and does not require

clean room environments. Conventional methods of fabricating multi-layer passive structures such as metal-insulator-metal (MIM) capacitors, requires a sequence of photo-lithography and etching steps which use dangerous chemicals and waste vasts amounts of material in the subtractive processing. Inkjet printing, however, is a true additive and non-impact technology. This means it will deposit only the intended material, and then successively deposit multiple layers of different materials without disturbing or contaminating the previously deposited layers. This makes the process very attractive for the multi-layer printing of RF components, and especially for the first realistic realization of rollable/flexible sensor and radar systems.

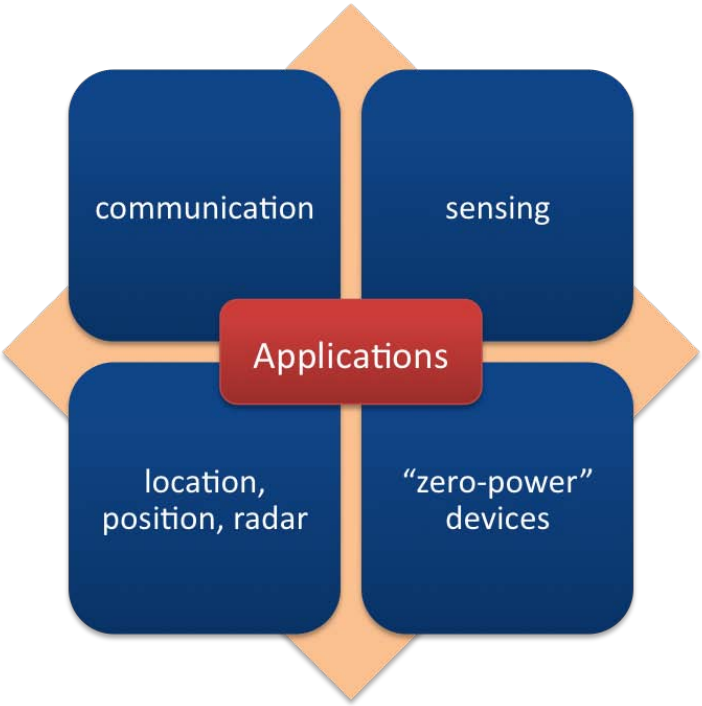

Fig. 3.2 Key applications for discruptive technology.

The focus of this research is to realize a portable, monolithic, ground penetrating radar system using a hybrid inkjet-printing/rigid component approach. Implementing such a system will requires new materials, technology and assembly techniques. Inkjet printing technology offers a cost effective, versatile and efficient method for realizing new flexible or rollable devices. The focus of this research is therefore to develop a portable, monolithic, ground penetrating radar system using this hybrid inkjet-printing/rigid component approach. To do this, a basic radar module is designed, fabricated, assembled and the structural integrity and rollable performance is experimentally validated. The first performance level is achieved when the material

properties and impedance for the chosen technology are verified, demonstrating a *proof of concept operation*. This level allows the establishment of a set of basic design rules to reach the next level of performance which is *fundamental performance operation*. This level represents the ability to integrate commercial off the shelf components with the new technology and demonstration of a good architecture choice. This performance level can be quantified by the devices ability to perform basic functions using a repeatable assembly procedure optimized for this new technology. The *advanced performance operation* will test the dynamic performance of the system and the bendability or rollability. In addition, a fundamental requirement for a state of the art system is high performance including low insertion loss over a wide bandwidth. To reach each stage of performance (Figure 3.3) various challenges encountered in the design and technology process must be solved.

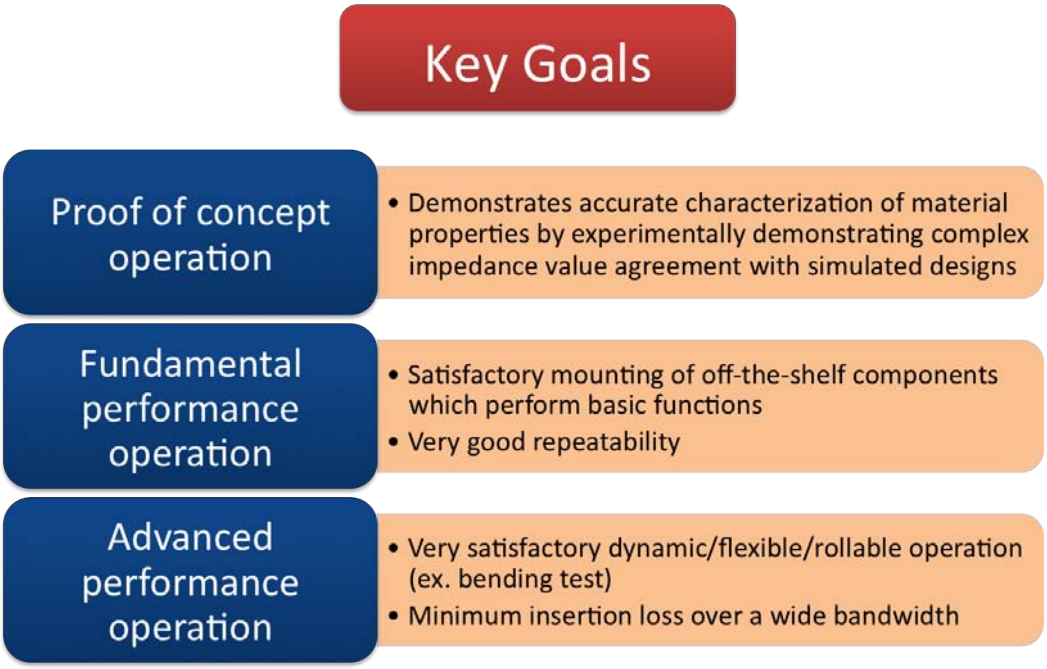

Fig. 3.3 Focus of this research.

3.2 Design

An FMCW architecture was chosen for the flexible GPR system. The FMCW radar transmits a frequency sweep or "chirp" then receives a time-delayed echo reflected from the target. The transmitted LO and received RF are correlated and produce an IF beat

frequency that is proportional to the target distance, and that can be interpreted by the IFFT. The system uses a typical transceiver architecture consisting of a VCO/PLL based frequency sweep generator, LO and power amplification and finally a low-noise receiver to down-convert and provide the necessary gain and filtering for low speed analog to digital conversion. The GPR imaging requirements increases the complexity of the FMCW architectures due to the need to generate an extremely pure and highly linear frequency sweep over a wide bandwidth in order to perform accurate, reliable and high resolution imaging. It is because of this that developing a state of the art GPR system often consists of integrating a large quantity of commercial off the shelf components together and using PCB. FMCW/SFCW radars are not commercially available and are typically used in academic research. In order to verify the ability to realize a large system using the hybrid approach, the flexible system was designed to perform the most fundamental FMCW functions while the electrical and mechanical behavior could be observed to benchmark the performance level. The elements chosen were the VCO, coupler, low noise amplifier, mixer and associated matching and biasing circuits with varying sizes ranging from 130mm to 3mm, with different material finishes and different pin orientations. To maximize rollability, a single-layer, low-density, wide area layout was chosen that was convenient for GPR VHF frequencies. The footprint layout was constructed in CADEagle using design rules based on the capabilities of the inkjet printing process. These rules included restricting the layout to one layer by minimizing crossovers and maintaining a resolution of at least 0.5mm between lines and pins. A LO frequency sweep between 200 and 400 MHz was chosen based on component availability and the ability of these frequencies to achieve significant exploration depth in earth oil. These specifications were validated theoretically and experimentally using a classical radar setup. The first component realized was the mixer circuit. For this component, the typical 4 layer board was reduced to 2 layers as seen in Figure 3.4

The design consists of an active mixer with 3 ports (LO, RF, IF), each port consisting of a single ended unbalanced 50 Ω input that is externally matched to the complex balanced impedance of the differential input ports using the classical broadband balun and matching network that can tuned for the mixer operating frequencies which extended up to 4 GHz. There are many commercial CAD tools that are very compatible with single layer designs intended for inkjet printing. CADEagle is one user friendly software that is simple and relatively versatile. Using this, one can specify the component footprints by drawing, symbolizing, pin-numbering, validating and naming each

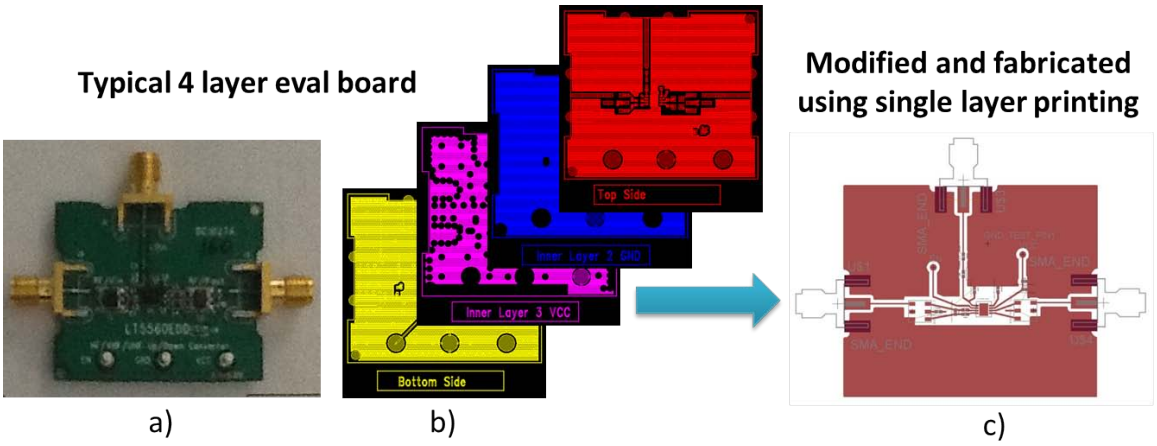

Fig. 3.4 Commercial mixer (LT5560) reduced to single layer.

element as is done with classical boards. Next, the signal lines can be drawn and connected using widths and geometries that adheres to the printing limitations. Due to restrictions in printing area the antenna size is limited so the frequency must increase which will only involve changing the passive elements while keeping the same footprint. After design verification, the file can be exported to a format accepted by the printing software. Since the software is intended for PCB designs, the user will receive various prompts concerning issues that may be irrelevant to the design. In the case of CADEagle, these prompts can be ignored without disturbing the file exportation. The final design exported will consist of multiple files of which only the single fingerprint is needed and can be converted to the inkjet printer file format. Additional exported files can used for assembly guidelines if necessary. In the first design the crossovers were left open and left to be realized directly in the fabrication.

3.3 Fabrication

There are a few choice of printing technologies that can be used to realize the circuit. One is the sheet-based inkjet printing of a silver nanoparticle conductive ink using a materials printer (Figure 3.5). The printer deposits 10 pico liter sized droplets using a pizeoelectrically controlled jetting device. The ability for the droplet to remain stable as it approaches the substrate requires expert observation and precise adjustment of the droplet speed. The optimal printer configurations will varies from material to material depending on the properties. Good printer settings and proper materials handling will ensure a clean contact for high resolution designs that can

achieve a resolution of about 21μm. The conductive ink consists of silver nanoparticles (nanospheres) dispersed in a solvent. Once the ink is printed, sintering is performed to remove this extra solvent. Between one and ten layers can be printed, and curing is performed between layers to solidify and improve the electrical conductivity of the printed layer. The curing is performed at 100 degrees celcius for one to ten hours in a temperature controlled oven. The curing must be performed quickly after printing because the printed ink will start to oxidize immediately upon exposure and degrade the electrical properties. Upon curing, a conductivity of σ=1.1e7S/m can be achieved. The advantages of this method is that one can achieve a very good conductivity and also print on a wide variety of materials and textiles. Photographic paper (ϵ_r=3-3.2, tanδ=0.02-0.05) is one examples of an easily accessible, widely available and environmentally friendly substrate that is often used with this type of printing process. It is available in reel-to-reel form and making this printing method in the near future, no longer restricted to sheet-based printing but also a perfect candidate for mass produced scalable applications. Figure 3.5 shows the first realization of the mixer circuit using this type of printing technology. This technology was used in the early stages of the design while optimizing the footprint geometry for the inkjet printing process. With this process the adhesion capabilities were tested as well as the contact quality of the assembled components.

Inkjet Printing: silver nanoparticle

Conductor : silvernanoparticle ink (σ =1.1e7S/m)

Substrate: ex. paper (ϵ_r=3-3.2 , tanδ=0.02-0.05, 10 mils)

Process
- pizeo-controlled jetting device
- 10pL droplets
- curing
- alignment

1-10 layers
Resolution: 21um

Tests
- Adhesion
- Trace/pad size
- Contact quality

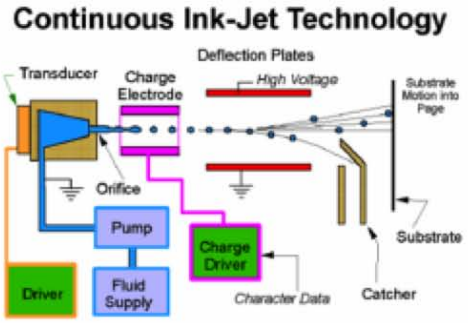

Challenges: nozzle clogging, droplet stability

Disadvantages to electroless copper deposition
- weaker adhesion
- sheet-based printing (currently)
- 10 to 20 times more expensive

Advantages over electroless copper deposition
- higher conductivity
- substrate versatility

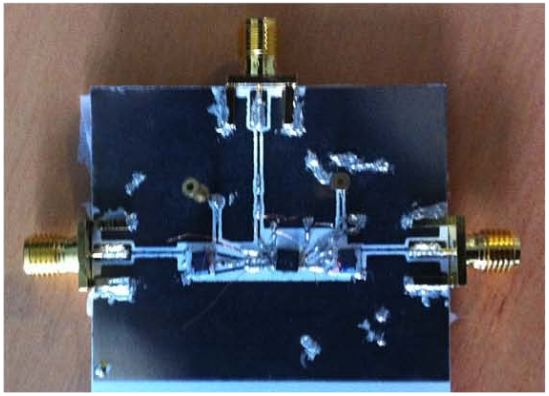

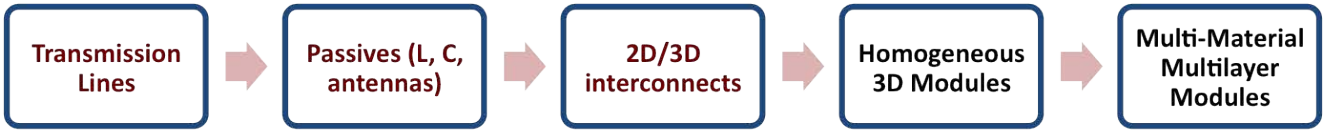

Fig. 3.5 Realization of circuit using silver nanoparticle technology process.

Another method that can be used to realize the flexible circuit is the catalyst-based electrodeless electroplating technology that combines inkjet printing technology into a two-step electroless plating bath process while allowing the mounting of SMD components using a low temperature paste. This method consists of two steps. The first step is the printing of a palladium-based catalyst ink onto a low-cost polymer substrate such as PET (ϵ_r=2.4, t=100μm) and then curing with UV light to improve bonding between the substrate and the catalyst. Next, the sample is placed in a copper bath where the copper film begins to deposit by means of a chemical reaction. The thickness of the film depends on the bathing time and the conductivity and thickness can be increased up to σ=3.2e6 S/m, t=0.61-3.8 μm. Furthur increase is difficult because the bathing time is limited by a volcano-like effect in which at a certain point in time, the line width starts to decrease with increasing thickness, thus no longer contributing effectively to the thickness or conductivity of the film. This method can be performed in house, but is also available commercially and was used to realize the first circuit as seen in Figure 3.7c. The availability of this method made it easier to focus more on the extremely large scale redesign aspect of this research.

Some advantages of using this method compared to using the sheet based inkjet printing of silver nanoparticle ink is that it is relatively fast and 20 times less expensive, making it ideal for wide-area printing. Another advantage found was that the copper film demonstrated very good adhesion the PET substrate, a good property to reduce the likelihood of component delamination when the circuit is rolled around a tight radius as rolling causses significant mechanical strain to the contacts. Drawbacks of this method compared to that of the silver nanoparticle inkjet printing are that the conductivity of the copper film is lower. Another drawback is that type of printing method is not compatible with textiles or fabrics because they cannot remain stable in the bath.

Inkjet Printing: Electroless copper deposition

Conductor : copper film (σ = 2e5-3e6 S/m, t = 4 μm)

Substrate: Polyethylene terephthalate (PET) – "polyester" (ε_r = 2.4, t = 100μm)

1. Print catalyst ink
2. Curing by UV exposure to improve bonding
3. Place in copper bath
4. Copper deposition (thickness ~ chemical reaction time), electroless growth

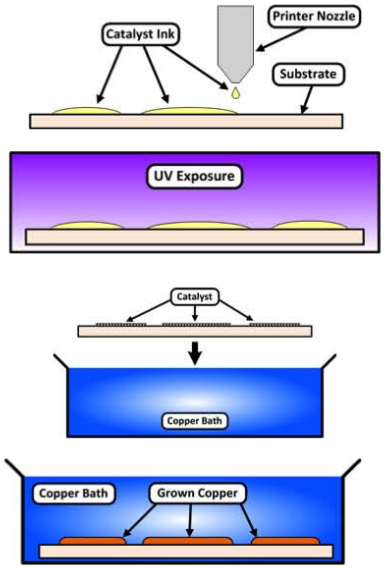

Advantages over silver nanoparticle inkjet printing

- stronger adhesion
- 10 to 20 times less expensive
- larger area printing

Disadvantages compared to silver nanoparticle inkjet printing

- lower conductivity
- process cannot be used on wide variety of materials

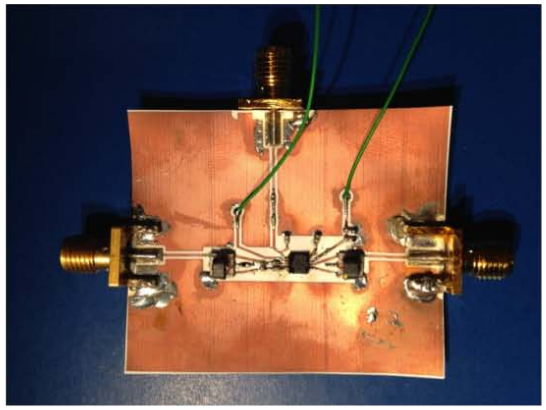

Transmission Lines → Passives (L, C, antennas) → 2D/3D interconnects → Homogeneous 3D Modules → Multi-Material Multilayer Modules

Fig. 3.6 Electroless copper deposition.

In the case of developing a rollable radar system using a hybrid commercial component/inkjet printing approach, both types of printing technologies demonstrated that they can realize conductive traces of complex layouts onto rollable substrates. Both technologies permit the attachment of surface mount components if a low temperature method is used. Both technologies allow the use of a protective coating (such as parylene) to enhancethe robustness by improving adhesion and to provide protection during flexing. The two-step electroless plating bath process was used more frequently in this research for the wide area realization capabilities which seem beneficial for debugging and redesigning the device, which as seen in the following chapters, was extensively done. The sheet-based silver nanoparticle inkjet printing method, however, will continue to be revisited in the near future because it demonstrates very good electrical properties as well as substrate versatility.

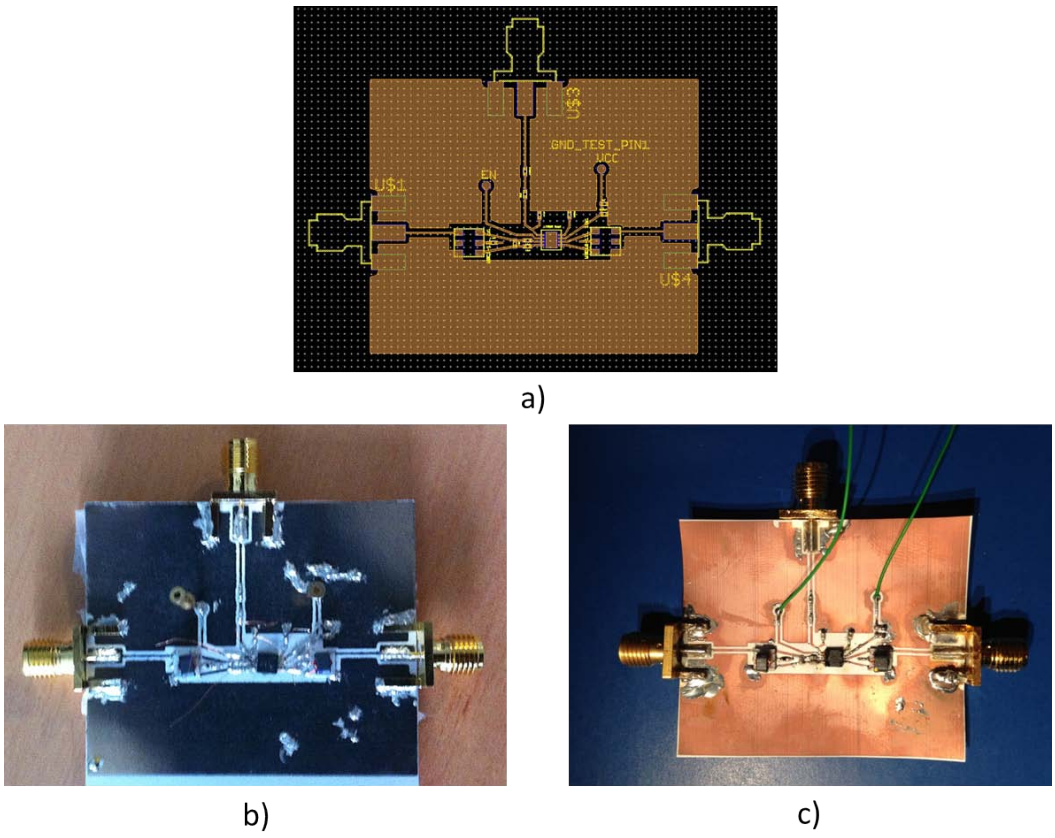

Fig. 3.7 Realization of a) using b) inkjet printing silver nanoparticle ink versus c) two-step electroless plating bath process.

3.4 Assembly

The method for bonding ICs to inkjet printed films on flexible substrate can be performed either manually or by using a preheated, temperature controlled oven. With both methods, the components are attached to the deposited copper film using a low-temperature solder paste that has a composition that is optimal for the bonded materials. More specifically, a solder paste with a melting temperature that is lower than the melting point of the polymers is required in order to avoid deformation or warping of the substrate or delamination of the copper layer. A paste that wets only the copper layer but not the PET will reduce the likelihood of assembly error. Lead-free is also preferred for environmentally friendliness

There are very few types of lead-free pastes that are appropriate for small components on flexible materials because the removal of lead increases the required processing temperature, making it incompatible with flexible materials such as paper or PET. Once choice is a tin-based paste Sn42Bi58 in which the low cost alloy, bismuth, is added to reduce the required reflow temperature. Bismuth, however; is also known to be brittle and to change in volume when cooled. This means that bending the circuit too much could risk abrupt delamination of the surface mounted element. Sn42Bi58Ag is another paste in which silver is added to increase thermal fatigue life, but the price silver is very expensive. Many commercial inkjet printing services have recommended $Bi_{58}Sn_{42}$. This is a lead free paste that has some of the best properties suitable with this technology and also demonstrates minimum dimensional change upon solidification. Interaction between paste and contact pad materials is also important. Certain contact pad materials may contaminate the paste and cause effects that reduce the contact quality.

Standard methods for attaching surface mount components to flexible PET have not fully entered the mainstram industry quite yet, therefore it is very important to experiment with the paste properties by performing a few tests to benchmark the interaction with the copper film and PET over temperature and time. The manual procedure is relatively simple, but only for small designs. It consists of collecting a small drop of paste using a sharp point and placing a small drop onto the contact locations. Using tweezers or any gripping device, the component is placed on the paste drop and held in place while carefully applying a soldering iron near the contact to fuse. As this method can yield quick realization of small experimental designs, it can become quite tedious with large designs, or fine resolution designs. Using

too little paste resulted in defective contacts that caused open circuits. Repairing these defects by means of reheating and adding more paste often lead to delamination of the component. Using too much paste increased the likelihood of bridging that caused short circuits. Repetitive bridge removal by means of reheating often lead to component delamination as well, and in many cases complete delamination of the printed copper layer making the entire circuit unusable (broken printed films were difficult if not impossible to repair). This was particularly an issue with the smallest IC having a pin pitch of 0.5mm as seen in Figure 3.8a-c. Cleaning bridges between such small pins required stabilizing the component and using very fine precision and minimum reheating. This was the smallest resolution limit that could be reached for mounting components onto flexible printed traces using both the manual placement method or the heated oven (which will be discussed later). During assembly it was best to avoid reheating all together, especially with flexible substrates as the reheating resulted in permanent warping of the PET and/or the printed conductor. Using the manual method, several circuits needed to be realized. Throughout the process it was very difficult to protect small ICs from the prolonged heat exposure of bridge repair so extra ICs were kept as replacements when they became damaged. This is why the large area printing became an important feature, as it allowed the fabrication of several footprint copies in case of failure or just simply the need for experimentation and disposal.

Avoiding copper film delamination became a top priority, which is why the adhesion properties of the printing technology are important, especially before a protective coating is applied, the period when the device is the most vulnerable. Sometimes it was best to start with the smallest most challenging IC first, so that if the board needed disposing due to delamination, time and resources have not been wasted having already mounting other components prior. The best technique used to manually mount small unexposed pins was to apply a moderate amount of paste to the pins to make them exposed, then place the component in the contact position and wave the iron along the exposed paste in an 'outwards' direction (away from the IC) as if painting a line. This technique, if done properly, often resulted in successful mounting as seen in Figure 3.8d. To prevent such complications due to bridging and costly reassembly, the packages with orthogonal pins such as the one in Figure 3.8d can be selected, when available. Throughout the entire process, careful handling of the substrate during excessive manipulation was necessary.

Three different bonding methods and materials were used to handle the differ-

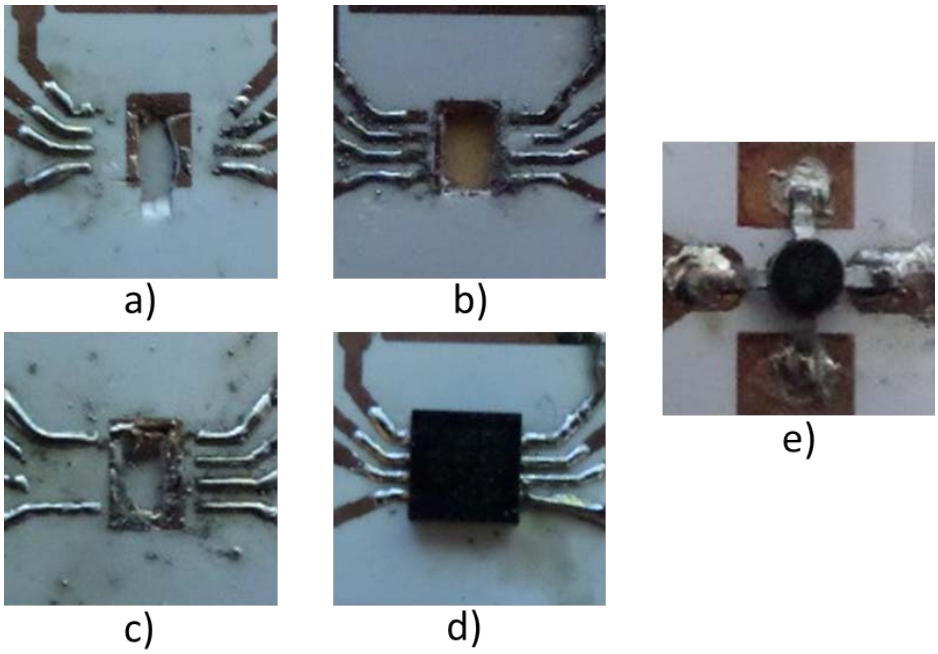

Fig. 3.8 a)-c) metal delamination after bridge removal d) successful mounting e) package choice for bridge prevention.

ent components when assembling the complete system for measurement. The R,L,C passive elements and small ICs were bonded with the low temperature solder paste already discussed. The solder paste did not fuse well with the bottom copper tape so the ground contact at the bottom of the mixer IC was bonded using solid solder, though this was challenging as well. While this ground connection did not require fine precision, wetting both the bottom IC pad and copper tape was quite difficult and required a lot of reheating increasing again the risk of damaging the mixer IC. The VCO had a gold finish and needed to be bonded with conductive silver epoxy then cured. The SMA connectors were best bonded using solid solder with medium difficulty. The result of each material can be seen in Figure 3.9.

Using manual assembly procedure following the inkjet printing was a positive step towards a truly low-cost, environmentally friendly technology process because it completely eliminated the need for expensive equipment. For realizing large systems with high repeatability however, a heat-controlled single-step assembly process is the most efficient, both for repeatable performance and high throughput. In order to reduce tedious reassembly, the heating tool was changed from a soldering iron to a temperature controlled oven. This allowed for much more thorough experimentation of the paste properties and the development of a thermal profile. The manual assembly procedure

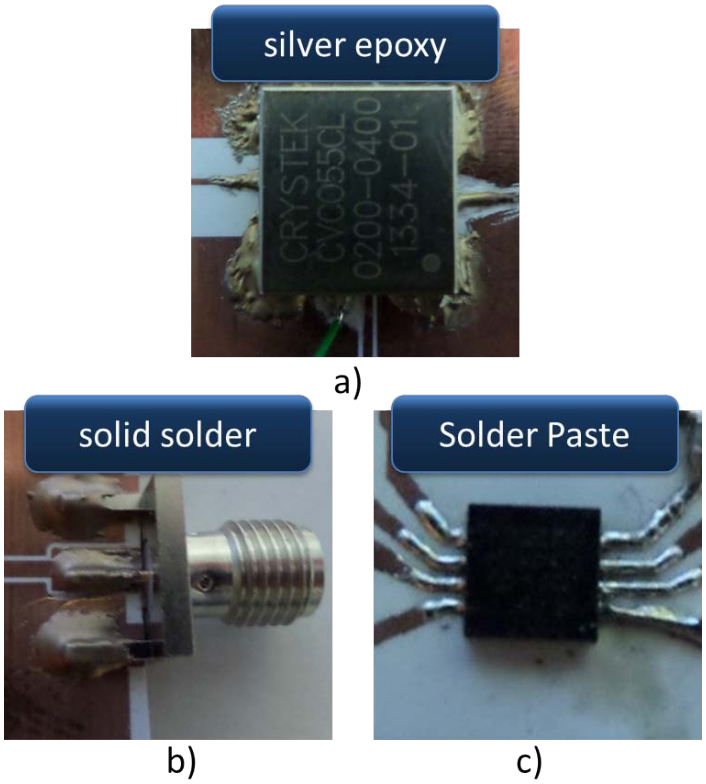

Fig. 3.9 Bonding materials used to attach components to Cu contact pads inkjet printed onto PET a) poxy glue, b) solid solder and c) solder paste.

had actually allowed the close observation of the paste flow behavior and its interaction with the copper film and substrate material, proving valuable information that assisted in the establishment of the thermal profile for the heat controlled process.

In the heat controlled procedure, the paste was deposited at all locations and the components were temporarily placed. The oven was preheated for 90 seconds at 130 °C to gradually increase the device temperature at a safe rate and activate the paste flux. Next, the temperature was increased to a maximum temperature of 155 °C for 55 seconds for the paste to flow. Afterwards, the device was allowed to cool down to 60 °C. This controlled heating allowed the paste to establish the tight bonds between the copper layer and components in one single heat cycle without damaging the substrate. The precision of the thermal profile was very important. Temperatures too low resulted in inadequate flow of the paste and unstable contacts while temperatures too high resulted in in excessive flow of the paste that created short circuits, or damaged the printed conductive films, the substrate or the components.

The controlled heating allowed the paste to establish the bonds between the copper

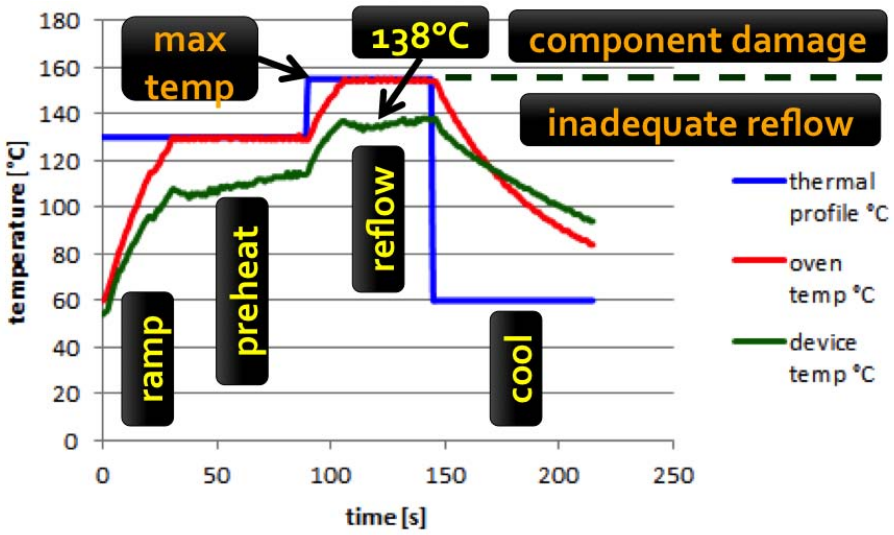

Fig. 3.10 Thermal profile settings, oven temperature, and device temperature used.

film and components in a single heating cycle while preventing damage to the PET and copper film as seen in Figure 3.11

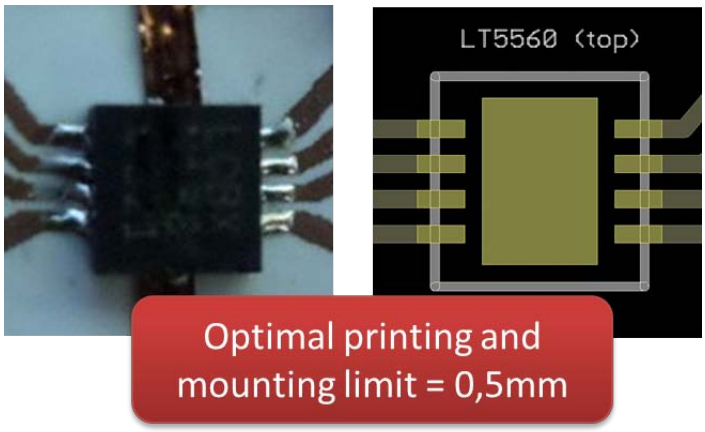

Fig. 3.11 Resolution limit reached for printing and assembling components onto flexible PET.

In the single-layer CADEagle fingerprint design, the crossovers were left open. They were constructed afterwards using a wire as seen in Figure 3.12a. If access to reprinting was possible, the crossover could actually be printed on top of the protective parylene coating as seen in Figure 3.12b. With controlled inkjet printing, very accurate alignment can be achieved for printing multiple layers.

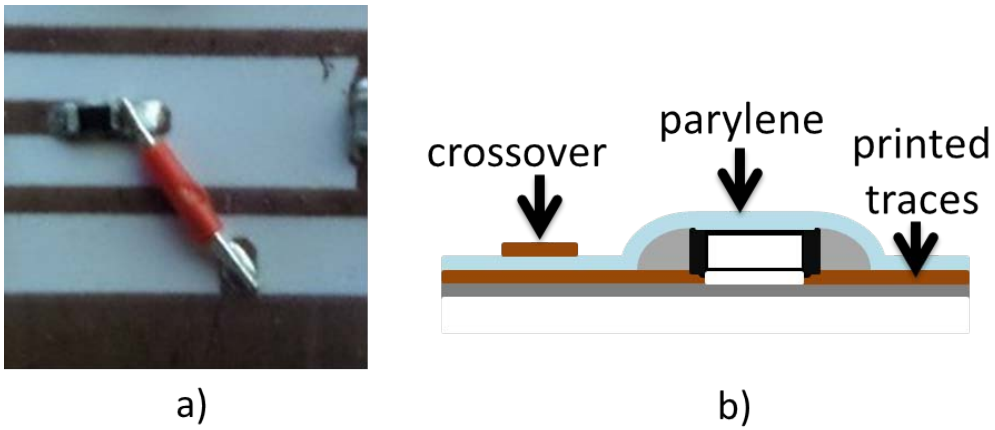

Fig. 3.12 a) wire crossover b) if using parylene for crossover then reprinting.

3.5 System design

Moving now from component level to system level, a few more challenges are introduced. For one, package availability limitations for other components made it difficult to minimize the bending radius which is limited by the size of of the largest IC of the system. In this case the VCO was the largest package on the board, measuring 12.7mm by 12.7mm compared to the mixer which measured 3mm by 3mm. Another challenge was that the manual mounting procedure was still being used during the complete system assembly. Uncontrolled multi-stage heating with a soldering iron, extended the assembly time, and the introduction of more components increased likelihood of accidents that could render the boards unusable. It was for this reason that the system complexity was kept at a moderate level in order to prove the fundamental performance operation; that all components could be mounted correctly, including the smallest component size and that the device functioned properly.

The system components consisted of a VCO, hybrid coupler, LNA and mixer as well as all their biasing and matching circuits. This system was intended to perform the most fundamental functions on rollable substrate including: demonstration of accurate voltage controlled signal frequency generation, perform amplification, perform conversion from RF to IF. The system design is shown in Figure 3.13

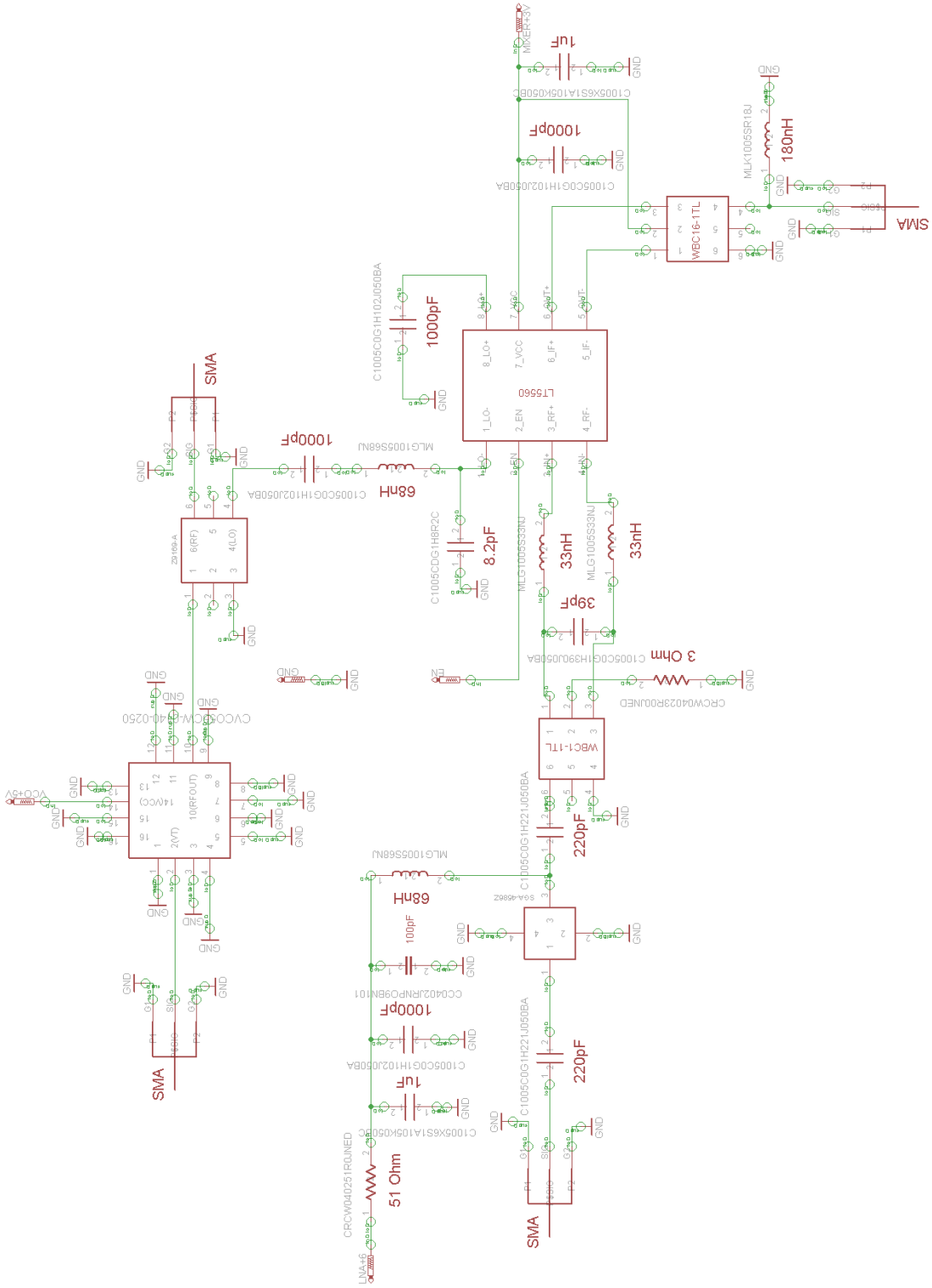

Fig. 3.13 CADEagle schematic.

The packages and pins for each component were drawn and labeled. The connections were assigned and verified as seen in Figure 3.13. The components were placed/positioned on the board according to basic rules. The connections were drawn and shaped. The CPW ground plane was manually drawn. Extensive reshaping of small spaces was necessary to ensure the footprint adhered to the printing resolution requirements as seen in Figure 3.14b.

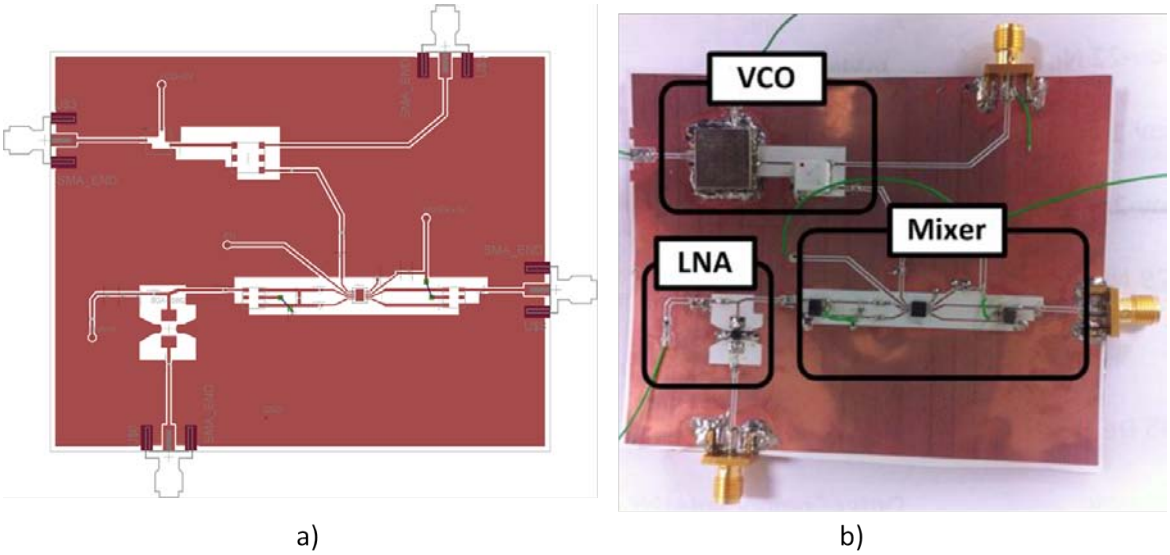

Fig. 3.14 Full system assembled on inkjet printed flexible substrate technology.

A parylene (-C and -N type) protective coating will be used. Parylene is a widely used chemical chosen for protecting devices that are medically implanted, undergoing harsh environmental conditions (including space), or that are subject to corrosion. Parylene is biocompatible, moisture resistant, chemically stable and can be used for microwave circuits because the electrical properties (ϵ_r = 2.4-2.95, tan δ = 6×10^{-4}-2×10^{-3}) do not interfere with performance. The thickness of the parylene is around 1-10 μm and can be varied. This parylene coating will prevent component delamilnation and cracking of the traces while the device is bent. It will also seal the device, protecting it from outdoor weathering during transportation or measurements.

In realizing the flexible FMCW architecture, the electrical design modifications made and the new low cost flexible materials introduced many challenges in the assembly, in particular the repeatability. Chapter 4 will demonstrate the experimental verification of the classical radar system and rollable radar system together. Performance limitation due to assembly electrical issues that arise when modifying the design for the inkjet printing process will also be shown.

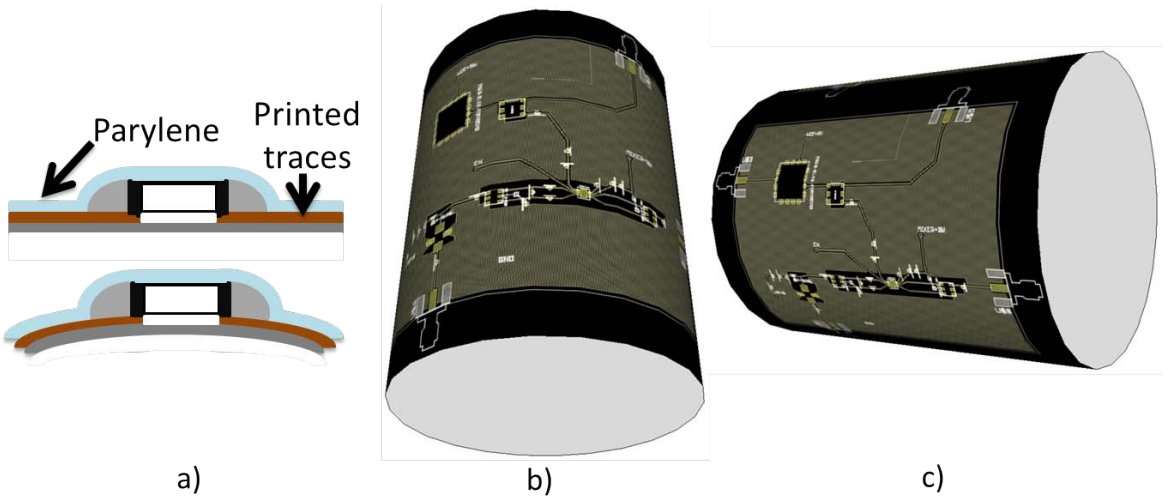

Fig. 3.15 Illustration of a) parylene coating b) flexible system layout.

Chapter 4

Measurement verification

4.1 SFCW GPR on classical technology

4.1.1 Introduction

The detailed study of the nature of groundwater has allowed for the establishment of a detailed set of system specifications. These system specifications were experimentally validated and used in the design of a flexible monolithic ultra-portable ground penetrating radar using inkjet printing technology. This section discusses the experimental setup that was used to verify the system specifications and analyze the performance under these specifications. The complete stepped frequency modulated continuous wave ground penetrating radar system consists of a unique combination of components, configured for the specifications. These include a Direct Digital Synthesizer to produce frequency steps using an external VCO reference clock, a power splitter to produce the RF and LO, and upon attachment of the second channel a quadrature phase shifter to produce both the I and Q local oscillator channels. For indoor measurements the front end is replaced with a delay cable to simulate the attenuation in the subsurface and the accuracy and reliability of target detection and range estimation. The receiver consists of the low noise amplifier to reduce noise influence for all subsequent stages, an optional power splitter to prepare the RF input for mixing with the I and Q functions, one or two mixers for conversion the IF beat frequency, a low pass filter and amplification stages, IF amplification stages and a VGA (Variable Gain Amplifier) which drives the Analog to Digital Converter that will digitize the data. An FPGA card is used to transfer the data between the ADC and PC and configure the ADC. The PC is used as a display to observe the spectrum data and

noise performance. This transmitter architecture is able to produce a high quality stepped frequency generation up to 400 MHz. Frequency steps outside of this band can be obtained simply switching the DDS model. Components satisfying the design specifications were chosen from various vendors including Crystek, Analog Devices, Broadwave Technologies, Linear Technology, Hittite Microwave and others. The component list is shown in Table 4.1.

Parts List		
Part	Description	Vendor
CVCO55CL-0800-0980	VCO	Crystek
CEVAL-055	VCO Eval Board	Crystek
151-173-002	Resistive Power Divider(s)	Broadwave Technologies
ABLJO-V 100MHz	VCO	ABLJO
AD9910	DDS	Analog Devices
ADL5391	Multiplier	Analog Devices
74VCX16374	D-Type Flip Flop	Fairchild Semiconductor
NC7WV07	Buffer	Fairchild Semiconductor
MRG1740	Cable 50Ohm RG 174 U	Belden CDT
BA50300-20-0.2	Power Amplifier	-
SBW	Biconical Antenna(s)	Satimo
DC933a (LT5512)	Downconverting Mixer(s)	Linear Technology
DC1027A (LT5560)	Low Power Active Mixer	Linear Technology
LT6600-20	IF Filter/Amplifier	Linear Technology
RF3827PCK-410	LNA Eval Board	RFMD
ADL5566-EVALZ	Dual Differential Amplifier Eval Board	Analog Devices
ADL5202-EVALZ	Digitally Controlled VGA Eval Board	Analog Devices
Eval01-HMC9000	Multi-GHz Quantizer	Hittite Microwave
FMC SP601	FPGA Board	Xilinx

Table 4.1 Parts List

4.1.2 Hardware

The Crystek CVCO55CL-0800-0980 VCO clock was selected that features a tuning sensitivity of 75 MHz/Volt, accepts a tuning voltage between 0.5V to 5V, and produces

an output frequency between 800 MHz and 980 MHz with a power level of up to +3 dBm. In the hardware configuration used, the maximum tuning voltage corresponding to the maximum VCO output frequency of 980MHz was used in order to obtain the maximum possible DDS output of 400MHz. The VCO is supplied by 5V and has load impedance 50Ω. Critical performance challenges of the VCO are phase noise. The DDS accepts a reference clock with a maximum frequency of 1000 MHz and produces an output frequency of 40 percent of the reference clock frequency (or 400MHz). It features a frequency stepping resolution down to 0.23 Hz, a 14 bit ADC and is supplied by 1.8V and 3.3V. The DDS is controlled through the ADS software, however requires computer settings to English (using the . instead of a ,) is required for the software to function, as well as connection of the USB cables and instillation of all necessary drivers. Critical performance challenges of the DDS are digitally induced spurious performance (wideband SFDR < 80dBc) and amplitude modulation at the output. The 151-173-002 (Broadwave Technologies) resistive power divider was used at the DDS output. The Low Noise Amplifier (RF3827-PCK410) features a small signal gain of 20dB, noise figure of 1.2 dB and is supplied by 9V. Two different active mixer models were used, the LT5560 specified to feature a typical conversion gain of around 2.4dB. It accepts RF, LO inputs and IF output up to 4GHz. The matching circuits were selected to cover the RF, LO and IF frequencies specified for this particular system, found on the DC1027A evaluation board designed for VHF down-converting applications, featuring RF input frequencies from 115-295MHz, LO input frequencies 180-310MHz and IF output frequencies 3-60 MHz. The LO drive level is -2dBm (-6 to 1dBm). It is supplied by 3-5V. The LT5512 was also used, specified to have a conversion gain of around 1dB. It accepts RF and LO inputs up to 3GHz, and IF output up to 2GHz. The matching circuits were selected to cover the RF, LO and IF frequencies specified for this particular system, found on the dc933a. The LO drive level is from -11dBm to 1dBm The conversion gain for the frequencies of interest was measured for both mixers (see measurements section). The IF Amplifier (ADL 5566) has a fixed 16dB gain and is supplied by 3V and 5V. For outdoor measurements, additional stages may be connected to obtain enough gain for adequate digitization. The VGA (ADL5202) is used in order to ensure the appropriate input power level for analog to digital conversion. It features a variable gain up to 20dBm and is supplied by 5V. The Analog to Digital Converter has a 50 Ω input resistance, 1Vpp full scale level, maximum sampling frequency 1GHz and 12 bit resolution. Due to the very high sampling frequency, the ADC board required extra heat sinks to reduce the risk of

damage over time. Some of the components, such as the quadrature phase shifter, were not available on evaluation boards for the frequencies of interest and therefore the components required for the construction were obtained. Coaxial cables were cut to make all connections between components.

4.1.3 System construction

A portable measurement setup was constructed where each component, including the delay cable and power supplies were stabilized onto one single single board (FIgure 4.1a). Custom length coaxial cables were attached between components for the RF signal. The setup was made to be compact enough for easy transportation and an area of the board was left available to hold a laptop for running the software. The hardware setup for the indoor measurements is shown in Figure 4.1b and Figure 4.1. In this setup, the power amplification stages, some IF amplification stages, and Q-channel were left out as they were not needed to benchmark the range estimation performance. The power amplifier (10MHz-3GHz feature 20dB gain). Figure 4.2a and Figure 4.2b show the indoor setup and the schematic for the outdoor setup, which all components have been obtained for.

4.1.4 Software

Direct Digital Synthesis

The DDS software (Figure 4.3) will run only when the VCO is on functioning correctly and the PC is recognizing the DDS hardware. The DDS can produce output frequencies up to 40 percent of the clock frequency, any frequencies above this limit will produce aliased images, some of which cannot be filtered out by the anti-aliasing filter of the DDS. When selecting the frequency output or steps, the VCO frequency accuracy is very important. The value of $f_{vco,clk}$ must be manually entered into the DDS software. This value entered is used to generate the frequency tuning word for the chosen output frequency as in shown in (4.1.1).

$$FTW = round\left(2^{32}\left(\frac{f_{out}}{f_{vco,clk}}\right)\right) \tag{4.1.1}$$

To ensure accurate frequency generation, the VCO frequency output for a particular tuning voltage should be measured with a spectrum analyzer before each measurement. This will ensure the correct output frequency is generated ((4.1.2)). The

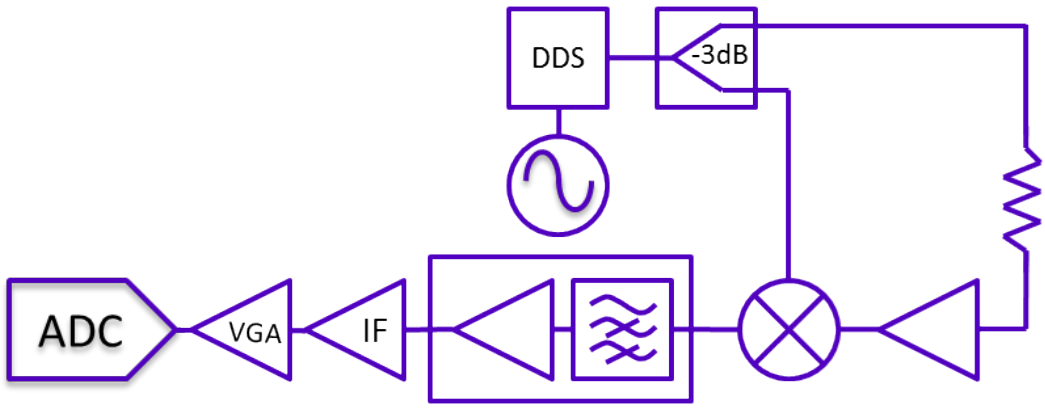

(a) schematic of indoor setup

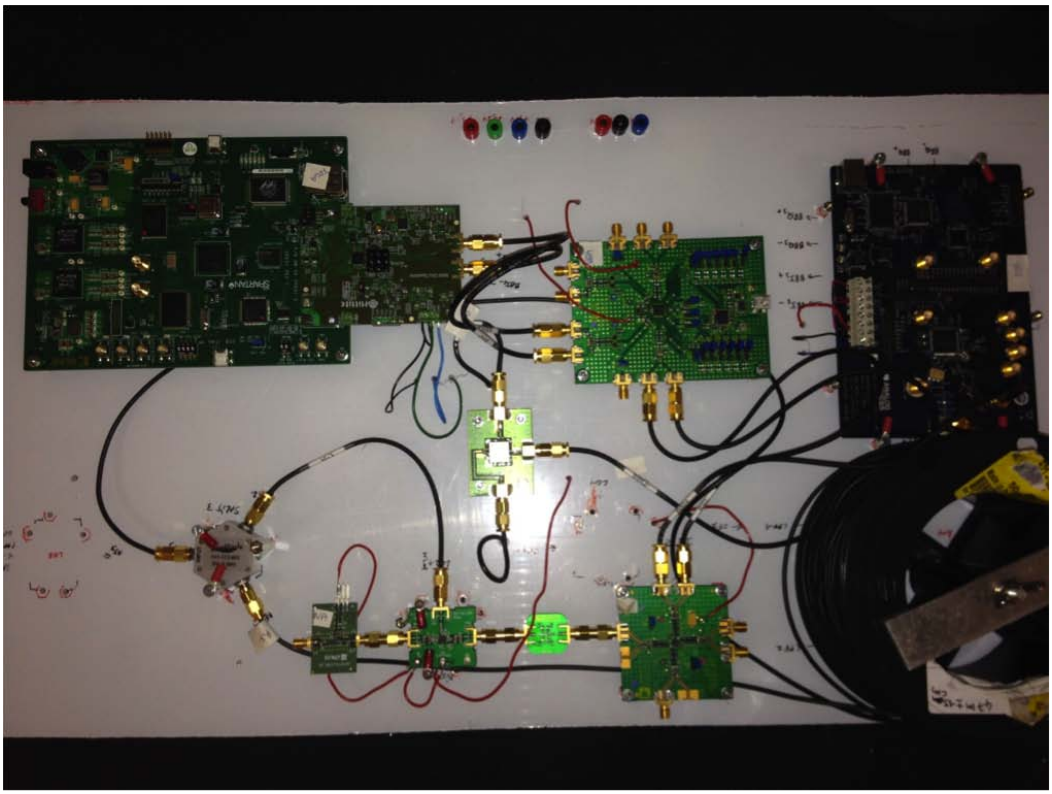

(b) indoor hardware setup

Fig. 4.1 Indoor setup.

actual output frequency will vary depending on weather or not the frequency divider is disabled.

$$f_{out,DDS} = \left(\frac{FTW}{2^N} f_{vco,clk}\right) \tag{4.1.2}$$

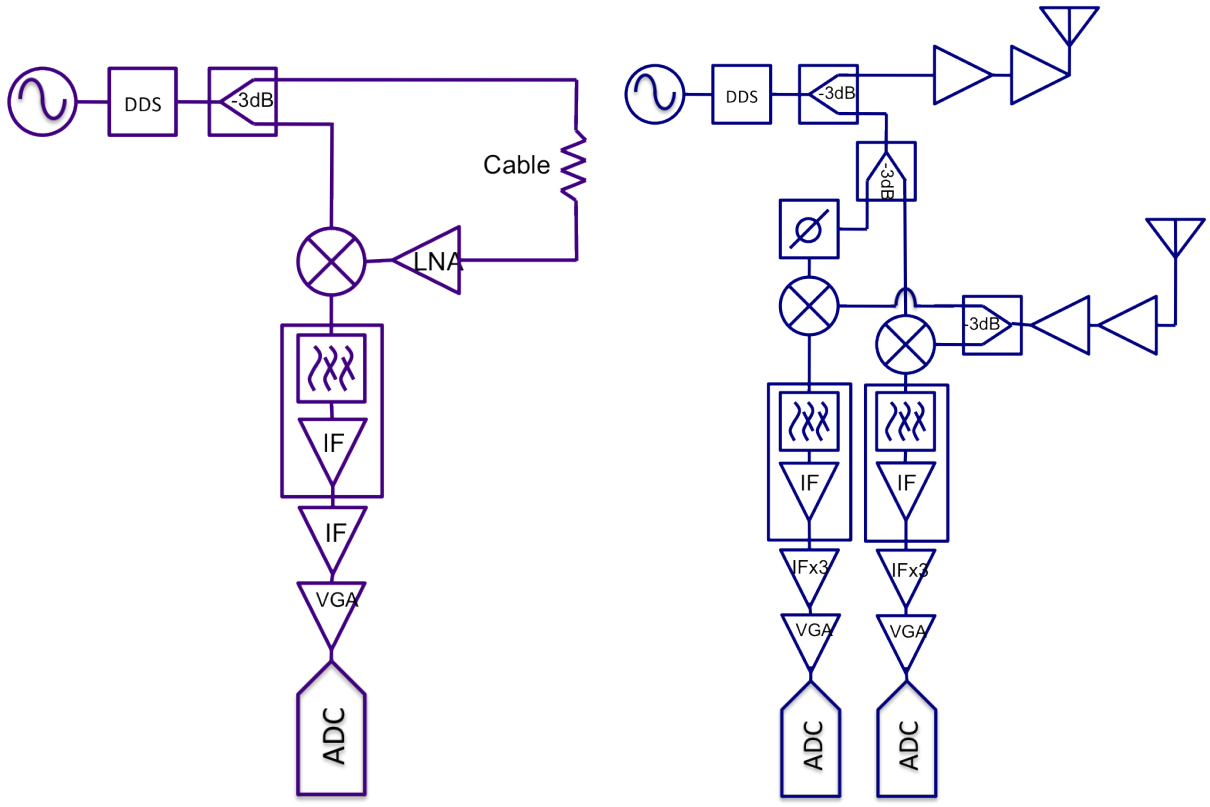

(a) indoor setup

(b) outdoor setup

Fig. 4.2 Indoor setup.

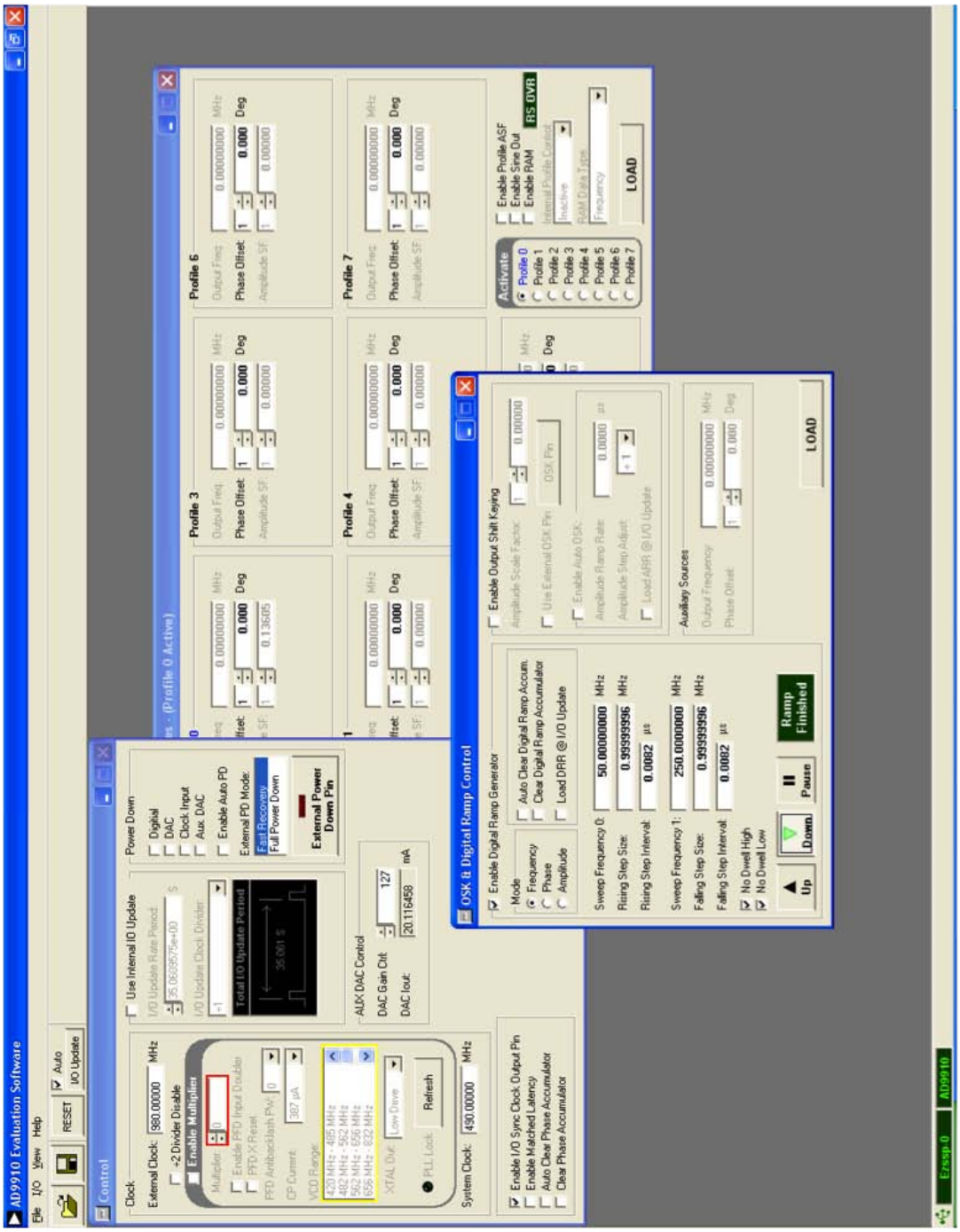

Fig. 4.3 DDS Software.

where N = 32 for a 32 bit phase accumulator. When observing the DDS output, various sources of spurious emissions, some less than 80 dBc below the wanted signal were be observed. One source is VCO phase noise. Depending on the configuration, enabling or disabling the frequency divider strongly affects the phase noise performance, this can be observed by viewing the output at one frequency through an oscilloscope. Another source of spurious is the finite number of bits used by the phase accumulator to increment the phase each clock cycle from 0 to 2π. This phase truncation causes phase modulation in the accumulator output. The sine lookup table which performs the phase to amplitude conversion also has a finite length and introduces amplitude modulation. Aliased images created by DAC nonlinearity that cannot be filtered out are another sources of spurious.

Analog to Digital Converter

An Analog Digital Converter on an SPI-enabled evaluation board is used. The ADC sampling frequency, FFT length and SPI control was configured by the EasySuite software installed on the PC. The EasySuite software (Figure 4.4) instillation must be performed correctly requires a significant amount of time and space. This software package was also used to analyse the frequency spectrum of the data output. The data is transported between the ADC and PC through the FPGA (Xlinx Spartan-6 FPGA Evaluation Board). The FPGA was programmed by installing the Hittite EasyStack firmware onto it. This performs the programming necessary to generate the appropriate configuration file for the board.

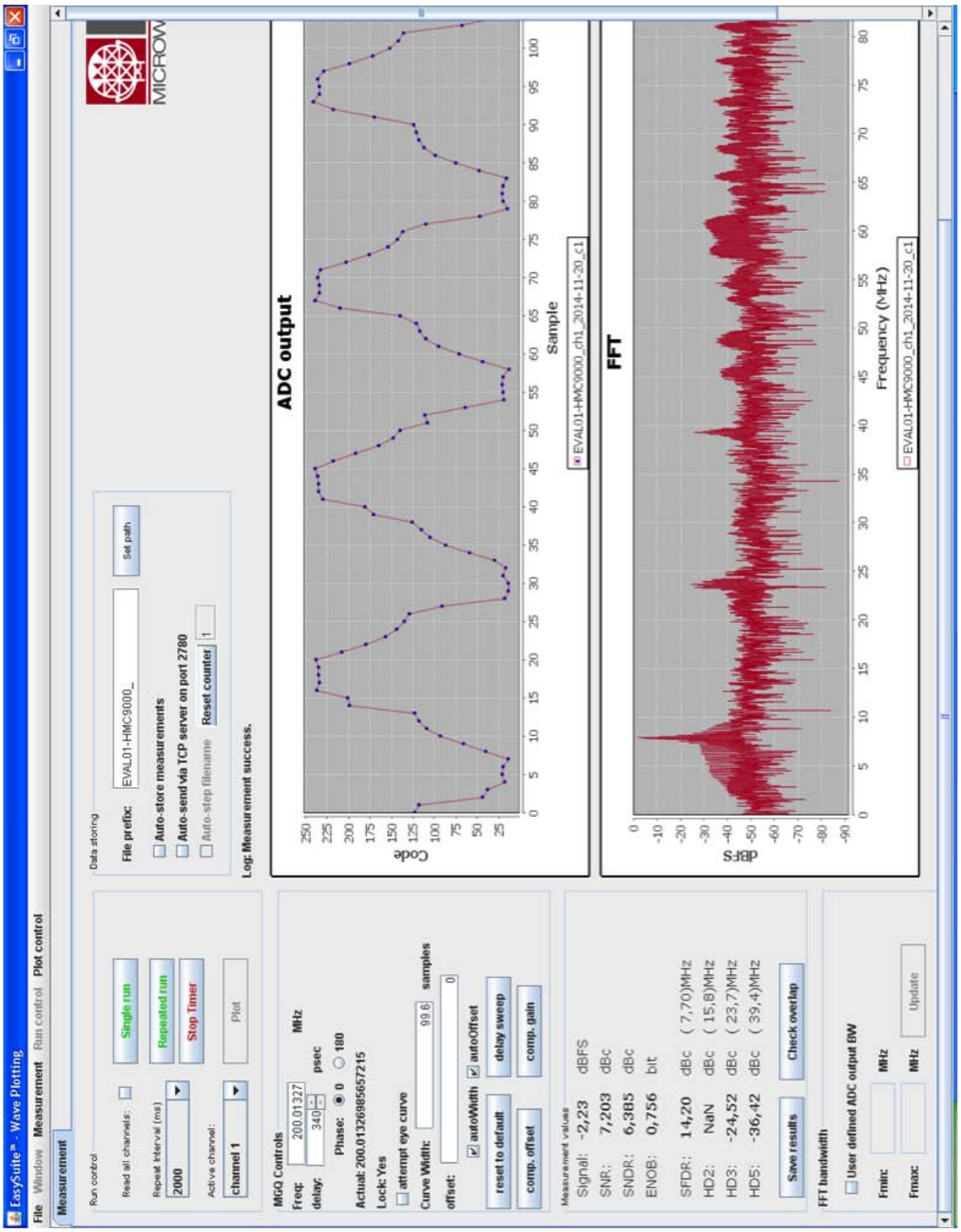

Fig. 4.4 ADC software.

4.1.5 Measurements

Introduction

The measurement setup can be seen in Figure 4.5. The DDS output power was specified as +4dBm but for this particular setup measured to be -7dBm. The power from at the 3dB splitter at the output of the DDS was measured and confirmed to be -13dBm. The power fro; the 47 +/- 15cm delay cable was measured to be -25.6 dBm. The conversion gain of each mixer was measurd to be 5.8dB and 10.6 dB.

4.1.6 Measurement data

In this work, the experimental validation is performed through observing the spectrum and power level characteristics of the ADC output (Figure 4.6, Figure 4.7 and Figure 4.8). The SNR (signal to noise ratio) is the ratio of the signal power to the noise power excluding any non-linearities that may exist. The SNDR or SINAD (Signal-to-noise + distortion ratio) is the ratio of the signal power to the noise power, including sprious due to non-linearities (excluding any DC components). $SINAD = (P_{sig} = P_{noise} + P_{distortion})/(P_{noise} + P_{distortion})$. The SINAD can be converted to ENOB. The ENOB (Effective Number Of Bits) is the number of bits an ideal ADC would have to obtain the same resolution. $ENOB = (SINAD\breve{}1/76dB)/6.02 = (SINAD_{measured}\breve{}1.76dB + 20log(V_{FS}/V_{input}))/6.02$, where V_{FS} is the FullScale Amplitude and V_{input} is the input amplitude. The SFDR (spurious free dynamic range) is the dynamic range throughout which no non-linearities exist. The HD is a measurement of the harmonic distortion. These performance parameters are computed using very advanced measurement software and allow for benchmarking of the system performance.

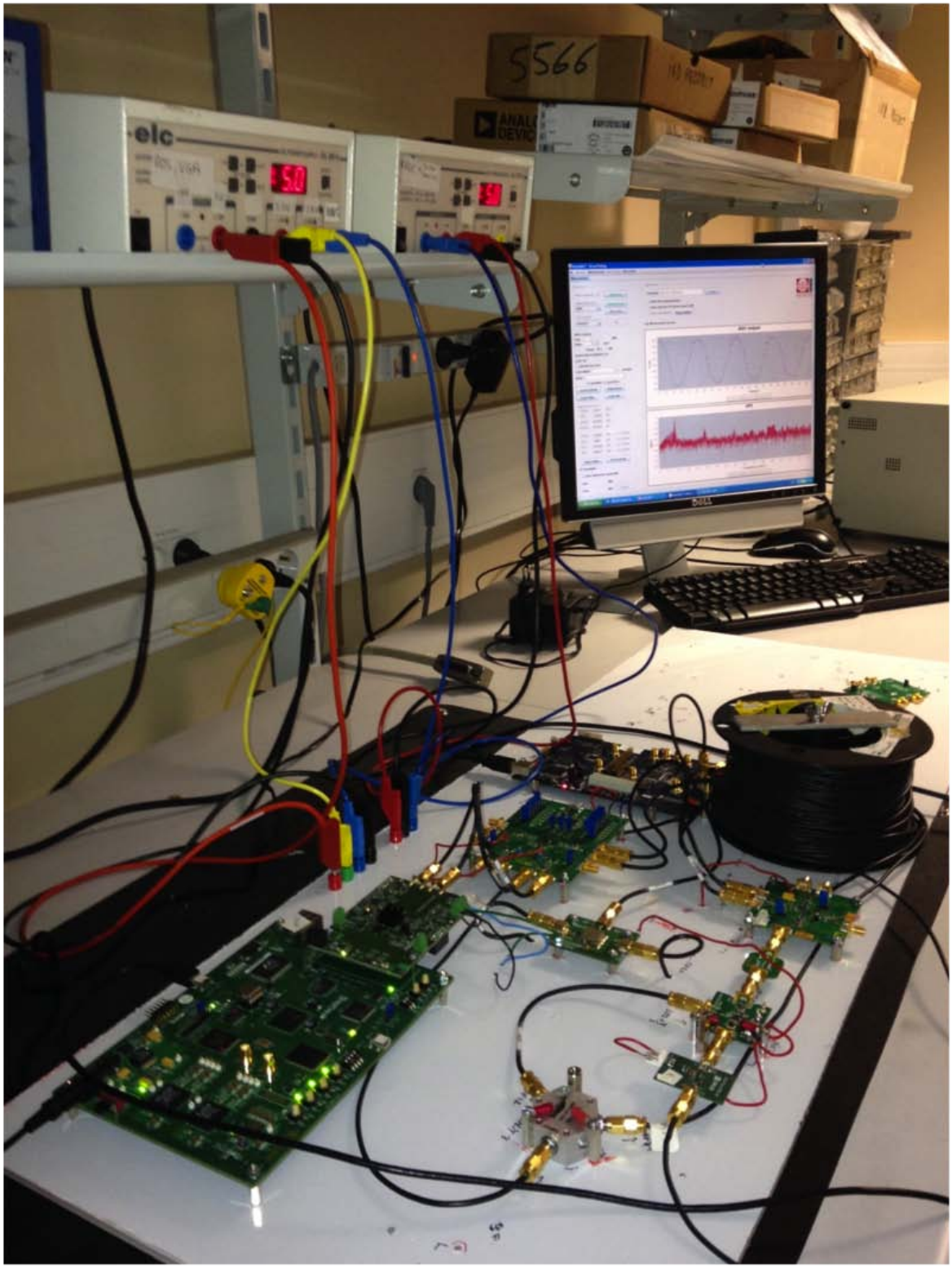

Fig. 4.5 Measurements.

DDS settings	
sweep	50 MHz – 250 MHz
t_d	0.0082 µs
Δf	1 MHz
ADC output (fs = 1GHz)	
Signal	-4.72 dBFS
SNR	6.314 dBFS
SNDR	5.227 dBFS
ENOB	0.576 bit
SFDR	7 dBc (63.6 MHz)
HD2	NaN dBc (125 MHz)
HD3	-32 dBc (187 MHz)

DDS settings	
sweep	50 MHz – 250 MHz
t_d	0.0163 µs
Δf	1 MHz
ADC output (fs = 1GHz)	
Signal	-3.3 dBFS
SNR	7.673 dBFS
SNDR	7.093 dBFS
ENOB	0.9886bit
SFDR	2.79 dBc (30.8 MHz)
HD2	NaN dBc (63 MHz)
HD3	7.41 dBc (94 MHz)

DDS settings	
sweep	50 MHz – 250 MHz
t_d	0.0327 µs
Δf	1 MHz
ADC output (fs = 1GHz)	
Signal	-3.85 dBFS
SNR	8.977 dBFS
SNDR	8.536 dBFS
ENOB	1.13 bit
SFDR	17 dBc (47 MHz)
HD2	-40 dBc (32 MHz)
HD3	-27 dBc (47 MHz)

DDS settings	
sweep	50 MHz – 250 MHz
t_d	0.0408 µs
Δf	1 MHz
ADC output (fs = 1GHz)	
Signal	-4.45 dBFS
SNR	8.791 dBFS
SNDR	8.366 dBFS
ENOB	1.1 bit
SFDR	4.21 dBc (37.8 MHz)
HD2	5 dBc (25.3 MHz)
HD3	9 dBc (37.8 MHz)

DDS settings	
sweep	50 MHz – 250 MHz
t_d	0.0490 µs
Δf	1 MHz
ADC output (fs = 1GHz)	
Signal	-5.88 dBFS
SNR	8.447 dBFS
SNDR	7.928 dBFS
ENOB	1.02 bit
SFDR	2.3 dBc (31 MHz)
HD2	NaN dBc (21 MHz)
HD3	4.83 dBc (31 MHz)

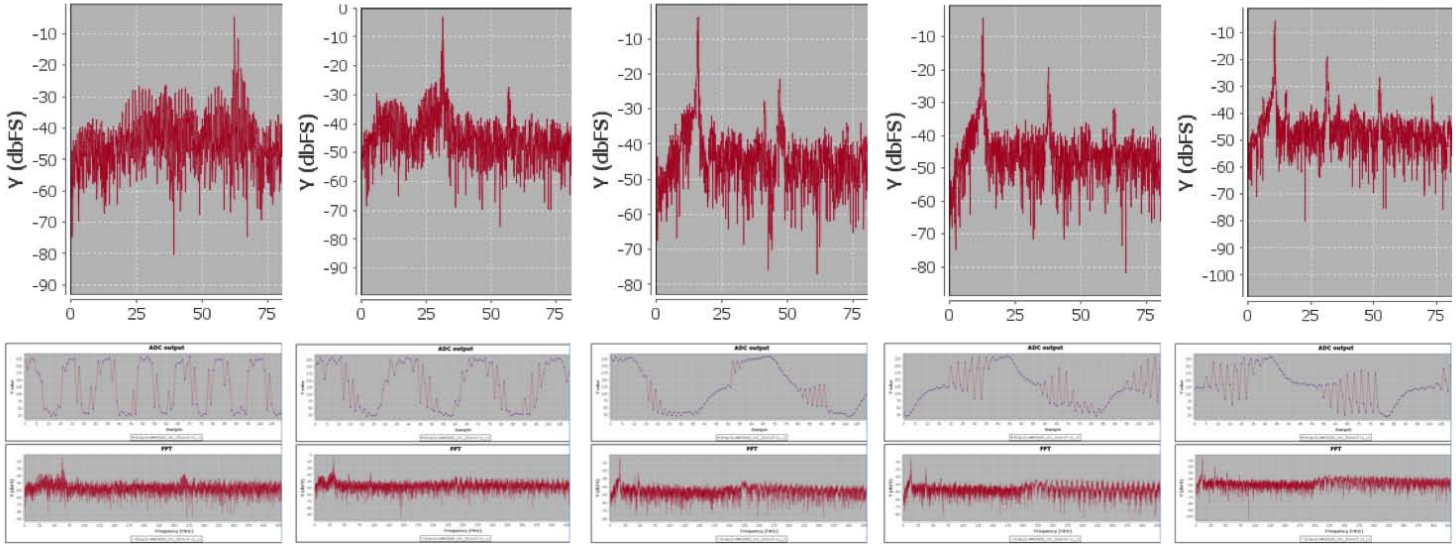

Fig. 4.6 Measurement data (B = 200 MHz).

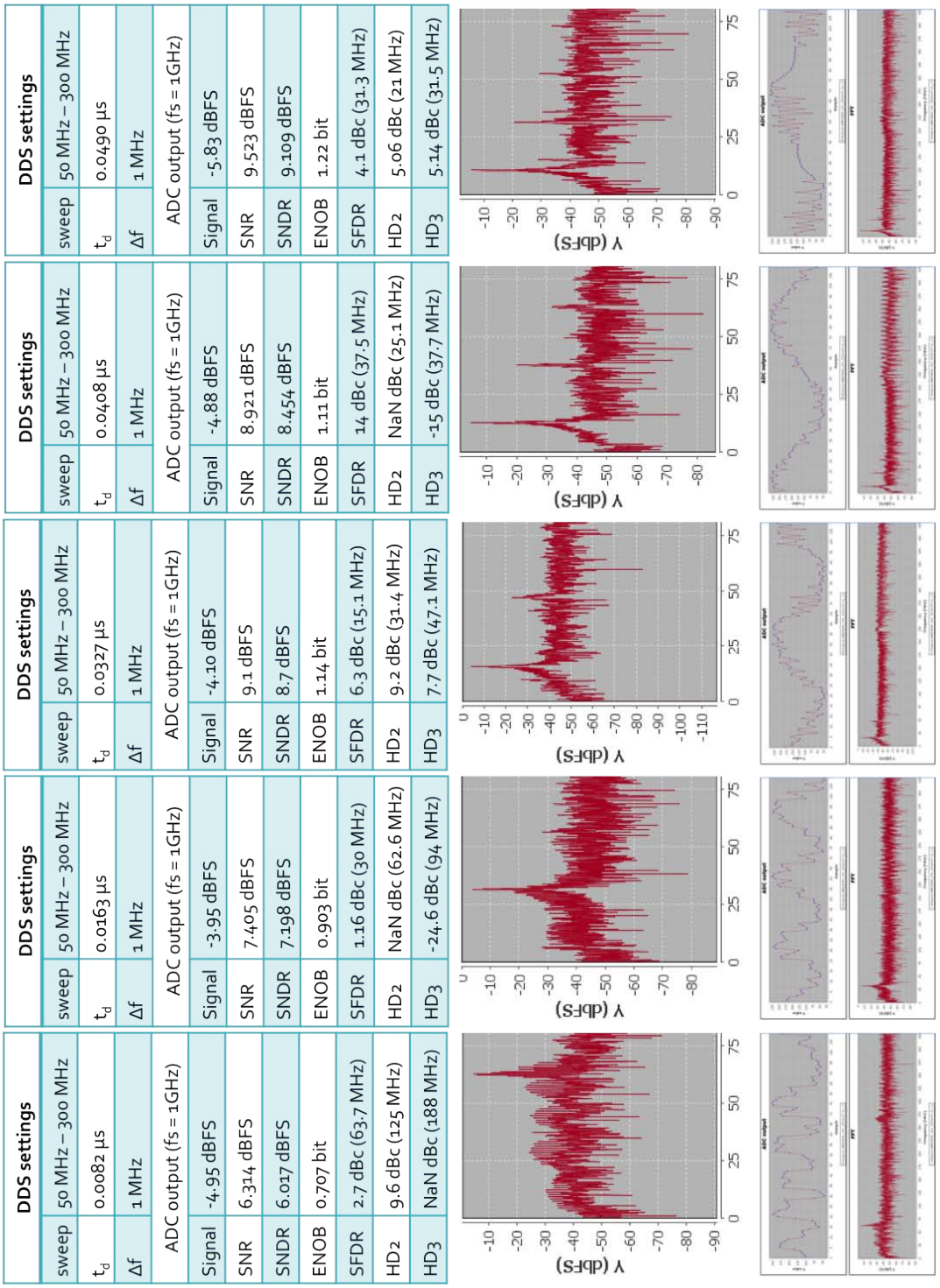

Fig. 4.7 Measurement data (B = 250 MHz).

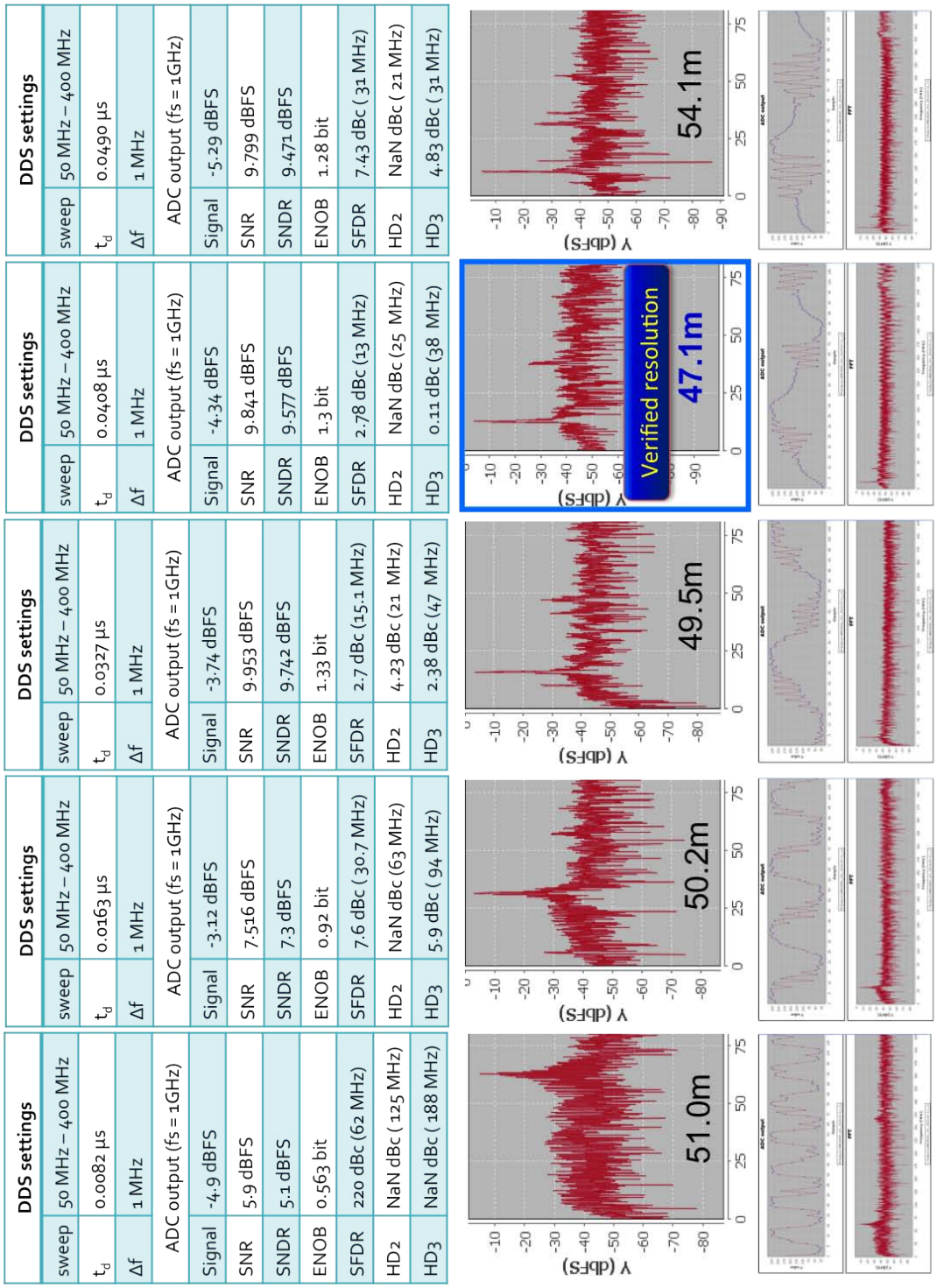

Fig. 4.8 Measurement data (B = 350 MHz).

4.1.7 Conclusion

The focus of this chapter was to establish and experimentally verify the system specifications required for a ground penetrating radar system dedicated primarily to the detection of groundwater at large depths. The primary challenge was the degree of complexity to develop a complete system which involved extensive work in a variety of different domains including: geophysics, electromagnetics, RF design, analog electronics, signal processing, and detection of signals in noise. Specific problems ranging from system level down to the transistor level required very careful organization and prioritization of system tasks and goals. The most efficient development solution was to take a top down approach by focusing on the system level aspects and integrating some already available componets into the system while making the appropriate modifications when necessary (such as redesigning or modifying components that were not available for the frequencies used). As radar technology is quite mature, the system design involved the integration of commercial components. This is a common approach used in radar system design. According to two different state of the art systems developed: “This aspect is also extremely difficult to attain and involves a lot of research activity and expenditure. Hence, the need arise to find a way of building a radar from commercial components (Commercial Off The Shelf—COTS) so as to keep the cost minimal and yet not lose out on high resolution, even if it is a synthetic one (since we process the signal using an IFFT, as discussed in Chapter 6). It was keeping this aspect in mind, that this radar was conceived“ [van Genderen] Most systems are based on a standard architecture that is customized for the particular application “To reduce cost and development time, we used a modi!ed version of a 500–2000 MHz FM-CW radar that was developed at the Radar Systems and Remote Sensing Laboratory at the University of Kansas to map near-surface internal layers over the Greenland ice sheet as a means to estimate the accumulation rate (Kanagaratnam et al., 2001, 2004)” [Holt 2008]

To realize a complete system designed for groundwater detection, a thorough investigation of the nature of groundwater was performed that included the establishment of a detailed power budget to accurately estimate the propagation behavior versus frequency for different materials. This allowed the creation of a very detailed set of system specifications that were compatible with available hardware. These specifications included the transmit waveform, power requirements, receiver design, digitization and signal processing specifications. The measurement performed provided an experimentally validated foundation for which to compare to the flexible monolithic

ultra-portable ground penetrating radar using inkjet printing technology.

4.2 Measurements of FMCW system in inkjet printed rollable substrate

4.2.1 Introduction: Assembled system

The assembled system measured 8cm by 10cm and contained a total 31 compoonents. First, the RF output port of the VCO was tested. The VCO used was a Crystek model featuring a tunable frequency range of 200 MHz to 400 MHz when using a tuning voltage from 0 to 5V. This corresponded to the GPR frequencies established in Chapter 2. There was no PLL so the VCO output was observed (Figure 4.9b) to verify that precise output frequency control. The LNA performance was also verified, as amplificaiton of the signal was demonstrated. Very unique precautiouns had to be taken when setting up the measurement configuration so that the heavy instrumentation did not pull or tear the SMA connectors off the flexible device, or twist the device itself. This was especially critical for prototypes without the protective coating.

4.2.2 Unrolled system

To generate the frequency sweep, the VCO was swept by manually stepping the tuning voltage to maintain the established frequency control and oscillator stability in the absence of a PLL. Experimental validation of the tuning characteristics of the VCO measured output power level of 0dBm can be seen in Figure 4.9. The complete system (from the signal generation to the IF output) was measured by tuning the VCO to generate the LO frequencies of 217 MHz, 222 MHz, 228 MHz and 234 MHz and applying an RF input of 200 MHz to the system RF input port. IF frequencies of 17 MHz, 22 MHz, 28 MHz and 34 MHz were observed, measured and recorded verifying the basic functionality of the system. This experiment confirmed the fundamental performance operation capabilities of the system when using an architecture that was well chosen and correctly assembled. As the complexity of the architecture increases, so will the system area and number of components, stressing the importance of good repeatability of the newly established assembly procedure

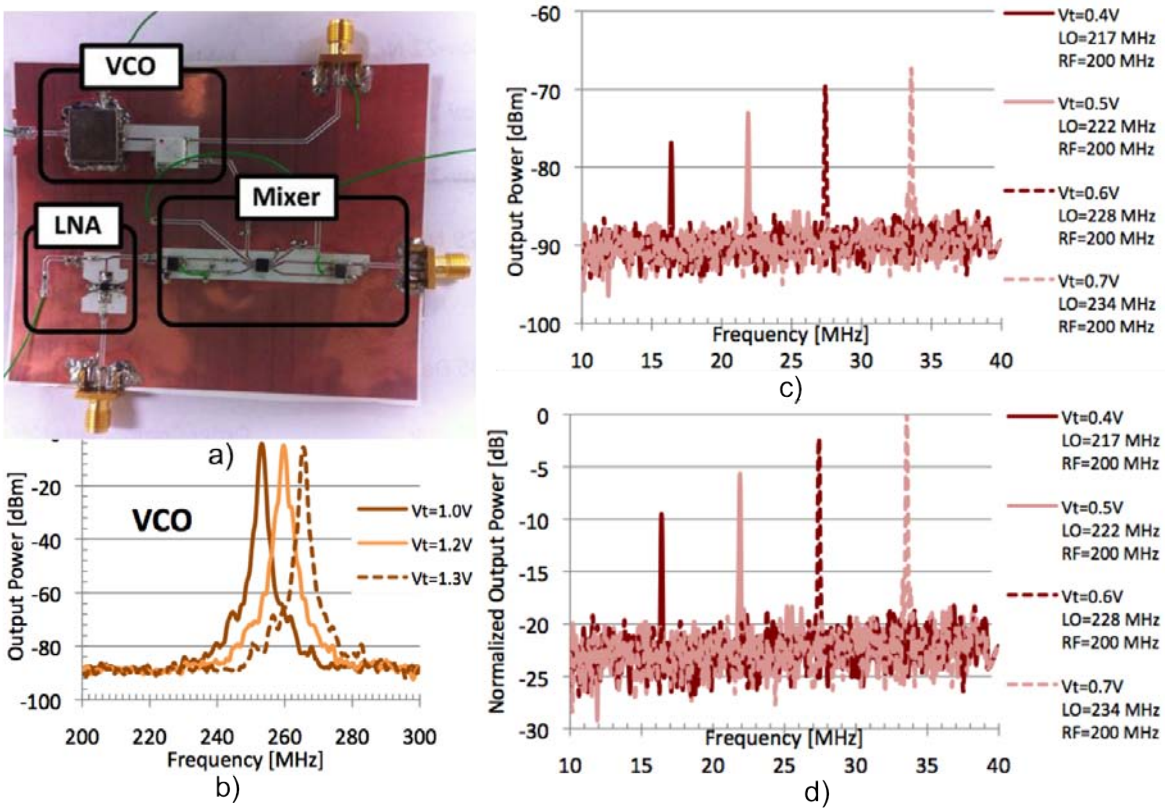

Fig. 4.9 Measurements of rollable radar module a) fabricated system b) VCO output c) full system measurements, mixer output d) full system measurements, mixer output (normalized).

4.2.3 Rolled system

A bending test (Figure 4.10) was performed to test the adhesion of the assembled components and the printed copper film and and to verify the system performance would not degrade after it has been in a rolled state, as would be when stored in a container. As an extra step, the dynamic performance was tested by leaving the system in a rolled state and performing the measurements. The dynamic performance is a good indicator of the quality of the electrical contact which may have a tendency to fail when using a paste that is brittle, or that has a low melting temperature. To perform this test, the 8cm by 10cm structure was bent both horizontally and vertically around foam cylinders of different radii. The critical bend radius was achieved with cylinder of radius 4.5cm (4.11). As mentioned in the design section, the primary factor that limited the minimum rollable radius was the size of the largest IC. In this case it was the VCO which had the dimensions of 0.5in by 0.5in. Regardless of this

current limitation, the full 10cm by 8am system could easily be wrapped around the 4.5cm radius without damaging the circuit due to delamination or cracking.

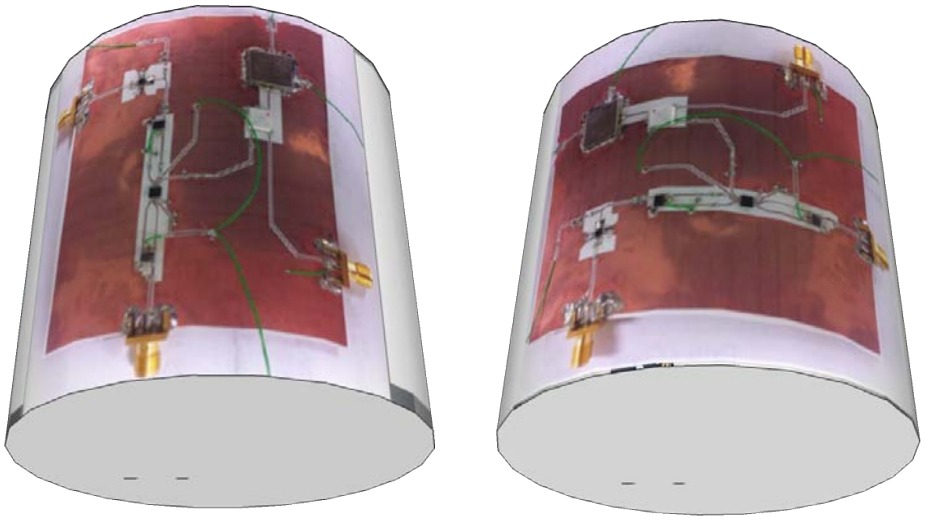

(a) vertical direction (b) horizontal direction

Fig. 4.10 Bending test.

The bending test verified the extremely strong adhesion properties and good flexibility properties of the copper film deposited to the PET substrate using the catalyst-based electrodeless electroplating technology process, even better so than the silver nanoparticle ink. The minimum bend radius of 4.5cm was limited by the size of the largest IC on the board, the VCO, measuring 1.3cm by 1.3cm. Miniaturizing the component in order to increase rollability means a smaller volume of paste must be used, therefore increasing the likelihood of contact failure and delamination when bending. This is why it is important to select the inkjet printing technology that demonstrates the best adhesion properties and finally adding a protective layer. The measured results showed a relatively bend independent fundamental performance operation in which the system continued to maintain electrical contact and performed the correct functions during bending without delamination of the components or cracking of the copper film. While the bending test was intended only to test robustness and quality of contacts, such a dynamic bending performance could be useful in the case that the radar system needed to perform while placed on an uneven surface, for example in GPR measurements where the system must be placed directly on uneven ground surface.

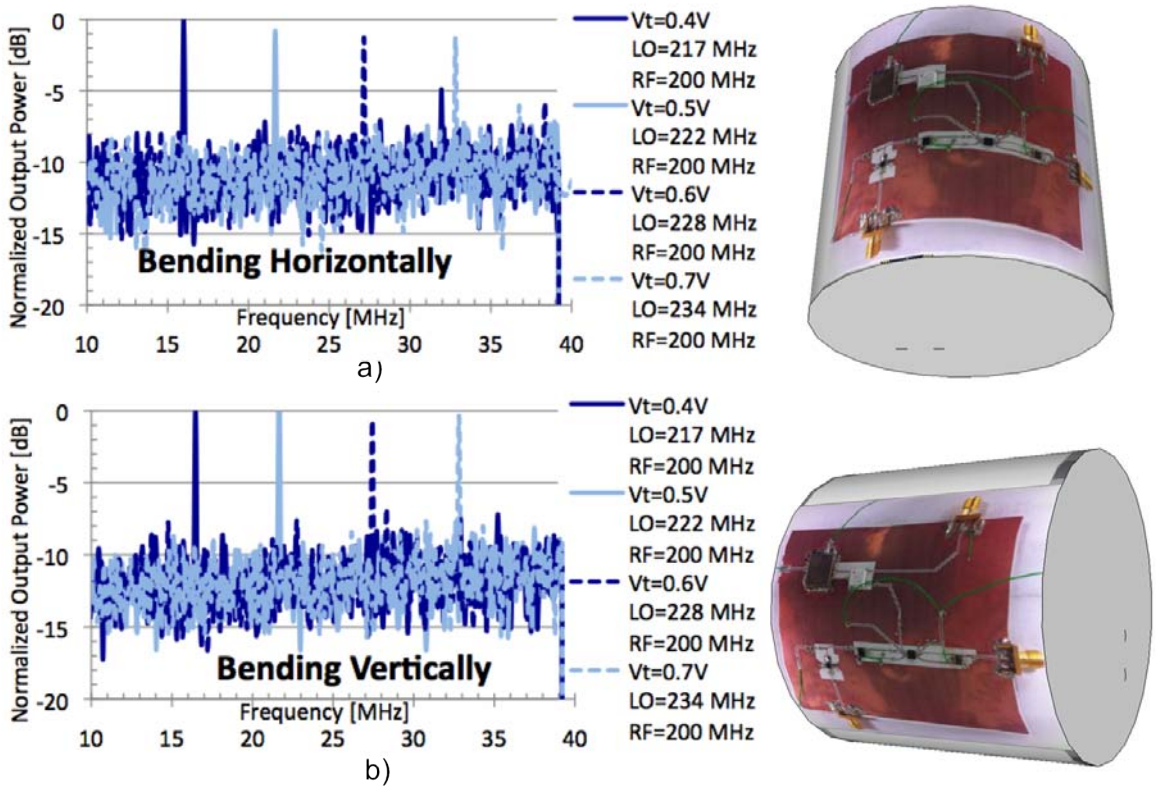

Fig. 4.11 Normalized output of the rollable radar system for horizontal and vertical bending around cylinder of radius 4.5cm.

4.2.4 Performance: Insertion loss

The only system weakness observed was a high level of insertion loss, with output powers measuring around -75 dBm. This insertion loss increased by as much as 10 dB when bending the devices around the foam cylinders. This meant that the mechanical strain being placed on the device was inducing electrical failure. Such a degradation in performance was the result of insufficient contact quality, or failure of already established contacts. To alleviate this problem, it was necessary to improve the quality of the contacts made in the assembly process by optimizing the thermal profile used in the oven.

Quality of contacts

The measurements in both unrolled (Figure 4.9) and rolled (Figure 4.11) systems verified the very satisfactory radar system performance by demonstrating the fundamental FMCW radar functions required to accurately detect a target at low depths including

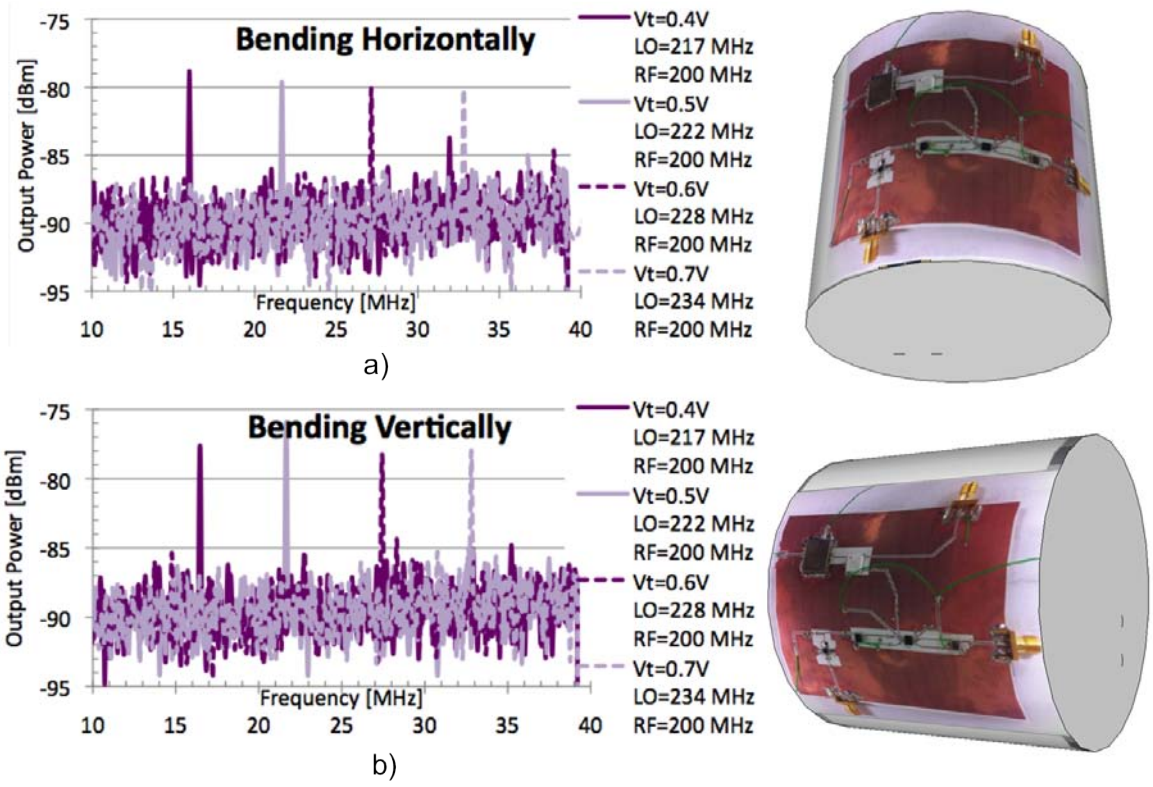

Fig. 4.12 Output of the rollable radar system for horizontal and vertical bending around cylinder of radius 4.5cm.

correlating the LO and RF signal to produce an accurate beat frequency. These results, however, also showed a high level of insertion loss with output power levels between -70 and - 75 dBm (Figure 4.12). The entire circuit was fabricated again to identify the sources of this successive insertion loss. At this stage the manual assembly procedure was still being utilized, so assembly was costly. Even upon successful bonding, the limited temperature control of the paste made it difficult to ensure good connections for all components. Despite this challenge, the entire system was remounted manually, including the mixer circuit having small pin size. The measurements were performed again and the insertion loss improved slightly, indicating improvements in the electrical contacts. The refabricated mixer displayed functional performance when applying RF input frequencies of 260 MHz and 230 MHz into the RF input port of the mixer and an LO frequency of 250 MHz into the LO port. The correct IF output of 10MHz and 20MHz was observed at an output power level of -50dBm (Figure 4.13b).

The difficulty in establishing precise, clean and uniform connections can be seen when comparing the manual process in Figure 4.14 with the heat controlled process in

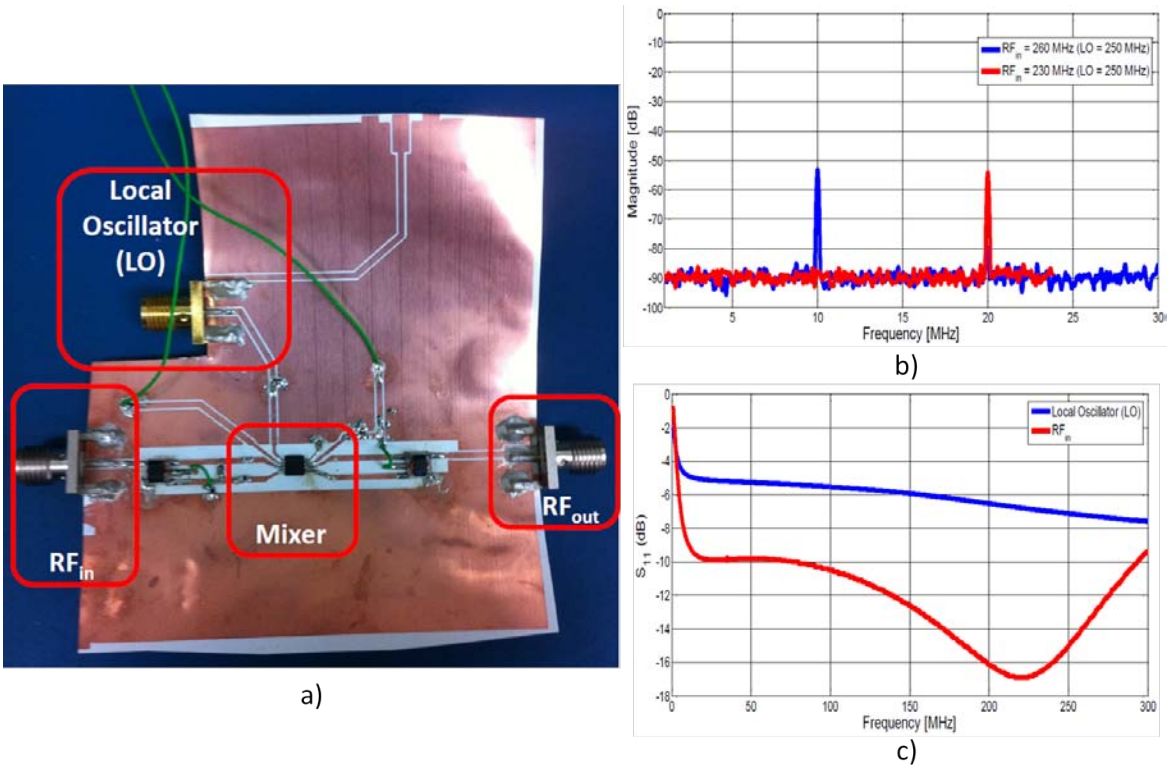

Fig. 4.13 Refabrication and measurement of mixer insertion loss.

Figure 4.15. A major step was made to reduce costly fabrication time while solving the various design problems encountered when moving a system to a heat controlled oven. This allowed for the accurate placement of the smallest IC with a high level of temperature control to reduce the risks of bridging, cracking, or reheating damage. The heat controlled assembly process however was also far from trivial. Designing a precise thermal profile is very challenging because it requires managing several very precise but conflicting parameters. The volume of paste used must be balanced between establishing secure contacts while avoiding short circuits. The thermal, mechanical and chemical behavior of the paste will determine how these contacts are established with respect to temperature and time and how reliable the contacts remain after construction. The $Bi_{58}Sn_{42}$ is Eutectic at 138C, the temperature at which the rapid transition from solid to liquid occurs. The thermal profile must be precisely brought to this temperature in order for the paste to flow. This severely conflicts with the thermal tolerances of the flexible substrate and individual components. The glass transition temperature of the Polyethylene terephthalate (PET) substrate is 70C and the melting temperature is less than 230C. The maximum storage temperature of the

smallest IC, the mixer circuit is 126C.

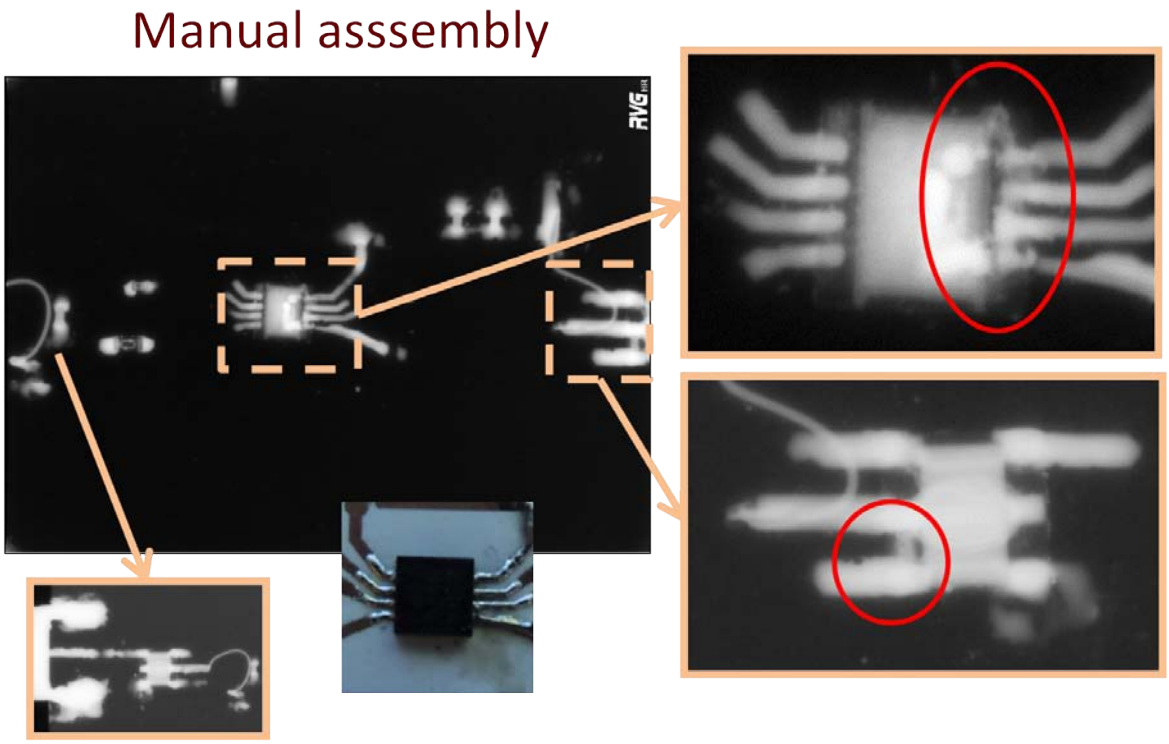

Fig. 4.14 Xray image of manually assembled circuit.

Electrical design

A large amount of insertion loss still persisted and after thorough testing, it appeared to originate primarily from the mixer circuit. In order to achieve practical and effective advanced system performance operation, a minimum insertion loss over a wide bandwidth was needed. The mixer was tested separately again from the rest of the system to observe the problem as seen in Figure 4.13a. This was a topology in which the low cost, rapid, wide area fabrication of multiple footprints for individual components really came into good use. This made it easier to solve the different design problems encountered throughout development. The mixer measurement results confirmed very good fundamental performance operation that improved when improving the contact quality however also confirmed that the high insertion loss was, in addition to the contact quality, an issue related to the electrical design of the mixer circuit. It originated from modifications in the layout to be compatible with the inkjet printing process. This introduced electrical performance issues, in particular energy leakage into parasitic CPW modes, causing a significant amount of the insertion loss in the

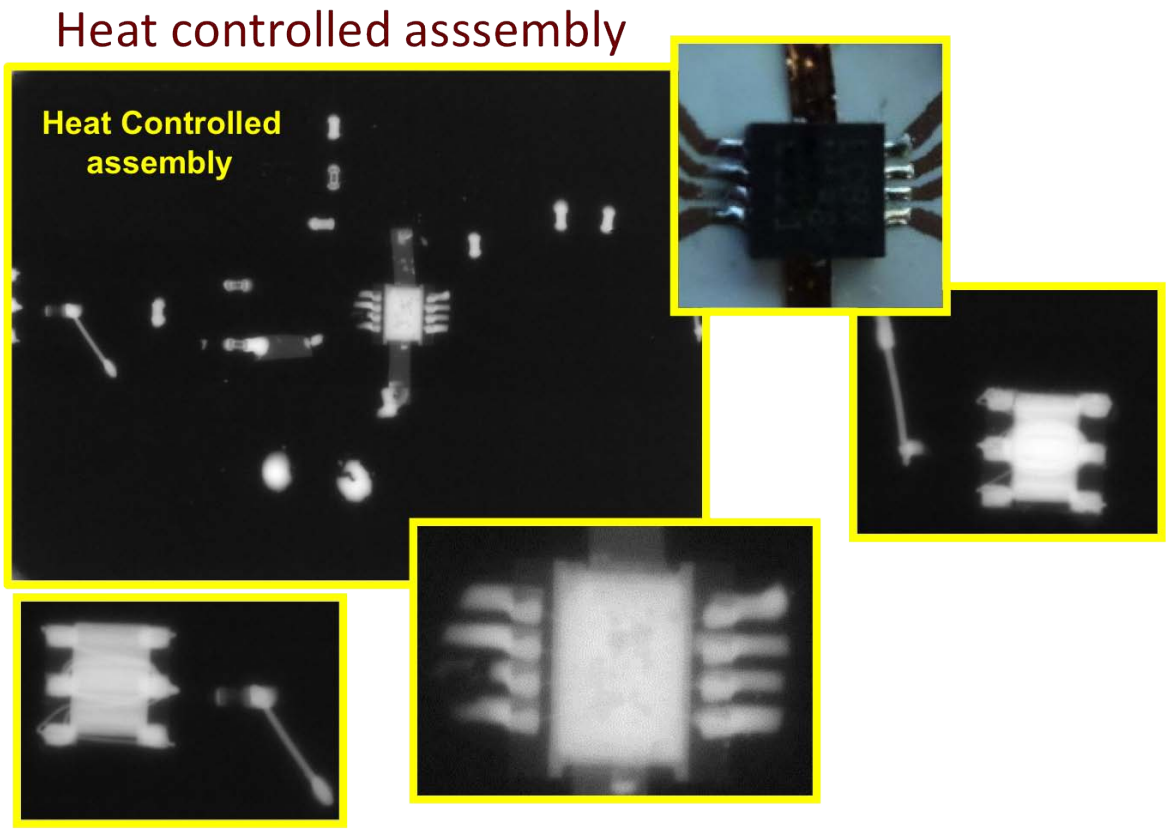

Fig. 4.15 Xray image of heat controlled assembled circuit.

mixer circuit. A wire of length less than one inch was connected from one of the balanced lines of the RF input port to the CPW ground plane as seen in Figure 4.16a. An improvement in insertion loss after adding this inductance is shown in Figure 4.16b when comparing the S11 of the *RF* dotted blue curve to the *RF new* solid blue curve in which the wire was added. The new circuit demonstrates a very good S11 of -14dB from 50 MHz up to 220 MHz compared to the previous circuit having an S11 of -2dB. This improvement is seen across GPR frequencies of interest discussed in chapter 2, however the rollable circuit was actually designed to work with RF and LO frequencies from 200MHz-400MHz range for the specific VCO used. The LO input displays low insertion loss at the designed frequencies, showing an S11 from 170 MHz to 300 MHz both with and without the addition of the wire.

4.2.5 Results Analysis

This brings us to stress the three key challenges in realizing an advanced performance system using inkjet printing technology. These challenges are related to the combi-

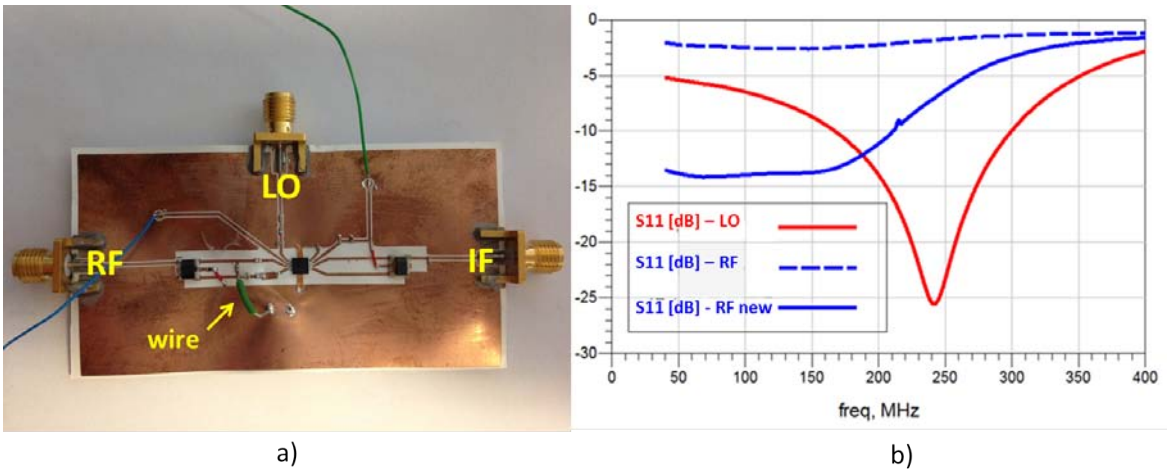

Fig. 4.16 Improvement in insertion loss (dotted blue curve to solid blue curve) upon addition of wire.

nation of the fabrication technology with the design process. The first challenge was related to the use of *low cost* materials, specifically the degraded quality of electrical contacts made with the solder paste material and copper film. Such a challenge is expected when working with new substrate materials and determines the best bonding material to use with them. Poor contacts caused a poor DC bias of the mixer circuit. This caused problems with the RF signal, particularly the S-parameters where S11 was observed to be too high. Even for a medium sized system, small variations in contact quality propagated across the board, degrading the overall quality of the circuit performance. The second challenge was to maintain a highly accurate *temperature control* with new materials needed to manage the trade-off between establishing good bonding contacts or leaving incomplete contacts, even with good paste. It was demonstrated in both the manual assembly, and heat controlled assembly that high temperatures helped to improve the connections quality but led to quick deterioration and damage. Even in the heat controlled oven, damage or complete destruction of the PET board was observed in the earlier prototypes. Using lower temperatures, however, resulted in poor contact quality and as mentioned previously, risked poor DC biasing. The temperature threshold is defined between the lower limit of being hot enough for the paste to reflow and establish good contacts and the upper limit of not approaching the thermal limit of sensitive components. The $Bi_{58}Sn_{42}$ Eutectic is at 138C while the component thermal limit is at 126C (Figure 4.17). This means the time spent allowing the paste to flow must be as short as possible in order to avoid damaging the IC. In addition, the glass transition temperature of the Polyethylene

terephthalate (PET) substrate is only 70C, so the substrate is suceptable to warping or deformation even in the low heating stages.

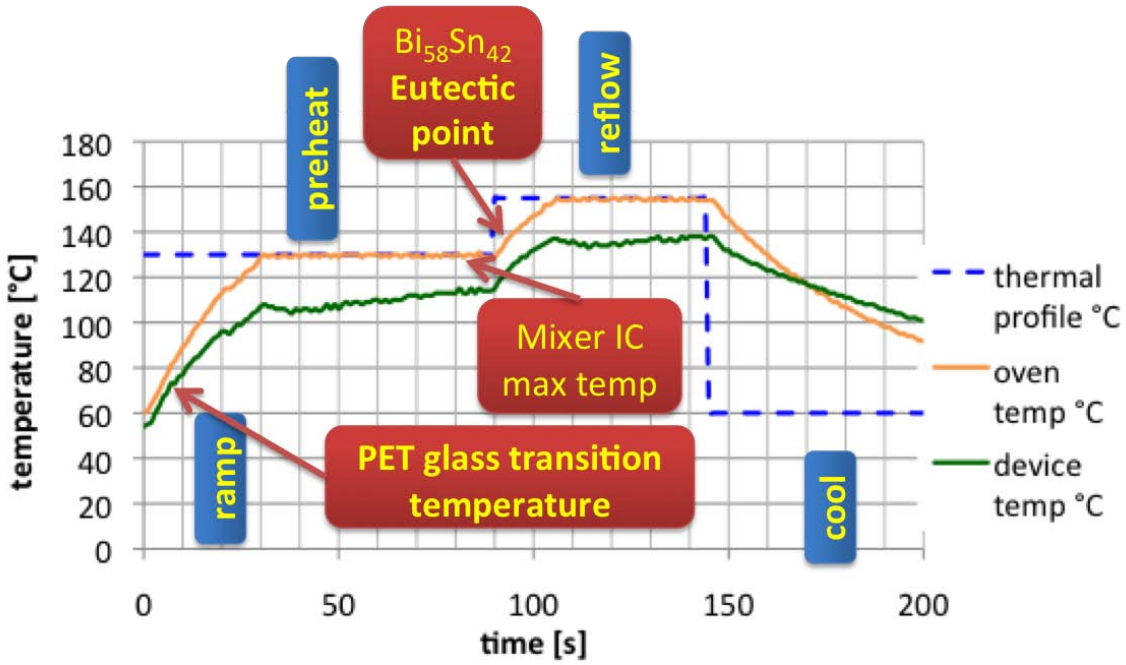

Fig. 4.17 Thermal profile settings, oven temperature, and device temperature used.

Finally, when implementing the radar system in a new fabrication technology, such as inkjet printing, electrical design issues arise, even when using a simplified architecture. In the case of of implementation in coplanar waveguide configurations, unexpected parasitic modes can arise within discontinuities and T-junctions [75]. Mode leakage can be a complex phenomena that can be easily overlooked in design and simulations and is often caught experimentally. This can be solved using ground straps (or ground bridges) at various locations along the CPW to shunt out the parasitic modes and avoid energy leakage. In this case, the simplest solution was to add a wire from the CPW ground to the signal line as seen in Figure 4.18. In future designs, or larger designs, the copper tape ground can be added for the easy insertion of bridges.

In the future, flexible electronics using inkjet printing technology should demonstrate advanced performance operation for state of the art rollable systems. This thesis represents the first time an attempt has been made to apply this technology to a radar system. Integrating off-the-shelf components with this technology will provide a head start in developing optimal designs and assembly techniques while taking advantage of state-of-the-art performance even in rollable or bent conditions. Robustness and rollable performance will continue to improve as the flexible electronics integration

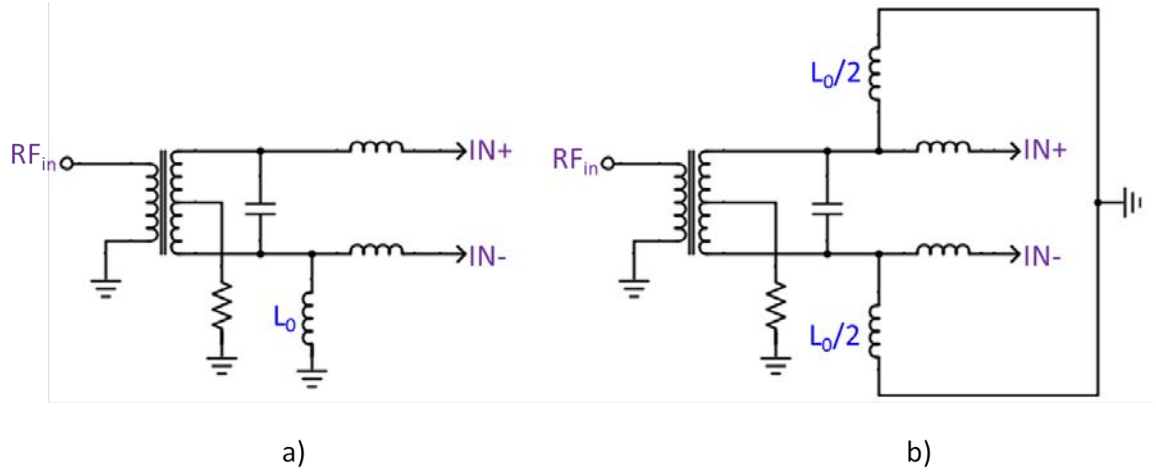

Fig. 4.18 Addition of inductance to remove the CPW parasitic mode.

level increases.

4.3 Antennas

Antennas for GPR applications require a high directivity and front to back ratio (to ensure maximum penetration into the ground with minimum backlobe radiation) and wideband impedance matching (particularly in the presence of the ground surface). The use of spatial or polarization diversity is beneficial for transmit/receive isolation. Monopole, dipole, wideband and frequency independent antennas often used in ground penetrating radar include cone, disc, bow-tie, tapered slot, horn and spiral antennas as listed in Table **??** [50].

Examples of GPR antennas from [50]					
Geometry	**Technology**	**Radiation**	**Polarization**	**G (500MHz)**	**G (1 GHz)**
cone	3D + ground	omni-dir	linear	1.6 dBi	3.2 dBi
disc	planar	omni-dir	linear	1.4 dBi	5.1 dBi
bow-tie	planar	bi-dir	linear	3.8 dBi	3.3 dBi
vivaldi	planar	dir	linear	3.0 dBi	5.8 dBi
DRH	3D	dir	linear	6.6 dBi	10.3 dBi
spiral	planar	bi-dir	linear	1.7 dBi	3.9 dBi

Table 4.2 My caption

Several antenna designs are being investigated for the monolithic radar system. The bowtie array is a good candidate for detecting large planar targets in a limited

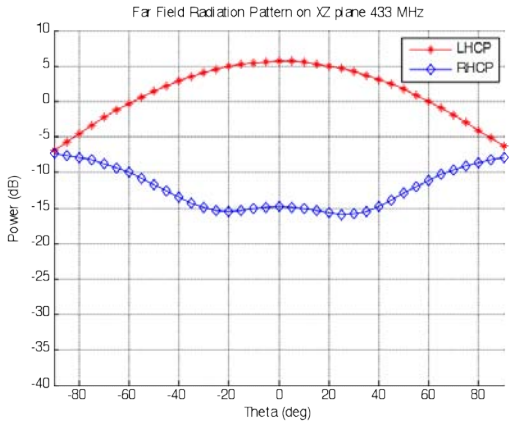

(a) XZ plane: 433 MHz

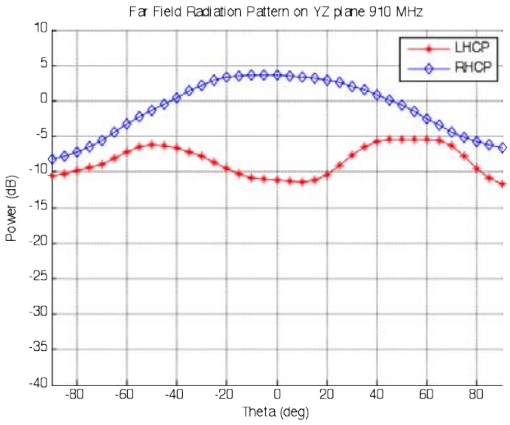

(b) XZ plane: 910 MHz

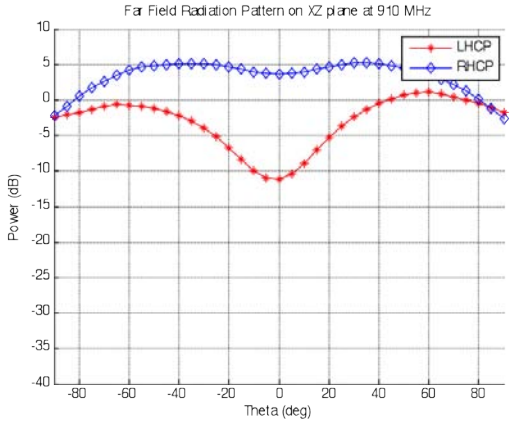

(c) XZ plane: 910 MHz

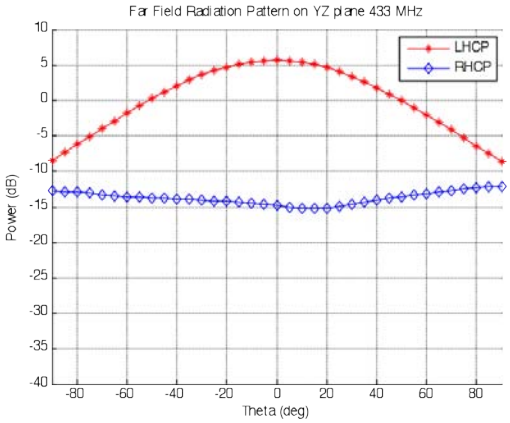

(d) YZ plane: 433 MHz

Fig. 4.19 Far field radiation pattern

frequency band and can be inkjet printed onto paper without difficulty. The equiangular spiral is another antenna with good performance over a large frequency range. Another potential design for a different mode of operation is a dual rhombic loop with a cross dipole in Fig. 8 [106]. It is circularly polarized making it ideal for smaller shallow more complex targets such as pipes that have depolarizing effects.

As stated previously, the antenna structure will occupy most of the space of the system. If the antenna size exceeds the printer area then different parts of the antenna can be printed on different sheets and later assembled together. The final antenna structure can still be low profile and simply folded and unfolded into position for use.

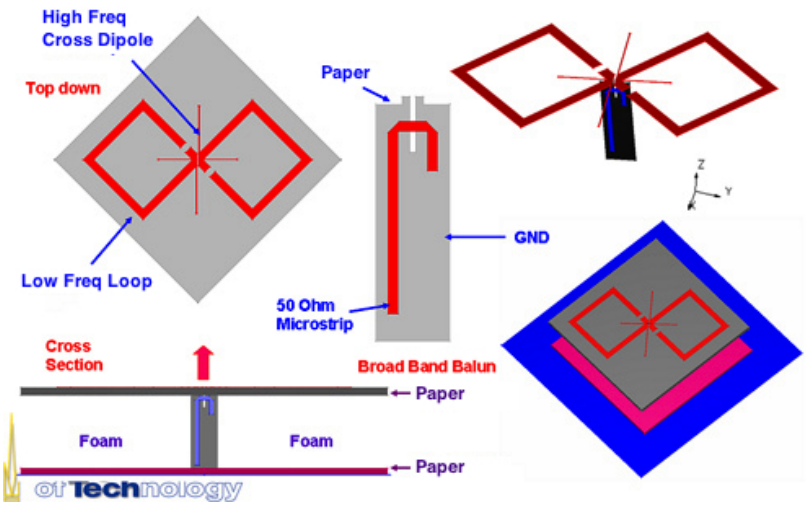

Fig. 4.20 Dual frequency CP rhombic Loop with crossed dipole.

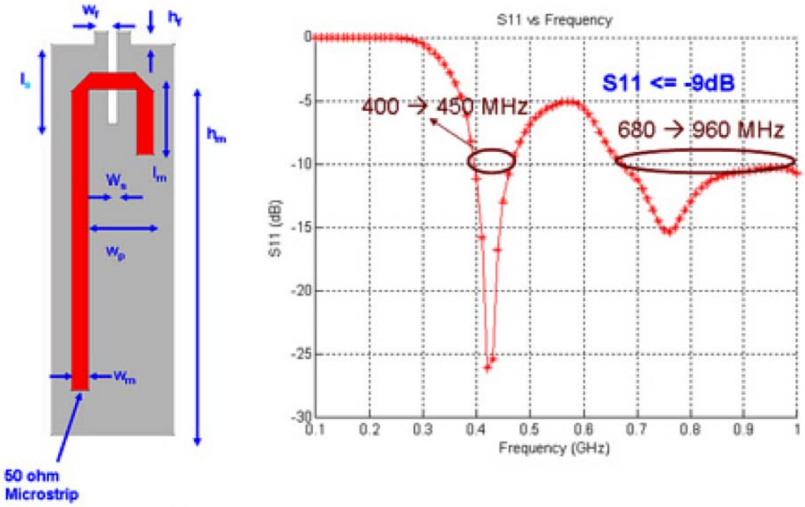

Fig. 4.21 Impedance matching.

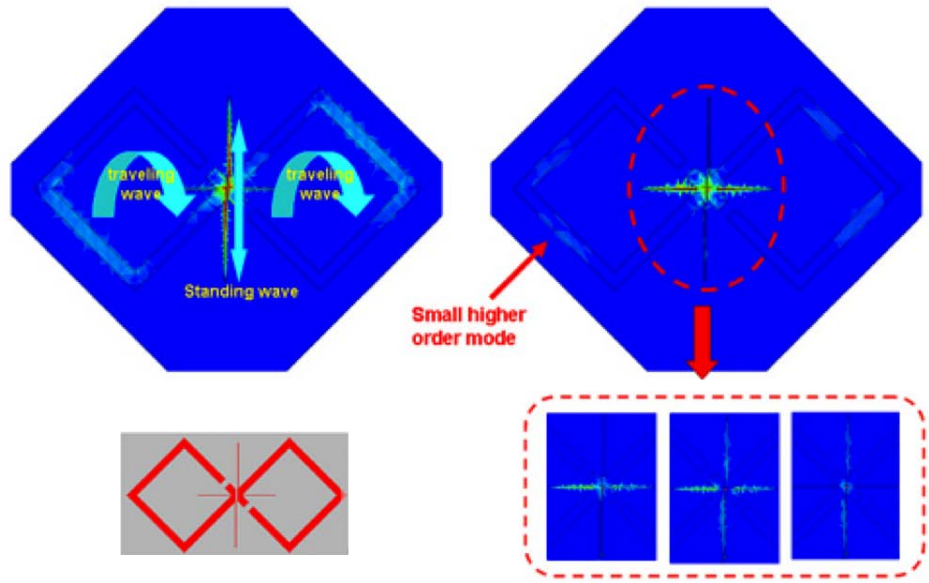

Fig. 4.22 Surface current magnitude.

4.3.1 Conclusions

It has been demonstrated that off the shelf components are very compatible with inkjet printed technology, allowing for the realization of hybrid rigid component/inkjet printed systems. Like other types of additive manufacturing technology, inkjet printing allows for the use of commercial CAD tools to realize complex geometries. Assembly of a circuit on printed copper film of flexible substrates can be performed manually using low temperature mounting techniques. For a complete user-friendly system, SMA connections can be added for easier testing. Both fundamental and advanced performance can be achieved using this technique and repeatability is improved by using a heat controlled mounting process that allows for the rapid but safe assembly of small components without damaging the inkjet printed films. The printed copper film demonstrated very good adhesion properties, allowing for easy flexing and rolling without cracking or delamination. The complete module displayed not only the ability to withstand mechanical rolling without damage but also a dynamic rolling-/bending-independent performance. These results verify the ability to achieve advanced performance operation capabilities with inkjet printing technology. The only limitation to the bending radius was the dimension of the largest IC, an issue that can be addressed utilizing smaller packages.

4.3.2 Recommendations

The initial design approach used for the simplified FMCW radar on new technology was good however the high insertion loss persisted for a large portion of the testing. It would have been interesting to verify the experimental findings in realistic simulations. The system displayed very good rollable performance. Further advancement towards realizing a truly rollable system would be to improve the flexibility of the soldered contacts, with less brittle material, so that the connections resist cracking when wrapped towards the minimum radius. Rather, the contacts should be strong enough to resist further rolling before even reaching the delamination point. The ability to print on an even wider variety of materials would open the doors for new features when it comes to robustness, environmentally friendliness, cost, biocompatibility, thermal management and the types of applications the device can be used for. This will require extensive research into modifying inkjet printing technology processes to be compatible with different materials, as is already being done. The adhesion performance of conductor film to different materials may vary greatly and each material will require different assembly process (bonding materials and temperatures used). The extensive fabrication challenges in developing a simple version of an FMCW radar stress the importance of developing the most efficient assembly method for each new material used, especially for large designs where the quality can vary greatly across different components. It has been demonstrated, that this new technology, in the early stages, can be combined with conventional technology processes until better techniques are developed. For example conventional stenciling could also be used to apply the solder paste to the inkjet printed layout for more complex designs. Another element that would have been interesting in this work, is the handling of the crossover connections which were realized with a wire. If using the silver nanoparticle inkjet printing method, the alignment capabilities could be used to reprinting a second layer over a protective coating for simple multilayer designs. As a conclusion, several key issues have been addressed in achieving advanced performance operation of a full system realized using inkjet printing.

References

[1] a.G. Stove (1992). Linear FMCW radar techniques. *IEE Proceedings F Radar and Signal Processing*, 139(5):343.

[2] Ahn, J.-H. and Je, J. H. (2012). Stretchable electronics: materials, architectures and integrations. *Journal of Physics D: Applied Physics*, 45(10):103001.

[3] Annan, A. (1992). Ground penetrating radar workshop notes. *Sensors and Software Inc., Mississauga*, (September).

[4] Annan, A. (1996). Transmission dispersion and GPR. *Journal of Environmental and Engineering Geophysics*, pages 125–136.

[5] Annan, A. (2005). GPR methods for hydrogeological studies. *Hydrogeophysics*, pages 185–213.

[6] Annan, A. P. (2002). GPR — History , Trends , and Future Developments. *Subsurface Sensing Technologies and Applications*, 3(4):253–270.

[7] Arcone, S. a. (2002). Stratigraphic profiling with ground-penetrating radar in permafrost: A review of possible analogs for Mars. *Journal of Geophysical Research*, 107(E11):5108.

[8] Bano, M. (2006). Bano - Effects of the transition zone above a water table on the reflection of GPR waves - 2006 - Unknown.pdf. 33:1–5.

[9] Benedetto, J. (2009). Phase-coded waveforms and their design. *Signal Processing ...*, (January 2009):22–31.

[10] Bevan, M. J., Endres, A. L., Rudolph, D. L., and Parkin, G. (2003). The non-invasive characterization of pumping-induced dewatering using ground penetrating radar. *Journal of Hydrology*, 281(1-2):55–69.

[11] Bilotti, F., Toscano, A., and Vegni, L. (1999). Very fast design formulas for microwave nonhomogeneous media filters. *Microwave and Optical ...*, 22(3):218–221.

[12] Bristow, C., Augustinus, P., Wallis, I., Jol, H., and Rhodes, E. (2010). Investigation of the age and migration of reversing dunes in Antarctica using GPR and OSL, with implications for GPR on Mars. *Earth and Planetary Science Letters*, 289(1-2):30–42.

[13] Buchner, R., Barthel, J., and Stauber, J. (1999). The dielectric relaxation of water between 0 C and 35 C. *Chemical Physics Letters*, 2(June).

[14] Cai, L., Li, J., Luan, P., Dong, H., Zhao, D., Zhang, Q., Zhang, X., Tu, M., Zeng, Q., Zhou, W., and Xie, S. (2012). Highly Transparent and Conductive Stretchable Conductors Based on Hierarchical Reticulate Single-Walled Carbon Nanotube Architecture. *Advanced Functional Materials*, 22(24):5238–5244.

[15] Cassidy, N. J. (2007). Evaluating LNAPL contamination using GPR signal attenuation analysis and dielectric property measurements: practical implications for hydrological studies. *Journal of contaminant hydrology*, 94(1-2):49–75.

[16] CENELEC (2009a). CENELEC GUIDE 24 - Electromagnetic Compatibility (EMC) Standardization for Product Committees concerned with apparatus.

[17] CENELEC (2009b). CENELEC GUIDE 25 - Guide on the user of standards for the implementation of the EMC Directive to apparatus.

[18] CENELEC (2014a). Cenelec guides @ONLINE. http://www.cenelec.eu/membersandexperts/referencematerial/cenelecguides.html.

[19] CENELEC (2014b). Electromagnetic compatibility (emc) @ONLINE. http://www.cenelec.eu/aboutcenelec/whatwedo/technologysectors/electromagneticcompatibility.html.

[20] Chalikakis, K., Plagnes, V., Guerin, R., Valois, R., and Bosch, F. P. (2011). Contribution of geophysical methods to karst-system exploration: an overview. *Hydrogeology Journal*, 19(6):1169–1180.

[21] Ciarletti, V., Corbel, C., Plettemeier, D., Ca\"\is, P., Clifford, S., and Hamran, S. (2011). WISDOM GPR Designed for Shallow and High-Resolution Sounding of the Martian Subsurface. *Proceedings of the IEEE*, 99(99):1–13.

[circuits] circuits, S. stretchable circuits.

[23] Clement, W. P. and Knoll, M. D. (2006). Traveltime inversion of vertical radar profiles. *Geophysics*, 71(3):K67.

[Daniels] Daniels, D., editor. *Ground Penetrating Radar-IET Radar, Sonar, Navigation and Avionics Series 15*. Institution of Engineering and Technology, 2nd edition.

[25] Daniels, J., Allred, B., and Binley, A. (2005). Hydrogeophysical case studies in the vadose zone. *Hydrogeophysics*, pages 413–440.

[26] Davis, J. L. and Annan, a. P. (1989). Ground-Penetrating Radar for High-Resolution Mapping of Soil and Rock Stratigraphy1. *Geophysical Prospecting*, 37(5):531–551.

[27] Deng, R. (1999). FM-CW radar performance in a lossy layered medium. *Journal of Applied Geophysics*, 42(1):23–33.

[28] des radiocommunications de l'UIT, L. (1995). *COURBES DE PROPAGATION EN ONDES MÉTRIQUES ET DÉCIMÉTRIQUES DANS LA GAMME DES FRÉQUENCES COMPRISES ENTRE 30 ET 1 000 MHz*.

[29] des radiocommunications de l'UIT, L. (2000). CARACTÉRISTIQUES ÉLECTRIQUES DU SOL. 1:10–14.

[30] Doolittle, J. (1995). Use of soil information to determine application of ground penetrating radar. *Journal of applied geophysics*, 33(1-3):101–108.

[31] DOOLITTLE, J., JENKINSON, B., HOPKINS, D., ULMER, M., and TUTTLE, W. (2006). Hydropedological investigations with ground-penetrating radar (GPR): Estimating water-table depths and local ground-water flow pattern in areas of coarse-textured soils. *Geoderma*, 131(3-4):317–329.

[32] Dukhan, M., Al-fares, W., Bakalowicz, M., and Gue, R. (2002). Analysis of the karst aquifer structure of the Lamalou area ´ rault , France) with ground penetrating radar (He. *Journal of Applied Geophysics*, 51:97–106.

[33] Elkhetali, S. I. (2006). Detection of Groundwater by Ground Penetrating Radar. *PIERS Online*, 2(3):251–255.

[34] ETSI (2009). STSI EG 202 730 - Electromagnetic compatibility and Radio spectrum Matters (ERM); Code of practice in respect to the control, use and application of Ground Probing Radar (GPR) and Wall Probing Radar (WPR) systems and equipment.

[35] Ezzy, T. R., Cox, M. E., O'Rourke, A. J., and Huftile, G. J. (2006). Groundwater flow modelling within a coastal alluvial plain setting using a high-resolution hydrofacies approach; Bells Creek plain, Australia. *Hydrogeology Journal*, 14(5):675–688.

[36] Francese, R., Mazzarini, F., Bistacchi, A., Morelli, G., Pasquarè, G., Praticelli, N., Robain, H., Wardell, N., and Zaja, A. (2009). A structural and geophysical approach to the study of fractured aquifers in the Scansano-Magliano in Toscana Ridge, southern Tuscany, Italy. *Hydrogeology Journal*, 17(5):1233–1246.

[37] Genderen, P. V. (2003). Multi-Waveform SFCW radar. *33rd European Microwave Conference, 2003*, pages 849–852.

[38] Genderen, P. V. and Hakkaart, P. (2001). A multi frequency radar for detecting landmines: Design aspects and electrical performance. *Microwave*, pages 1–4.

[39] GeoPotential (2014). Ground penetrating radar surveys @ONLINE.

[40] Greaves, R. J., Lesmes, D. P., Lee, J. M., and Toksoz, M. N. (1996). Velocity variations and water content estimated from multi-offset, ground-penetrating radar. *Geophysics*, 61(3):683–695.

[41] Griffiths, H. and McAslan, A. (2008). Low Frequency Radar for Buried Target Detection. *Unexploded Ordnance Detection and Mitigation*, page 125.

[42] Grimm, R. E., Heggy, E., Clifford, S., Dinwiddie, C., McGinnis, R., and Farrell, D. (2006). Absorption and scattering in ground-penetrating radar: Analysis of the Bishop Tuff. *Journal of Geophysical Research*, 111(E6):1–15.

[43] Hamran, S. (2009). Radar performance of ultra wideband waveforms. *Radar Technology*, (December):1–18.

[44] Hamran, S. and Erlingsson, B. (1998). Estimate of the subglacier dielectric constant of an ice shelf using a ground-penetrating step-frequency radar. *and Remote Sensing,*, 36(2):518–525.

[45] Hamran, S., Gjessing, D. T., Hjelmstad, J., and Aarholt, E. (1995). Ground penetrating synthetic pulse radar: dynamic range and modes of operation. *International Journal of Rock Mechanics and Mining Science & Geomechanics Abstracts*, 32(8):7–14.

[46] Hamran, S.-E., Berger, T., Hanssen, L., Oyan, M., Ciarletti, V., Corbel, C., and Plettemeier, D. (2007). A prototype for the WISDOM GPR on the ExoMars mission. *2007 4th International Workshop on, Advanced Ground Penetrating Radar*, pages 252–255.

[47] HARARI, Z. (1996). Ground-penetrating radar (GPR) for imaging stratigraphic features and groundwater in sand dunes. *Journal of Applied Geophysics*, 36(1):43–52.

[48] Harper, J. T. and Bradford, J. H. (2003). Snow stratigraphy over a uniform depositional surface: spatial variability and measurement tools. *Cold Regions Science and Technology*, 37(3):289–298.

[Harry M. Jol] Harry M. Jol. *Ground Penetrating Radar: Theory and Applications*. Elsevier, Amsterdam.

[50] Hertl, I. and Strycek, M. (2007). UWB antennas for ground penetrating radar application. *Applied Electromagnetics and ...*, pages 0–3.

[51] Holt, B., Kanagaratnam, P., Gogineni, S., Ramasami, V., Mahoney, A., and Lytle, V. (2008). Sea ice thickness measurements by ultrawideband penetrating radar: First results. *Cold Regions Science and Technology*, 55(1):33–46.

[52] HUISMAN, J., SNEPVANGERS, J., BOUTEN, W., and HEUVELINK, G. (2002). Mapping spatial variation in surface soil water content: comparison of ground-penetrating radar and time domain reflectometry. *Journal of Hydrology*, 269(3-4):194–207.

[53] Huisman, J. a., Hubbard, S. S., Redman, J. D., and Annan, a. P. (2003). Measuring Soil Water Content with Ground Penetrating Radar: A Review. *Vadose Zone Journal*, 2(4):476–491.

[54] III, H. N., Samueli, H., and Kim, B. (1988). The optimization of direct digital frequency synthesizer performance in the presence of finite word length effects. *Frequency Control ...*, pages 357–363.

[55] Jankiraman, M., Wessels, B., and van Genderen, P. (2000). Pandora multifrequency FMCW/SFCW radar. *Radar Conference,*, 0.

[56] Kester, W. (2005a). MT-001: Taking the Mystery out of the Infamous Formula," SNR= 6.02 N+ 1.76 dB," and Why You Should Care. *REV. 0*, pages 1–7.

[57] Kester, W. (2005b). MT-003: understand SINAD, ENOB, SNR, THD, THD+ N, and SFDR, so you don't get lost in the noise floor. *http.//www, analog. com/en/content/0*, MT-003:2–9.

[58] Kester, W. (2008). ADC Noise Figure An Often Misunderstaood and Misinterpreted Specification. *Analog Devices Application Note*, pages 1–9.

[59] Koh, G., Lever, J., Arcone, S., Marshall, H., and Ray, L. (2010). Autonomous FMCW radar survey of Antarctic shear zone. In *Ground Penetrating Radar (GPR), 2010 13th International Conference on*, pages 1–5. IEEE.

[60] Komarov, I. V. and Smolskiy, S. M. (2003). *Fundamentals of Short-Range FM Radar*. Artech House Publishers.

[61] Kroupa, V. (1993). Discrete spurious signals and background noise in direct frequency synthesizers. *Frequency Control Symposium, 1993. 47th., ...*, (2).

[62] Kroupa, V. (1999). Phase and amplitude disturbances in direct digital frequency synthesizers. *Ultrasonics, Ferroelectrics and Frequency Control, ...*, 46(3):481–486.

[63] Kroupa, V. and Stursa, J. (2001). Direct digital frequency synthesizers with the Σ-Δ arrangement in the PLL systems. *Frequency Control ....*

[64] Kroupa, V. F., Cizek, V., Stursa, J., and Svandova, H. (2000). Spurious signals in direct digital frequency synthesizers due to the phase truncation. *IEEE transactions on ultrasonics, ferroelectrics, and frequency control*, 47(5):1166–72.

[65] Kruesi, C. (2009). Design and development of a novel 3-D cubic antenna for wireless sensor networks (WSNs) and RFID applications. *Antennas and Propagation, ...*, 57(10):3293–3299.

[66] LANGHOFF, J., RASMUSSEN, K., and CHRISTENSEN, S. (2006). Quantification and regionalization of groundwater–surface water interaction along an alluvial stream. *Journal of Hydrology*, 320(3-4):342–358.

[67] Laskow, M., Gendler, M., Goldberg, I., Gvirtzman, H., and Frumkin, a. (2011). Deep confined karst detection, analysis and paleo-hydrology reconstruction at a basin-wide scale using new geophysical interpretation of borehole logs. *Journal of Hydrology*, 406(3-4):158–169.

[68] Lerner, L. (2014). Flexible, transparent thin film transistors raise hopes for flexible screens.

[69] Loher, T., Seckel, M., and Vieroth, R. (2009). Stretchable electronic systems: realization and applications. *Electronics ....*

[70] Longstaff, D., Noon, D., Leat, C., Stickley, G., and Cherniakov, M. (2003). GROUND PENETRATING RADAR.

[71] Maijala, P., Moore, J. C., Sven-Erik, H., Anja, P. A., and Anna, S. (1998). GPR INVESTIGATIONS OF GLACIERS AND SEA ICE IN THE SCANDINAVIAN ARCTIC. In *Proceedings International Conference on Ground-Penetrating Radar 7th*, pages 143–148, Lawrence, Kansas.

[72] Marshall, H. and Koh, G. (2008). FMCW radars for snow research. *Cold Regions Science and Technology*, 52(2):118–131.

[73] McClymont, A. F., Roy, J. W., Hayashi, M., Bentley, L. R., Maurer, H., and Langston, G. (2011). Investigating groundwater flow paths within proglacial moraine using multiple geophysical methods. *Journal of Hydrology*, 399(1-2):57–69.

[74] METJE, N., ATKINS, P., BRENNAN, M., CHAPMAN, D., LIM, H., MACHELL, J., MUGGLETON, J., PENNOCK, S., RATCLIFFE, J., and REDFERN, M. (2007). Mapping the Underworld – State-of-the-art review. *Tunnelling and Underground Space Technology*, 22(5-6):568–586.

[75] Microwaves101 (2014). Coplanar waveguide @ONLINE. http://www.microwaves101.com/encyclopedias/327-coplanar-waveguide-microwave-encyclopedia-microwaves101-com.

[76] Mullarkey, B. (2008). The differences between pulse radars and FMCW ones. *Retrieved Dec.*

[77] NAKASHIMA, Y., ZHOU, H., and SATO, M. (2001). Estimation of groundwater level by GPR in an area with multiple ambiguous reflections. *Journal of Applied Geophysics*, 47(3-4):241–249.

[78] National Telecommunications and Information Administration (2008). ANNEX K - Technical Standards for Federal " Non-Licensed " Devices. Technical report.

[79] Neal, A. (2004). Ground-penetrating radar and its use in sedimentology: principles, problems and progress. *Earth-Science Reviews*, 66(3-4):261–330.

[80] Nicholas, H. and Samueli, H. (1987). An analysis of the output spectrum of direct digital frequency synthesizers in the presence of phase-accumulator truncation. *... Annual Symposium on Frequency ....*

[81] Nikolaou, S. and Marcaccioli, L. (2005). Conformal double exponentially tapered slot antennas (DETSA) for UWB communications systems' front-ends. *Ultra-Wideband, ...*

[82] Noon, D. and Longstaff, D. (1994). Correction of I/Q errors in homodyne step frequency radar refocuses range profiles. *Acoustics, Speech, and*, pages 369–372.

[83] Noon, D., Stickley, G., and Longstaff, D. (1998). A frequency-independent characterisation of GPR penetration and resolution performance. *Journal of Applied Geophysics.*

[84] Owen, R. and Dahlin, T. (2010). Inherited drainage - paleochannels and preferential groundwater flow. *Hydrogeology Journal*, 18(4):893–903.

[85] Oyan, M. and Hamran, S. (2012). Ultrawideband gated step frequency ground-penetrating radar. *... and Remote Sensing ...*, 50(1):212–220.

[86] O'Driscoll, M., Johnson, P., and Mallinson, D. (2010). Geological controls and effects of floodplain asymmetry on river–groundwater interactions in the southeastern Coastal Plain, USA. *Hydrogeology Journal*, 18(5):1265–1279.

[87] Parviz, B. (2009). For your eye only. *Spectrum, IEEE*, (september 2009):36–41.

[88] PEREZGRACIA, V., GONZALEZDRIGO, R., and DICAPUA, D. (2008). Horizontal resolution in a non-destructive shallow GPR survey: An experimental evaluation. *NDT & E International*, 41(8):611–620.

[89] Piper, S. (1993). Receiver frequency resolution for range resolution in homodyne FMCW radar. *..., 1993.'Commercial Applications and Dual-Use ...*, pages 0–4.

[90] Piper, S. (1995). Homodyne FMCW radar range resolution effects with sinusoidal nonlinearities in the frequency sweep. *Radar Conference, 1995., Record of the IEEE 1995 ...*, 0:563–567.

[91] Plumb, R., Noon, D., and Longstaff, I. (1998). A waveform-range performance diagram for ground-penetrating radar. *Journal of applied*, pages 117–126.

[92] Porsani, J., Filho, W., Elis, V., Shimeles, F., Dourado, J., and Moura, H. (2004). The use of GPR and VES in delineating a contamination plume in a landfill site: a case study in SE Brazil. *Journal of Applied Geophysics*, 55(3-4):199–209.

[93] Reynolds, J. M. (2011). *An Introduction to Applied and Environmental Geophysics*. John Wiley and Sons.

[94] RFSafetySolutions (2014). Fcc regulations @ONLINE. http://www.rfsafetysolutions.com/RF%20Radiation%20Pages/FCC_Regulations.html.

[95] Sachs, J. (2010). Ultra-wideband sensing: The road to new radar applications. *Radar Symposium (IRS), 2010 11th International*.

[96] Sailhac, P., Bano, M., Behaegel, M., Girard, J.-F., Para, E. F., Ledo, J., Marquis, G., Matthey, P.-D., and Ortega-Ramírez, J. (2009). Characterizing the vadose zone and a perched aquifer near the Vosges ridge at the La Soutte experimental site, Obernai, France. *Comptes Rendus Geoscience*, 341(10-11):818–830.

[97] Scott, M., Arnold, J., and Gibson, D. (2010). Step Frequency Ground Penetrating Radar Characterization and Federal Evaluation Tests. (october).

[98] Shiklomanov, I. (1993). Water in Crisis: A Guide to the World's Fresh Water Resources. In Gleick, P. H., editor, *World fresh water resources*. Oxford University Press, New York.

[99] Son, D., Lee, J., Qiao, S., Ghaffari, R., Kim, J., Lee, J. E., Song, C., Kim, S. J., Lee, D. J., Jun, S. W., Yang, S., Park, M., Shin, J., Do, K., Lee, M., Kang, K., Hwang, C. S., Lu, N., Hyeon, T., and Kim, D.-H. (2014). Multifunctional wearable devices for diagnosis and therapy of movement disorders. *Nature nanotechnology*, 9(5):397–404.

[100] Stickley, G. and Noon, D. (1997). Preliminary field results of an ultra-wideband (10-620 MHz) stepped-frequency ground penetrating radar. *and Remote Sensing*, pages 1282–1284.

[101] Stickley, G., Noon, D., Cherniakov, M., and Longstaff, I. (2000). Gated stepped-frequency ground penetrating radar. *Journal of Applied Geophysics*, 43(2-4):259–269.

[102] Stotler, R. L., Frape, S. K., Ruskeeniemi, T., Ahonen, L., Onstott, T. C., and Hobbs, M. Y. (2009). Hydrogeochemistry of groundwaters in and below the base of thick permafrost at Lupin, Nunavut, Canada. *Journal of Hydrology*, 373(1-2):80–95.

[103] Sultan, M., Wagdy, A., Manocha, N., Sauck, W., Gelil, K. A., Youssef, A., Becker, R., Milewski, A., El Alfy, Z., and Jones, C. (2008). An integrated approach for identifying aquifers in transcurrent fault systems: The Najd shear system of the Arabian Nubian shield. *Journal of Hydrology*, 349(3-4):475–488.

[104] Sun, B., Long, Y.-Z., Chen, Z.-J., Liu, S.-L., Zhang, H.-D., Zhang, J.-C., and Han, W.-P. (2014). Recent advances in flexible and stretchable electronic devices via electrospinning. *Journal of Materials Chemistry C*, 2(7):1209.

[105] Terlep, D. (2002). How Quantization and Thermal Noise Determine an ADC's Effective Noise Figure. pages 1–5.

[106] Traille, A. and Tentzeris, M. M. (2008). Novel Dual-Band Circular-Polarization Antennas for Universal RFID Readers and Cognitive Radio Applications. In *Proceedings of the 2008 URSI Meeting*.

[107] TURESSON, A. (2006). Water content and porosity estimated from ground-penetrating radar and resistivity. *Journal of Applied Geophysics*, 58(2):99–111.

[108] United States Environmental Protection Agency (2000). Innovations in Site Geophysical Investigation at Hazardous Waste Sites. (August).

[109] van Genderen, P. (2001). The effect of phase noise in a stepped frequency continuous wave ground penetrating radar. *2001 CIE International Conference on Radar Proceedings (Cat No.01TH8559)*, pages 581–584.

[110] Wang, C., Hwang, D., Yu, Z., Takei, K., Park, J., Chen, T., Ma, B., and Javey, A. (2013). User-interactive electronic skin for instantaneous pressure visualization. *Nature materials*, 12(10):899–904.

[111] Wolf, A. (1937). The reflection of elastic waves from transition layers of variable velocity. *Geophysics*, pages 357–363.

[112] Xu, S., Zhang, Y., Cho, J., Lee, J., Huang, X., Jia, L., Fan, J. A., Su, Y., Su, J., Zhang, H., Cheng, H., Lu, B., Yu, C., Chuang, C., Kim, T.-i., Song, T., Shigeta, K., Kang, S., Dagdeviren, C., Petrov, I., Braun, P. V., Huang, Y., Paik, U., and Rogers, J. A. (2013). Stretchable batteries with self-similar serpentine interconnects and integrated wireless recharging systems. *Nat Commun*, 4:1543.

[113] Zhang, B., Dong, Q., Korman, C. E., Li, Z., and Zaghloul, M. E. (2013). Flexible packaging of solid-state integrated circuit chips with elastomeric microfluidics. *Scientific Reports*, 3:1–8.

[114] Zhu, X., He, X., Lu, G., Liu, Q., and Li, J. (2009). Ground Penetrating Radar Exploration for Ground Water and Contamination. *PIERS Proc*, pages 1316–1320.

Appendix A

Appendix A

A.1 Dwell time: t_d

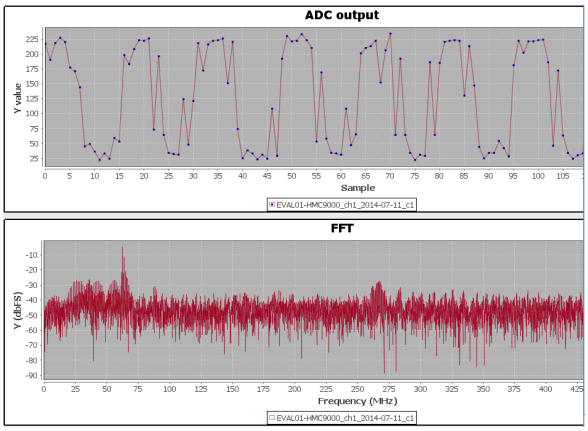

$B_{DDS} = 200\text{MHz}$, $t_d = 0.0082\mu s$

DDS Settings	
Sweep	**50MHz - 250MHz**
t_d	**0.0082**μs
Δf	1MHz
ADC Output (f_s = 1GHz)	
Signal	-4.72 dBFS
SNR	6.314 dBFS
SNDR	5.227 dBFS
ENOB	0.576 bit
SFDR	6.957 dBc (63.6 MHz)
HD2	NaN dBc (125 MHz)
HD3	-30.81 dBc (187 MHz)

DDS & ADC settings.

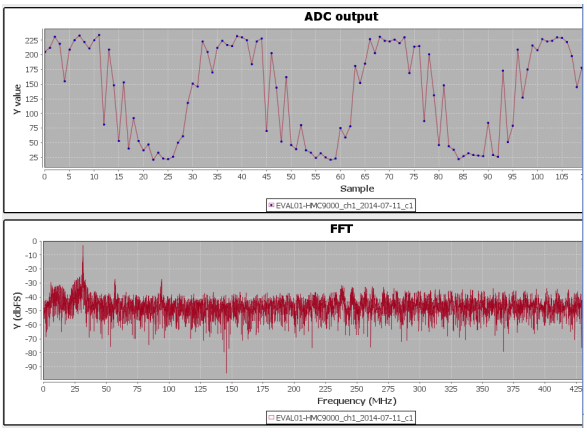

$B_{DDS} = 200\text{MHz}$, $t_d = 0.0163\mu s$

DDS Settings	
Sweep	**50MHz - 250MHz**
t_d	**0.0163**μs
Δf	1MHz
ADC Output (f_s = 1GHz)	
Signal	-3.30 dBFS
SNR	7.673 dBFS
SNDR	7.093 dBFS
ENOB	0.886 bit
SFDR	2.79 dBc (30.8 MHz)
HD2	NaN dBc (62.9 MHz)
HD3	7.41 dBc (94.3 MHz)

DDS & ADC settings.

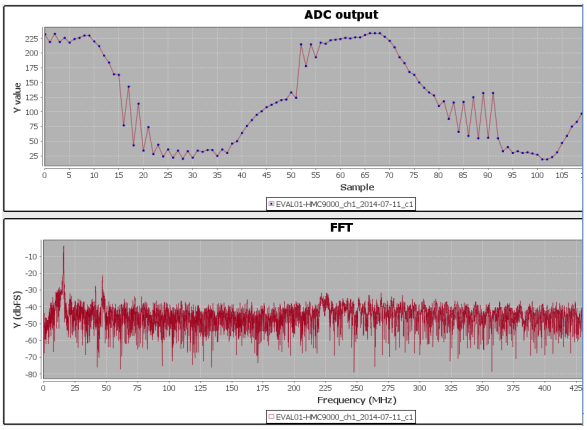

$B_{DDS} = 200\text{MHz}$, $t_d = 0.0327\mu s$

DDS Settings	
Sweep	**50MHz - 250MHz**
t_d	**0.0327**μs
Δf	1MHz
ADC Output (f_s = 1GHz)	
Signal	-3.85 dBFS
SNR	8.799 dBFS
SNDR	8.536 dBFS
ENOB	1.13 bit
SFDR	16.71 dBc (46.9 MHz)
HD2	-40.47 dBc (31.6 MHz)
HD3	-27.00 dBc (47.4 MHz)

DDS & ADC settings.

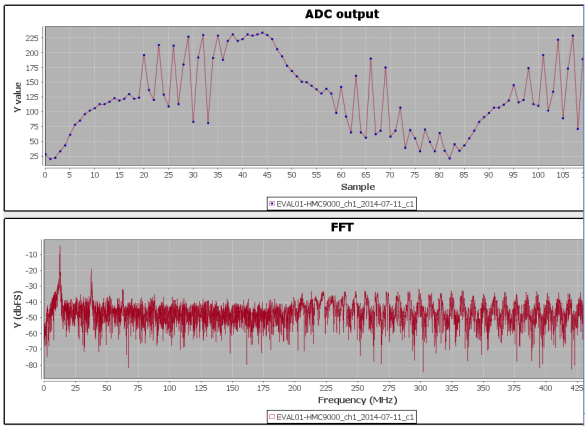

$B_{DDS} = 200\text{MHz}$, $t_d = 0.0408\mu s$

DDS Settings	
Sweep	**50MHz - 250MHz**
t_d	**0.0408**μs
Δf	1MHz
ADC Output (f_s = 1GHz)	
Signal	-4.45 dBFS
SNR	8.791 dBFS
SNDR	8.366 dBFS
ENOB	1.10 bit
SFDR	4.21 dBc (37.5 MHz)
HD2	5.08 dBc (25.3 MHz)
HD3	-3/8.84 dBc (37.9 MHz)

DDS & ADC settings.

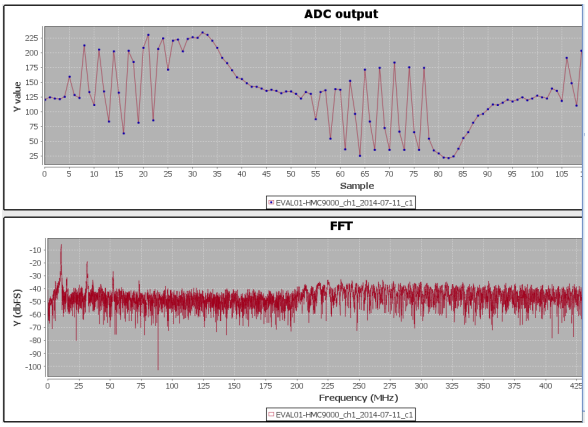

$B_{DDS} = 200\text{MHz}$, $t_d = 0.0490\mu s$

DDS Settings	
Sweep	**50MHz - 250MHz**
t_d	**0.0490μs**
Δf	1MHz
ADC Output (f_s = 1GHz)	
Signal	-5.88 dBFS
SNR	8.447 dBFS
SNDR	7.928 dBFS
ENOB	1.02 bit
SFDR	2.30 dBc (31.3 MHz)
HD2	NaN dBc (21.0 MHz)
HD3	3/8.18 dBc (31.5 MHz)

DDS & ADC settings.

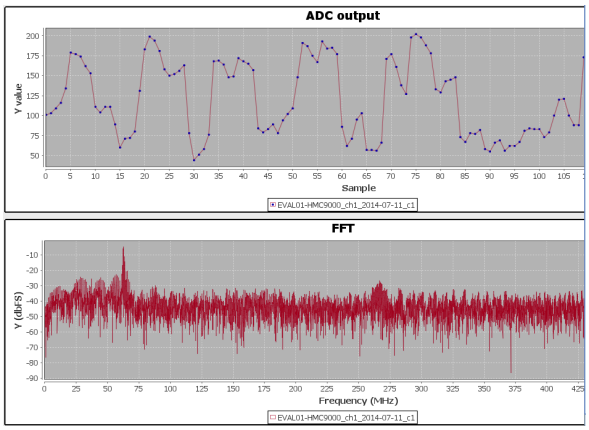

$B_{DDS} = 250\text{MHz}$, $t_d = 0.0082\mu s$

DDS Settings	
Sweep	**50MHz - 300MHz**
t_d	**0.0082μs**
Δf	1MHz
ADC Output (f_s = 1GHz)	
Signal	-4.95 dBFS
SNR	6.314 dBFS
SNDR	6.017 dBFS
ENOB	0.707 bit
SFDR	2.70 dBc (63.7 MHz)
HD2	9.61 dBc (125 MHz)
HD3	NaN dBc (188 MHz)

DDS & ADC settings.

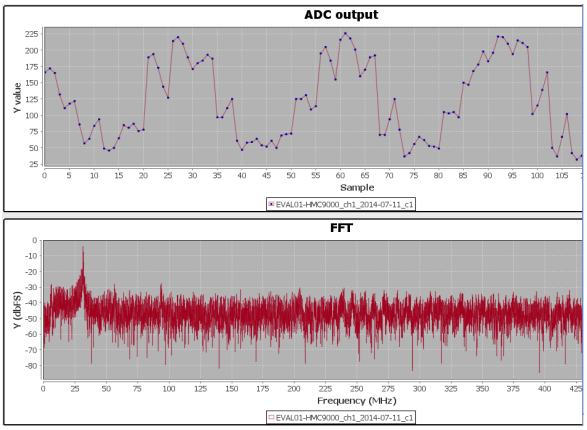

$B_{DDS} = 250\text{MHz}$, $t_d = 0.0163\mu s$

DDS Settings	
Sweep	**50MHz - 300MHz**
t_d	**0.0163μs**
Δf	1MHz
ADC Output (f_s = 1GHz)	
Signal	-3.95 dBFS
SNR	7.405 dBFS
SNDR	7.198 dBFS
ENOB	0.903 bit
SFDR	16.57 dBc (30 MHz)
HD2	NaN dBc (62.6 MHz)
HD3	-24.57 dBc (93.9 MHz)

DDS & ADC settings.

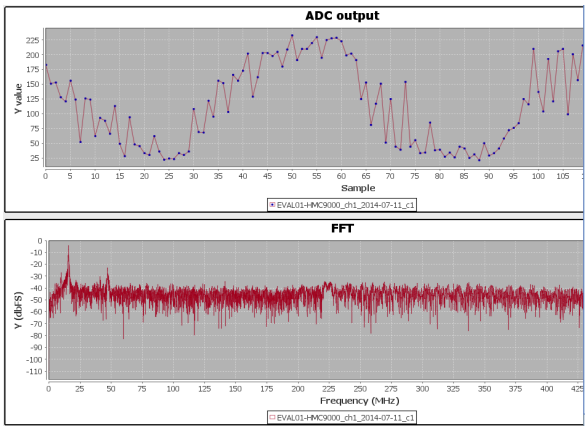

$B_{DDS} = 250\text{MHz}$, $t_d = 0.0327\mu s$

DDS Settings	
Sweep	**50MHz - 300MHz**
t_d	**0.0327μs**
Δf	1MHz
ADC Output (f_s = 1GHz)	
Signal	-4.10 dBFS
SNR	9.099 dBFS
SNDR	8.608 dBFS
ENOB	1.14 bit
SFDR	6.32 dBc (15.1 MHz)
HD2	9.15 dBc (31.4 MHz)
HD3	7.72 dBc (47.1 MHz)

DDS & ADC settings.

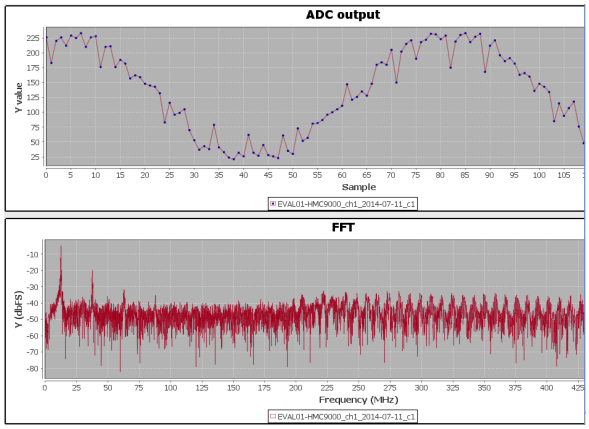

$B_{DDS} = 250\text{MHz}$, $t_d = 0.0408\mu s$

DDS Settings	
Sweep	**50MHz - 300MHz**
t_d	**0.0408μs**
Δf	1MHz
ADC Output (f_s = 1GHz)	
Signal	-4.88 dBFS
SNR	8.921 dBFS
SNDR	8.454 dBFS
ENOB	1.11 bit
SFDR	14.05 dBc (37.5 MHz)
HD2	NaN dBc (25.1 MHz)
HD3	-14.71 dBc (37.7 MHz)

DDS & ADC settings.

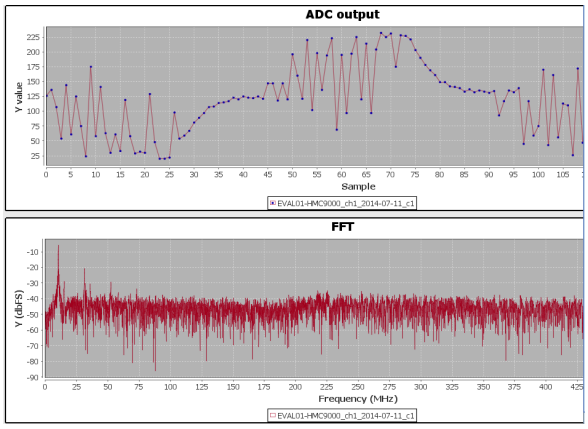

$B_{DDS} = 250\text{MHz}$, $t_d = 0.0490\mu s$

DDS Settings	
Sweep	**50MHz - 300MHz**
t_d	**0.0490μs**
Δf	1MHz
ADC Output (f_s = 1GHz)	
Signal	-5.83 dBFS
SNR	9.523 dBFS
SNDR	9.109 dBFS
ENOB	1.22 bit
SFDR	4.08 dBc (31.3 MHz)
HD2	5.06 dBc (21.0 MHz)
HD3	5.14 dBc (31.5 MHz)

DDS & ADC settings.

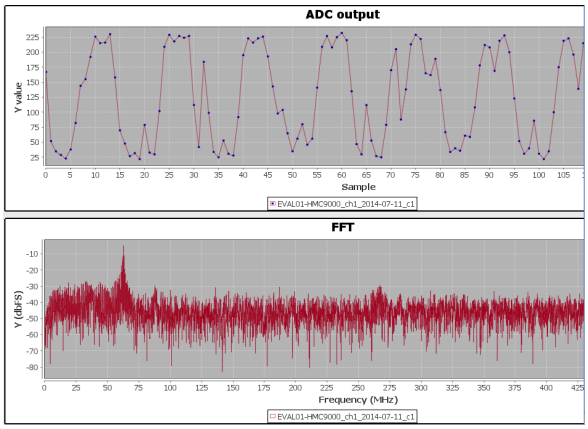

$B_{DDS} = 350\text{MHz}$, $t_d = 0.0082\mu s$

DDS Settings	
Sweep	**50MHz - 400MHz**
t_d	**0.0082**μs
Δf	1MHz
ADC Output (f_s = 1GHz)	
Signal	-4.93 dBFS
SNR	5.852 dBFS
SNDR	5.147 dBFS
ENOB	0.563 bit
SFDR	220 dBc (62.0 MHz)
HD2	NaN dBc (125 MHz)
HD3	NaN dBc (188 MHz)

DDS & ADC settings.

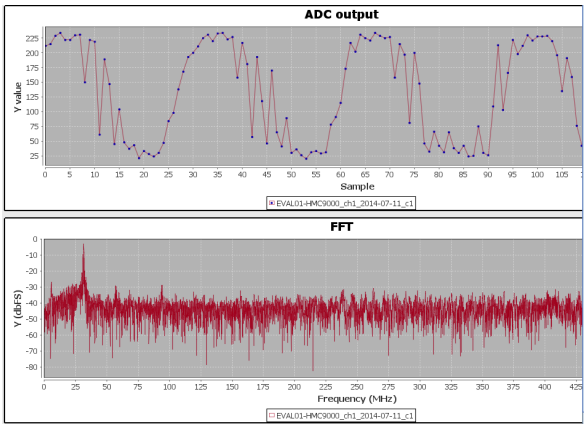

$B_{DDS} = 350\text{MHz}$, $t_d = 0.0163\mu s$

DDS Settings	
Sweep	**50MHz - 400MHz**
t_d	**0.0163**μs
Δf	1MHz
ADC Output (f_s = 1GHz)	
Signal	-3.13 dBFS
SNR	7.516 dBFS
SNDR	7.300 dBFS
ENOB	0.920 bit
SFDR	7.60 dBc (30.7 MHz)
HD2	NaN dBc (62.6 MHz)
HD3	5/6.88 dBc (93.9 MHz)

DDS & ADC settings.

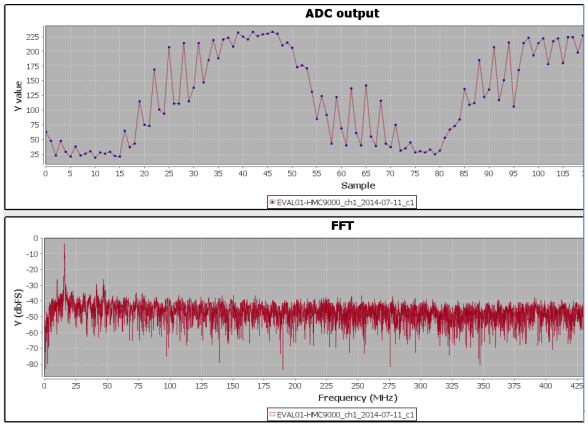

DDS Settings	
Sweep	**50MHz - 400MHz**
t_d	**0.0327μs**
Δf	1MHz
ADC Output (f_s = 1GHz)	
Signal	-3.74 dBFS
SNR	9.953 dBFS
SNDR	9.742 dBFS
ENOB	1.33 bit
SFDR	2.69 dBc (15.1 MHz)
HD2	4.23 dBc (31.4 MHz)
HD3	2.38 dBc (47.1 MHz)

$B_{DDS} = 350\text{MHz}$, $t_d = 0.0327\mu s$ DDS & ADC settings.

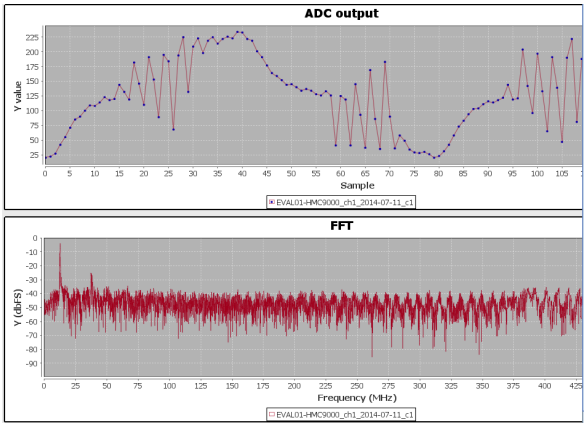

DDS Settings	
Sweep	**50MHz - 400MHz**
t_d	**0.0408μs**
Δf	1MHz
ADC Output (f_s = 1GHz)	
Signal	-4.34 dBFS
SNR	9.841 dBFS
SNDR	9.577 dBFS
ENOB	1.30 bit
SFDR	2.78 dBc (13.1 MHz)
HD2	NaN dBc (25.0 MHz)
HD3	9.11 dBc (37.5 MHz)

$B_{DDS} = 350\text{MHz}$, $t_d = 0.0408\mu s$ DDS & ADC settings.

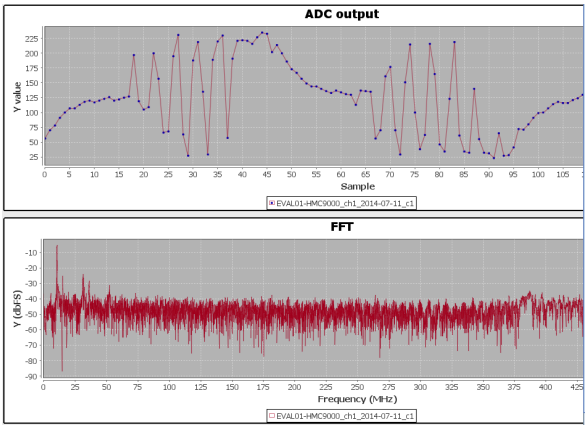

DDS Settings	
Sweep	**50MHz - 400MHz**
t_d	**0.0490μs**
Δf	1MHz
ADC Output (f_s = 1GHz)	
Signal	-5.29 dBFS
SNR	9.799 dBFS
SNDR	9.471 dBFS
ENOB	1.28 bit
SFDR	7.43 dBc (31.1 MHz)
HD2	NaN dBc (20.9 MHz)
HD3	5/6.83 dBc (31.3 MHz)

$B_{DDS} = 350\text{MHz}$, $t_d = 0.0490\mu s$ DDS & ADC settings.

A.2 Frequency stepsize: Δf

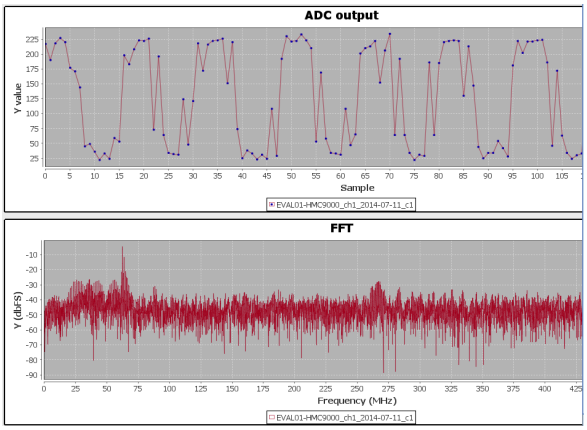

DDS Settings	
Sweep	**50MHz - 250MHz**
t_d	**0.0082μs**
Δf	**1MHz**
ADC Output (f_s = 1GHz)	
Signal	-4.72 dBFS
SNR	6.314 dBFS
SNDR	5.227 dBFS
ENOB	0.576 bit
SFDR	6.957 (63.6 MHz)
HD2	NaN dBc (125 MHz)
HD3	-30.81 dBc (187 MHz)

$t_d = 0.0082\mu s$, $\Delta f = 1$MHz

DDS & ADC settings.

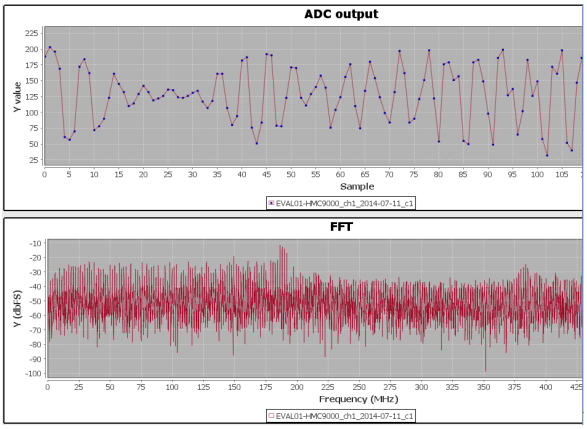

DDS Settings	
Sweep	**50MHz - 250MHz**
t_d	**0.0082μs**
Δf	**2MHz**
ADC Output (f_s = 1GHz)	
Signal	-11.5 dBFS
SNR	3.975 dBFS
SNDR	3.382 dBFS
ENOB	0.269 bit
SFDR	1.553 (188 MHz)
HD2	NaN dBc (373 MHz)
HD3	-26.60 dBc (441 MHz)

$t_d = 0.0082\mu s$, $\Delta f = 2$MHz

DDS & ADC settings.

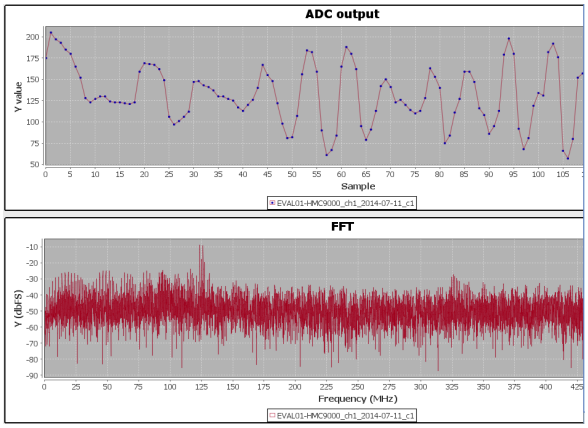

$t_d = 0.0082\mu s$, $\Delta f = 3$MHz

DDS Settings	
Sweep	**50MHz - 250MHz**
t_d	**0.0082μs**
Δf	**3MHz**
ADC Output (f_s = 1GHz)	
Signal	-8.71 dBFS
SNR	5.488 dBFS
SNDR	3.7771 dBFS
ENOB	0.334 bit
SFDR	069 (126 MHz)
HD2	NaN dBc (248 MHz)
HD3	NaN dBc (371 MHz)

DDS & ADC settings.

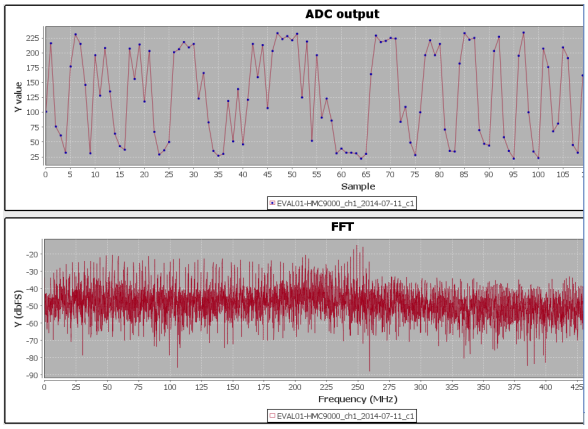

$t_d = 0.0082\mu s$, $\Delta f = 4$MHz

DDS Settings	
Sweep	**50MHz - 250MHz**
t_d	**0.0082μs**
Δf	**4MHz**
ADC Output (f_s = 1GHz)	
Signal	-14.8 dBFS
SNR	3.386 dBFS
SNDR	3.225 dBFS
ENOB	0.243 bit
SFDR	1.166 (254 MHz)
HD2	NaN dBc (498 MHz)
HD3	NaN dBc (253 MHz)

DDS & ADC settings.

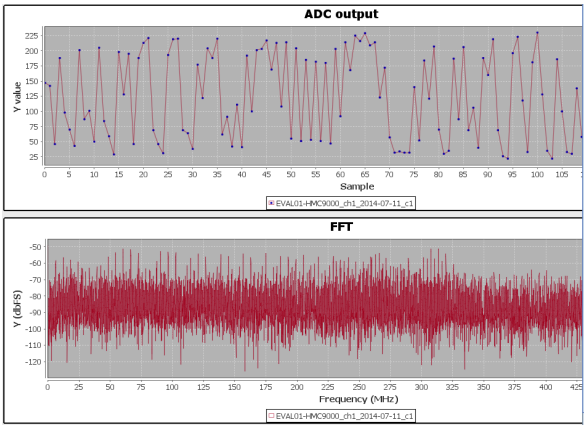

$t_d = 0.0082\mu s$, $\Delta f = 5$MHz

DDS Settings	
Sweep	**50MHz - 250MHz**
t_d	**0.0082μs**
Δf	**5MHz**
ADC Output (f_s = 1GHz)	
Signal	-49.0 dBFS
SNR	3.532 dBFS
SNDR	3.389 dBFS
ENOB	0.271 bit
SFDR	-31.23 (314 MHz)
HD2	NaN dBc (0,00 MHz)
HD3	NaN dBc (0,00 MHz)

DDS & ADC settings.

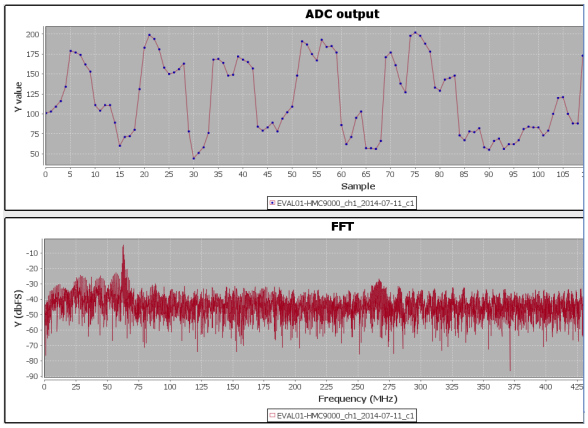

$t_d = 0.0082\mu s$, $\Delta f = 1$MHz

DDS Settings	
Sweep	**50MHz - 300MHz**
t_d	**0.0082μs**
Δf	**1MHz**
ADC Output (f_s = 1GHz)	
Signal	-4.95 dBFS
SNR	6.314 dBFS
SNDR	6.017 dBFS
ENOB	0.707 bit
SFDR	2.70 (63.7 MHz)
HD2	9.61 dBc (125 MHz)
HD3	NaN dBc (188 MHz)

DDS & ADC settings.

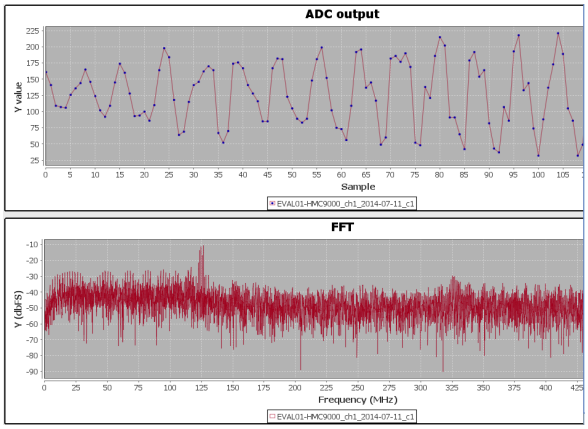

$t_d = 0.0082\mu s$, $\Delta f = 2$MHz

DDS Settings	
Sweep	**50MHz - 300MHz**
t_d	**0.0082μs**
Δf	**2MHz**
ADC Output (f_s = 1GHz)	
Signal	-10.6 dBFS
SNR	4.888 dBFS
SNDR	3.805 dBFS
ENOB	0.340 bit
SFDR	035 (125 MHz)
HD2	NaN dBc (253 MHz)
HD3	NaN dBc (380 MHz)

DDS & ADC settings.

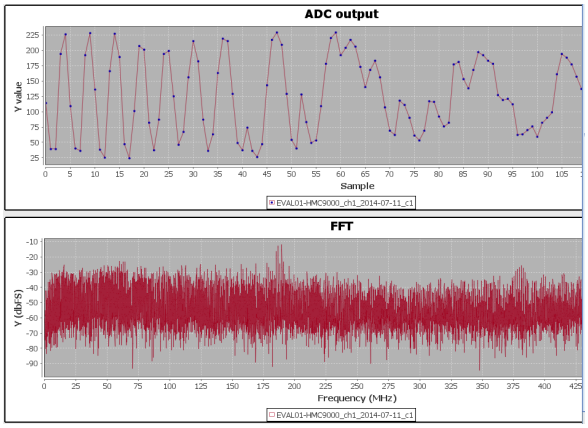

$t_d = 0.0082\mu s$, $\Delta f = 3$MHz

DDS Settings	
Sweep	**50MHz - 300MHz**
t_d	**0.0082μs**
Δf	**3MHz**
ADC Output (f_s = 1GHz)	
Signal	-12.0 dBFS
SNR	4.627 dBFS
SNDR	3.717 dBFS
ENOB	0.325 bit
SFDR	075 (187 MHz)
HD2	NaN dBc (379 MHz)
HD3	NaN dBc (431 MHz)

DDS & ADC settings.

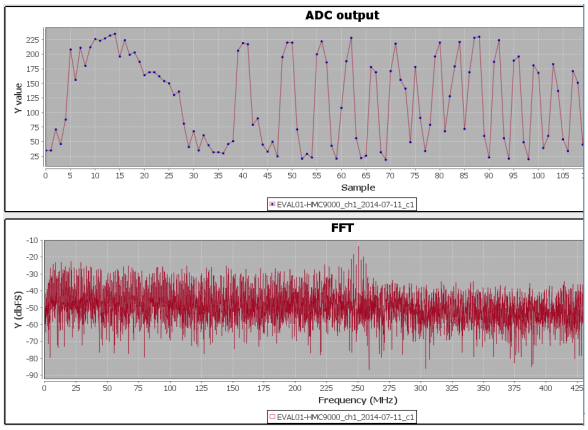

$t_d = 0.0082\mu s$, $\Delta f = 4$MHz

DDS Settings	
Sweep	**50MHz - 300MHz**
t_d	**0.0082μs**
Δf	**4MHz**
ADC Output (f_s = 1GHz)	
Signal	-13.7 dBFS
SNR	4.113 dBFS
SNDR	3.930 dBFS
ENOB	0.360 bit
SFDR	4.844 (247 MHz)
HD2	NaN dBc (433 MHz)
HD3	-13.16 dBc (249 MHz)

DDS & ADC settings.

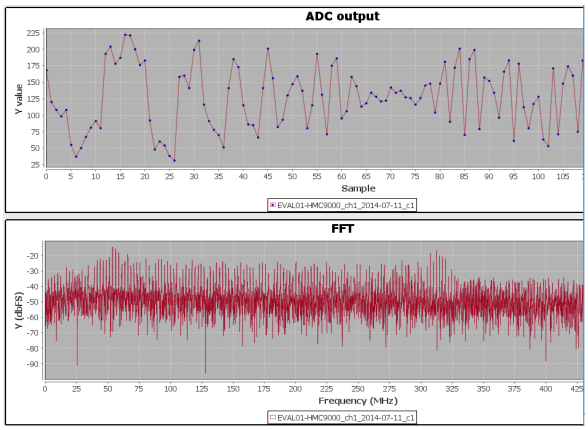

$t_d = 0.0082\mu s$, $\Delta f = 5$MHz

DDS Settings	
Sweep	**50MHz - 300MHz**
t_d	**0.0082μs**
Δf	**5MHz**
ADC Output (f_s = 1GHz)	
Signal	-14.6 dBFS
SNR	3.767 dBFS
SNDR	3.642 dBFS
ENOB	0.313 bit
SFDR	2.567 (56.0 MHz)
HD2	NaN dBc (107 MHz)
HD3	-22.48 dBc (161 MHz)

DDS & ADC settings.

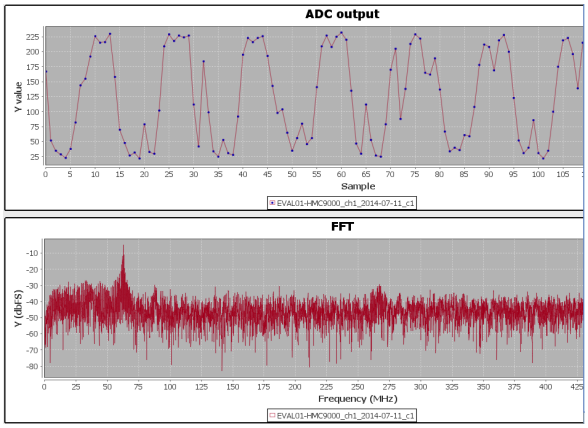

$t_d = 0.0082\mu s$, $\Delta f = 1$MHz

DDS Settings	
Sweep	**50MHz - 400MHz**
t_d	**0.0082μs**
Δf	**1MHz**
ADC Output (f_s = 1GHz)	
Signal	-4.93 dBFS
SNR	5.852 dBFS
SNDR	5.147 dBFS
ENOB	0.563 bit
SFDR	220 (62.0 MHz)
HD2	NaN dBc (125 MHz)
HD3	NaN dBc (188 MHz)

DDS & ADC settings.

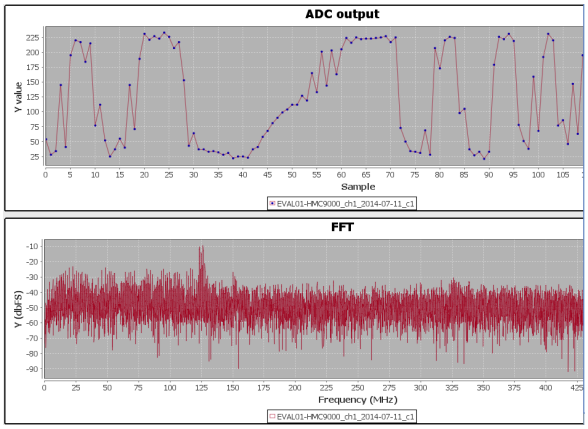

$t_d = 0.0082\mu s$, $\Delta f = 2$MHz

DDS Settings	
Sweep	**50MHz - 400MHz**
t_d	**0.0082μs**
Δf	**2MHz**
ADC Output (f_s = 1GHz)	
Signal	-9.45 dBFS
SNR	5.166 dBFS
SNDR	3.541 dBFS
ENOB	0.296 bit
SFDR	0.6359 (123 MHz)
HD2	NaN dBc (253 MHz)
HD3	NaN dBc (379 MHz)

DDS & ADC settings.

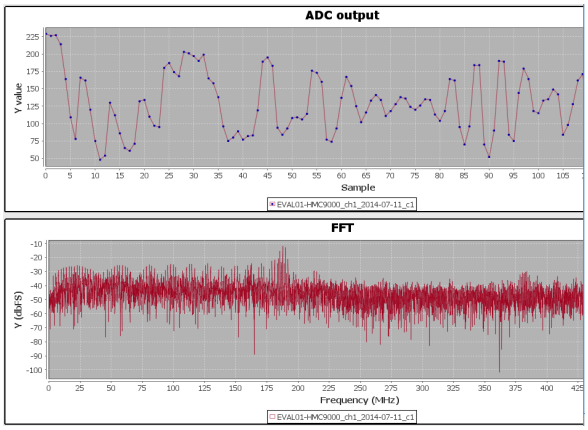

$t_d = 0.0082\mu s$, $\Delta f = 3$MHz

DDS Settings	
Sweep	**50MHz - 400MHz**
t_d	**0.0082μs**
Δf	**3MHz**
ADC Output (f_s = 1GHz)	
Signal	-12.0 dBFS
SNR	3.703 dBFS
SNDR	3.293 dBFS
ENOB	0.255 bit
SFDR	1.352 (190 MHz)
HD2	NaN dBc (375 MHz)
HD3	NaN dBc (437 MHz)

DDS & ADC settings.

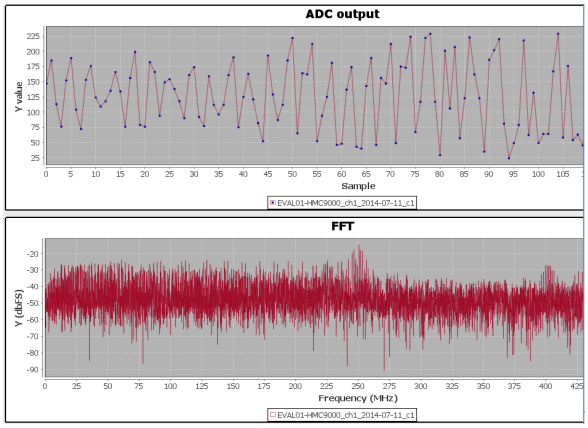

$t_d = 0.0082\mu s$, $\Delta f = 4$MHz

DDS Settings	
Sweep	**50MHz - 400MHz**
t_d	**0.0082μs**
Δf	**4MHz**
ADC Output (f_s = 1GHz)	
Signal	-14.6 dBFS
SNR	3.227 dBFS
SNDR	3.165 dBFS
ENOB	0.233 bit
SFDR	4.324 (246 MHz)
HD2	NaN dBc (499 MHz)
HD3	NaN dBc (248 MHz)

DDS & ADC settings.

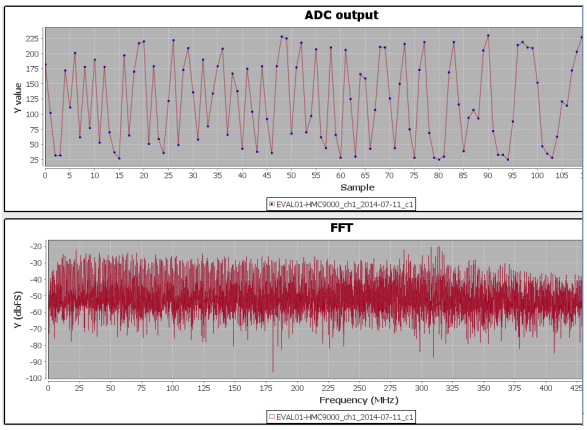

$t_d = 0.0082\mu s$, $\Delta f = 5$MHz

DDS Settings	
Sweep	**50MHz - 400MHz**
t_d	**0.0082μs**
Δf	**5MHz**
ADC Output (f_s = 1GHz)	
Signal	-19.9 dBFS
SNR	3.087 dBFS
SNDR	3.055 dBFS
ENOB	0.215 bit
SFDR	0.5591 (313 MHz)
HD2	NaN dBc (371 MHz)
HD3	NaN dBc (56.1 MHz)

DDS & ADC settings.

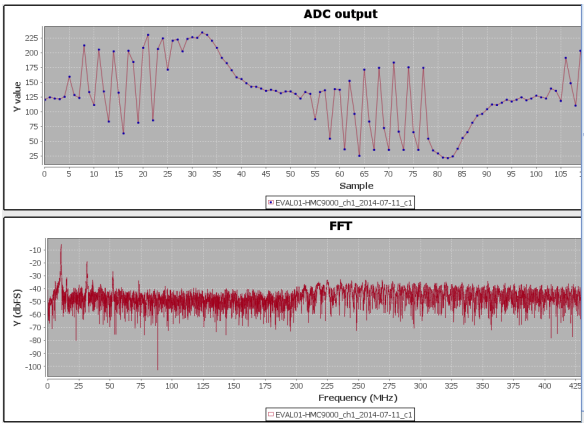

$t_d = 0.0490\mu s$, $\Delta f = 1$MHz

DDS Settings	
Sweep	**50MHz - 250MHz**
t_d	**0.0490μs**
Δf	**1MHz**
ADC Output (f_s = 1GHz)	
Signal	-5.88 dBFS
SNR	8.447 dBFS
SNDR	7.928 dBFS
ENOB	1.02 bit
SFDR	2.30 (31.3 MHz)
HD2	NaN dBc (21.0 MHz)
HD3	3.10 dBc (31.5 MHz)

DDS & ADC settings.

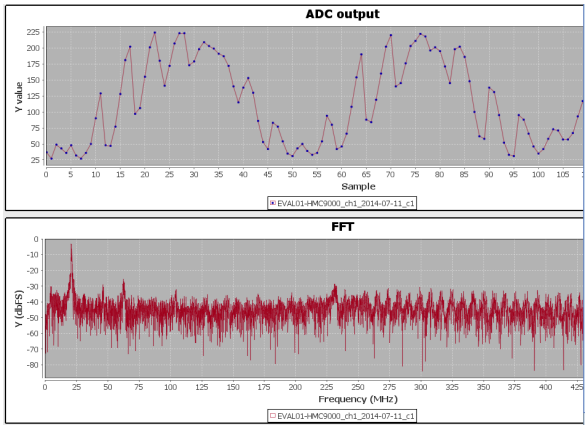

$t_d = 0.0490\mu s$, $\Delta f = 2$MHz

DDS Settings	
Sweep	**50MHz - 250MHz**
t_d	**0.0490μs**
Δf	**2MHz**
ADC Output (f_s = 1GHz)	
Signal	-3.41 dBFS
SNR	8.545 dBFS
SNDR	8.050 dBFS
ENOB	1.04 bit
SFDR	14.55 (- MHz)
HD2	NaN dBc (- MHz)
HD3	-24.72 dBc (- MHz)

DDS & ADC settings.

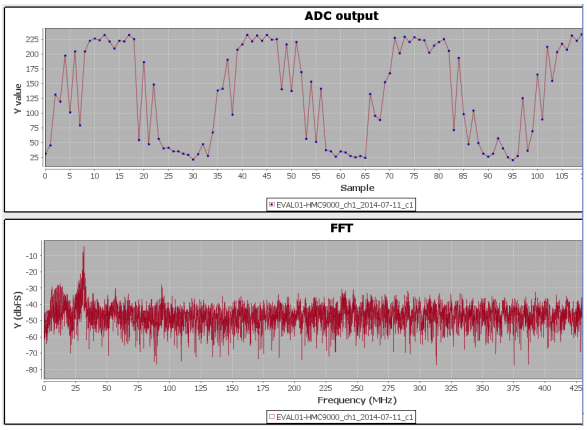

$t_d = 0.0490\mu s$, $\Delta f = 3$MHz

DDS Settings	
Sweep	**50MHz - 250MHz**
t_d	**0.0490μs**
Δf	**3MHz**
ADC Output (f_s = 1GHz)	
Signal	-4.47 dBFS
SNR	6.921 dBFS
SNDR	5.097 dBFS
ENOB	0.554 bit
SFDR	5.199 (30.9 MHz)
HD2	NaN dBc (63.1 MHz)
HD3	-34.15 dBc (94.7 MHz)

DDS & ADC settings.

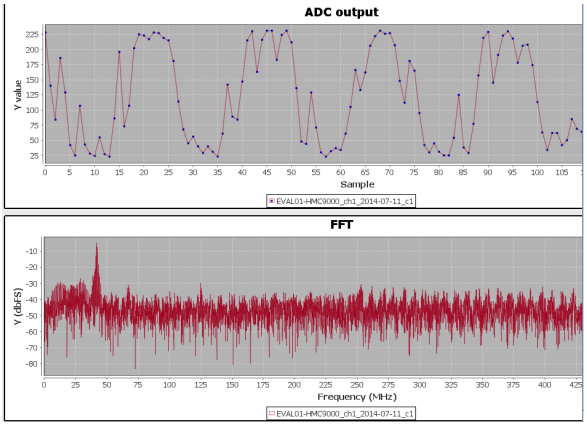

$t_d = 0.0490\mu s$, $\Delta f = 4$MHz

DDS Settings	
Sweep	**50MHz - 250MHz**
t_d	**0.0490μs**
Δf	**4MHz**
ADC Output (f_s = 1GHz)	
Signal	-4.97 dBFS
SNR	6.986 dBFS
SNDR	4.726 dBFS
ENOB	0.493 bit
SFDR	3.788 (42.3 MHz)
HD2	NaN dBc (82.9 MHz)
HD3	NaN dBc (124 MHz)

DDS & ADC settings.

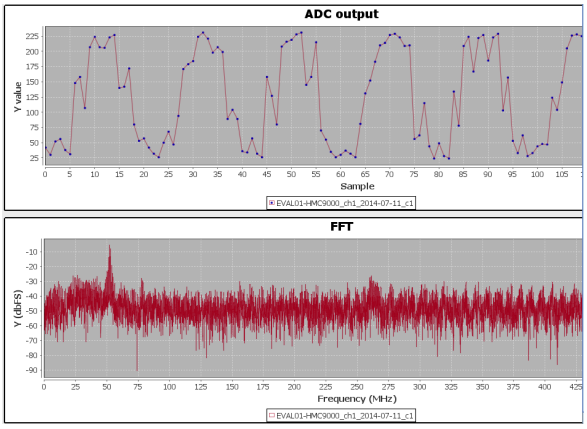

$t_d = 0.0490\mu s$, $\Delta f = 5$MHz

DDS Settings	
Sweep	**50MHz - 250MHz**
t_d	**0.0490μs**
Δf	**5MHz**
ADC Output (f_s = 1GHz)	
Signal	-5.36 dBFS
SNR	6.468 dBFS
SNDR	4.543 dBFS
ENOB	0.462 bit
SFDR	3.591 (52.9 MHz)
HD2	-34.87 dBc (104 MHz)
HD3	NaN dBc (155 MHz)

DDS & ADC settings.

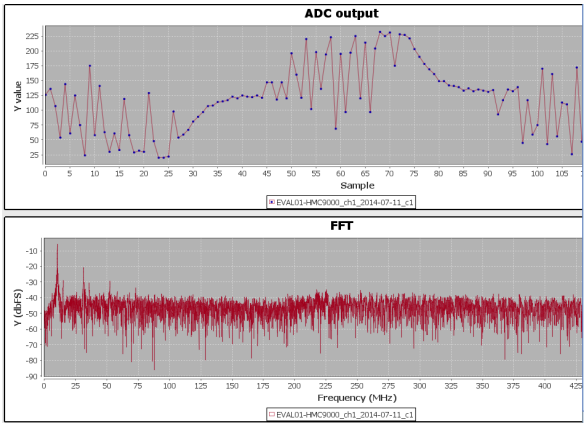

DDS Settings	
Sweep	**50MHz - 300MHz**
t_d	**0.0490μs**
Δf	**1MHz**
ADC Output (f_s = 1GHz)	
Signal	-5.83 dBFS
SNR	9.523 dBFS
SNDR	9.109 dBFS
ENOB	1.22 bit
SFDR	4.08 (31.3 MHz)
HD2	5/6.06 dBc (21.0 MHz)
HD3	5/6.14 dBc (31.5 MHz)

$t_d = 0.0490\mu s$, $\Delta f = 1$MHz

DDS & ADC settings.

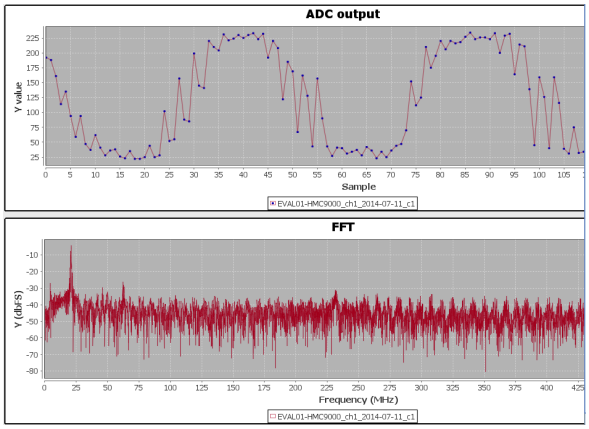

DDS Settings	
Sweep	**50MHz - 300MHz**
t_d	**0.0490μs**
Δf	**2MHz**
ADC Output (f_s = 1GHz)	
Signal	-4.29 dBFS
SNR	9.049 dBFS
SNDR	8.639 dBFS
ENOB	1.14 bit
SFDR	6/5.18 (20.1 MHz)
HD2	5.71 dBc (42.0 MHz)
HD3	4.59 dBc (63.0 MHz)

$t_d = 0.0490\mu s$, $\Delta f = 2$MHz

DDS & ADC settings.

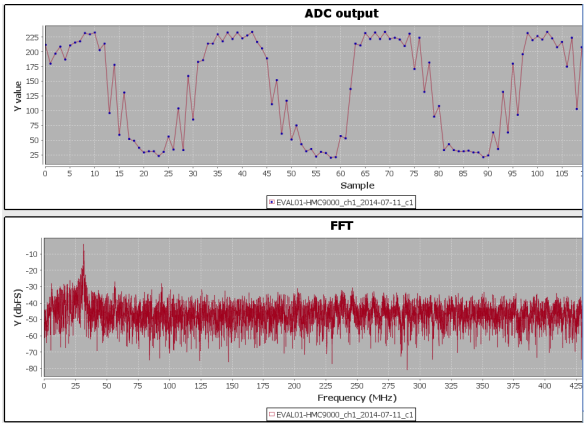

DDS Settings	
Sweep	**50MHz - 300MHz**
t_d	**0.0490μs**
Δf	**3MHz**
ADC Output (f_s = 1GHz)	
Signal	-4.03 dBFS
SNR	7.623 dBFS
SNDR	7.388 dBFS
ENOB	0.935 bit
SFDR	6.20 (30.0 MHz)
HD2	NaN dBc (62.5 MHz)
HD3	5.69 dBc (93.8 MHz)

$t_d = 0.0490\mu s$, $\Delta f = 3$MHz

DDS & ADC settings.

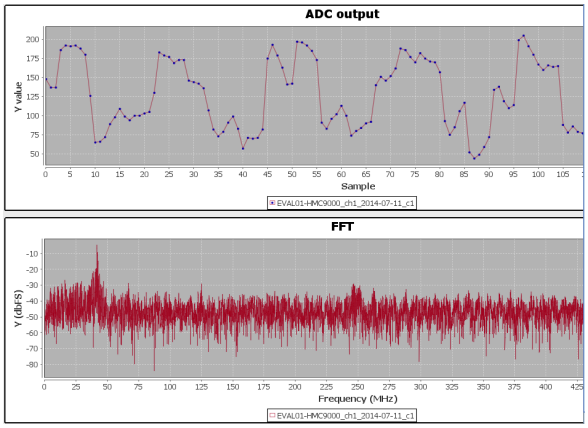

DDS Settings	
Sweep	**50MHz - 300MHz**
t_d	**0.0490μs**
Δf	**4MHz**
ADC Output (f_s = 1GHz)	
Signal	-4.60 dBFS
SNR	6.793 dBFS
SNDR	6.319 dBFS
ENOB	0.757 bit
SFDR	11.49 (42.4 MHz)
HD2	NaN dBc (83.4 MHz)
HD3	-25.82 dBc (125 MHz)

$t_d = 0.0490\mu s$, $\Delta f = 4$MHz

DDS & ADC settings.

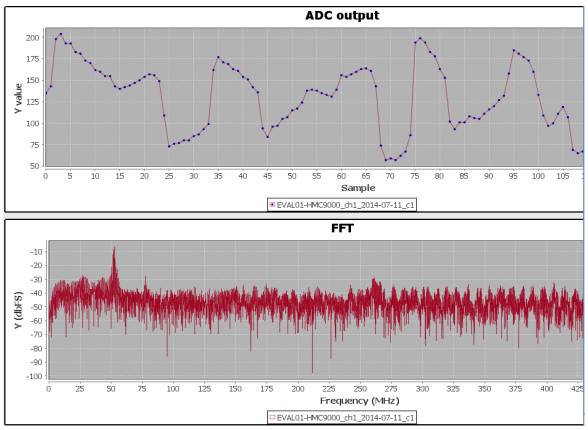

DDS Settings	
Sweep	**50MHz - 300MHz**
t_d	**0.0490μs**
Δf	**5MHz**
ADC Output (f_s = 1GHz)	
Signal	-6.52 dBFS
SNR	6.077 dBFS
SNDR	4.676 dBFS
ENOB	0.484 bit
SFDR	3.574 (51.7 MHz)
HD2	NaN dBc (105 MHz)
HD3	NaN dBc (158 MHz)

$t_d = 0.0490\mu s$, $\Delta f = 5$MHz

DDS & ADC settings.

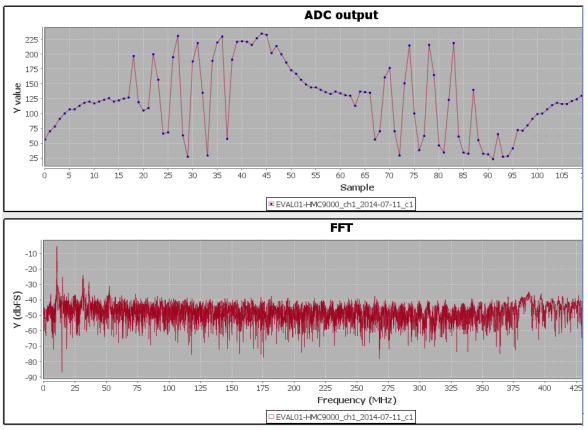

$t_d = 0.0490\mu s$, $\Delta f = 1$MHz

DDS Settings	
Sweep	**50MHz - 400MHz**
t_d	**0.0490μs**
Δf	**1MHz**
ADC Output (f_s = 1GHz)	
Signal	-5.29 dBFS
SNR	9.799 dBFS
SNDR	9.471 dBFS
ENOB	1.28 bit
SFDR	7.43 (31.1 MHz)
HD2	NaN dBc (20.9 MHz)
HD3	6.83 dBc (31.3 MHz)

DDS & ADC settings.

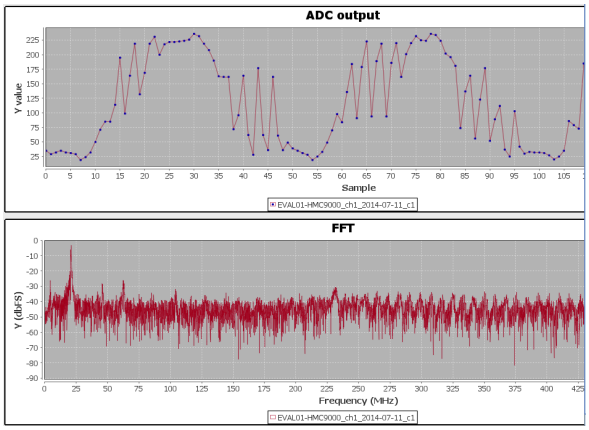

$t_d = 0.0490\mu s$, $\Delta f = 2$MHz

DDS Settings	
Sweep	**50MHz - 400MHz**
t_d	**0.0490μs**
Δf	**2MHz**
ADC Output (f_s = 1GHz)	
Signal	-3.37 dBFS
SNR	8.629 dBFS
SNDR	8.281 dBFS
ENOB	1.08 bit
SFDR	6.90 (21.7 MHz)
HD2	3.14 dBc (42.0 MHz)
HD3	3.34 dBc (63.0 MHz)

DDS & ADC settings.

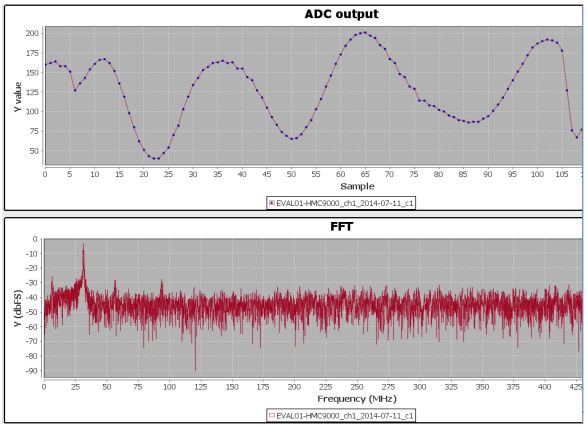

$t_d = 0.0490\mu s$, $\Delta f = 3$MHz

DDS Settings	
Sweep	**50MHz - 400MHz**
t_d	**0.0490μs**
Δf	**3MHz**
ADC Output (f_s = 1GHz)	
Signal	-3.32 dBFS
SNR	7.922 dBFS
SNDR	7.520 dBFS
ENOB	0.957 bit
SFDR	14.93 (30.8 MHz)
HD2	NaN dBc (62.7 MHz)
HD3	-28.00 dBc (94.1 MHz)

DDS & ADC settings.

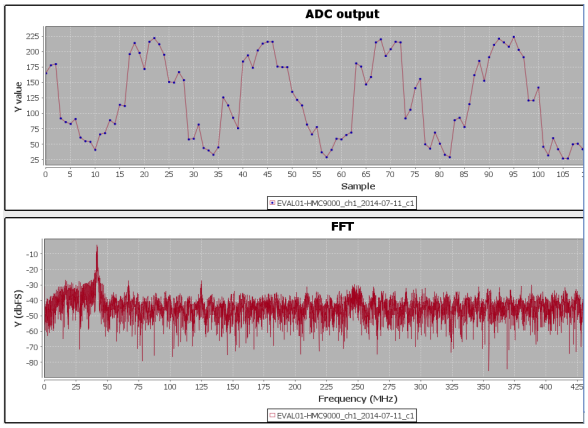

$t_d = 0.0490\mu s$, $\Delta f = 4$MHz

DDS Settings	
Sweep	**50MHz - 400MHz**
t_d	**0.0490μs**
Δf	**4MHz**
ADC Output (f_s = 1GHz)	
Signal	-4.23 dBFS
SNR	7.115 dBFS
SNDR	5.931 dBFS
ENOB	0.693 bit
SFDR	7.911 (41.0 MHz)
HD2	NaN dBc (83.5 MHz)
HD3	-26.84 dBc (125 MHz)

DDS & ADC settings.

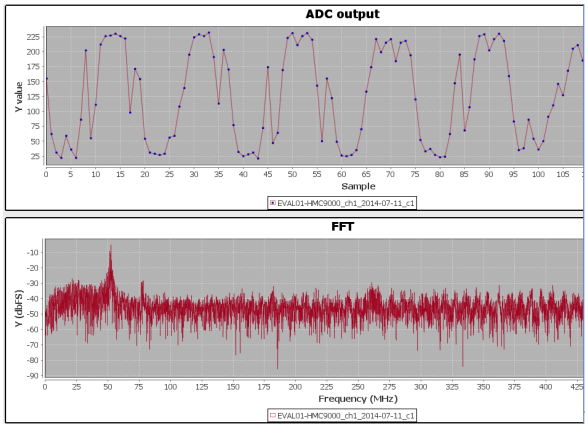

$t_d = 0.0490\mu s$, $\Delta f = 5$MHz

DDS Settings	
Sweep	**50MHz - 400MHz**
t_d	**0.0490μs**
Δf	**5MHz**
ADC Output (f_s = 1GHz)	
Signal	-5.16 dBFS
SNR	6.180 dBFS
SNDR	4.936 dBFS
ENOB	0.528 bit
SFDR	5.616 (51.6 MHz)
HD2	NaN dBc (105 MHz)
HD3	NaN dBc (157 MHz)

DDS & ADC settings.